An Ultracold Dipolar Gas of Ground-state ^{23}Na^{87}Rb Molecules

基態^{23}Na^{87}Rb分子的極性超冷氣體

GUO, Mingyang

郭鳴陽

A Thesis Submitted in Partial Fulfilment

of the Requirements for the Degree of

Doctor of Philosophy

in

Physics

The Chinese University of Hong Kong

December 2017

Thesis Assessment Committee

Professor XU, Lei (Chair)

Professor WANG, Dajun (Thesis Supervisor)

Professor WANG, Jianfang (Committee Member)

Professor DU, Shengwang (External Examiner)

Abstract

Abstract of thesis entitled:

An Ultracold Dipolar Gas of Ground-state $^{23}Na^{87}Rb$ Molecules

Submitted by GUO, Mingyang

for the degree of Doctor of Philosophy

at The Chinese University of Hong Kong in December 2017

This thesis describes the creation and collisional investigations of a high density sample of ultracold ground-state dipolar $^{23}Na^{87}Rb$ molecules. These molecules are produced by transferring weakly-bound Feshbach molecules to the ground state through a two-photon Raman process. To this end, an ultrastable and narrow linewidth Raman laser system is constructed by locking two diode lasers to a dual-wavelength coated high-finesse optical cavity. After identifying the two-photon pathway, a Stimulated Raman adiabatic passage with efficiency up to 93% is achieved, which allows us to produce a sample of absolute ground-state $^{23}Na^{87}Rb$ molecules with density as high as 6×10^{11} cm^{-3}. An effective electric dipole moment over 1 Debye, the largest ever achieved in ultracold molecules, is also demonstrated by applying a static electric field.

Although the absolute ground-state $^{23}Na^{87}Rb$ molecules are chemically stable, an unexpected fast two-body loss is observed. Thus, collisions of the molecules prepared to different internal states, which is achieved by combining the high-resolution two-photon Raman process with extra microwave pulses, are investigated. Loss rates of the ground-state molecules with different dipolar interaction

strength are also measured. These results pave the way toward the investigations of ultracold gases with strong dipolar interactions

摘要

本論文介紹了高密度基態超冷極性鈉銫分子的製備以及對其碰撞性質的研究。為了把分子從弱束縛費什巴赫態轉移到基態，我們搭建了一套超穩且具備超窄線寬的激光系統。通過合適的雙光子拉曼過程，我們實現了93%的轉移效率，成功製備了密度高達6×10^{11} cm^{-3}的基態超冷鈉銫分子。通過外加靜電場，我們成功誘導基態分子達到1 Debye的等效電偶極矩，這是目前在超冷分子里實現的最大等效電偶極矩。

儘管基態鈉銫分子是化學穩定的，我們依然在實驗上觀測到了分子的嚴重損耗。通過對分子內態的超精密操控，我們研究了分子在有化學反應和沒有化學反應發生情況下的損耗行為，並且觀測到了非常相似的動力學過程。此外，我們還研究了在不同偶極相互作用強度下的分子損耗，在超冷溫度下同時觀測到了s分波和d分波的貢獻。雖然這些結果還不足以確定基態分子的損耗機制，我們的成果對極性超冷氣體的研究具有重要意義。

Acknowledgement

I feel grateful to many people during my PhD period in CUHK. First, I would like to give my deepest thanks to my advisor Professor Dajun Wang. I really appreciate his insightful and instructive suggestions not only to my work but also to my life. His foresight and intuition on the experiments keep our research moving forward. Under his instructions, I have learned a lot on both the experimental skills and the understandings of physics problems.

I would also like to thank everyone I have worked with in the lab. They are both my colleagues and my best friends, whom I have enjoyed countless joyful moments with. Dr. Fudong Wang is always enthusiastic and hard working, from whom I have gained a lot of technical skills. Without him the new system cannot be up and running in such a short time. Dr. Xiaoke Li is patient in answering my questions and willing to help whenever I need. Dr. Bing Zhu has a wide scope of knowledge and always shares with us the latest progresses of experiments around the world. Together with him, we realized the first creation of the ground-state ^{23}Na^{87}Rb molecules. Xin Ye, who joined the group one year after me, has insightful understandings on physics problems and can always bring me new inspirations. I really enjoy working with him for the last two years on the molecular collisions. I would also like to thank Dr. Xiaodong He, Dr. Bo Lu and Dr. Shi Yu, who are postdocs in our group. They have taught me a lot of knowledge and shared their experimental experience with us. I appreciate the younger graduate students in our group, Lintao Li, Junyu He and Zhichao Guo, for their help to the experiments. They are all hard working and fully capable to

keep the setup running smoothly from day to day. I will always feel fortunate to be a part of this group.

Besides those in our group, many other people also helped me a great deal in the last several years. I would like to thank the members of the Theomol team of Laboratoire Aimé Cotton in Orsay, Frence, including Prof. Olivier Dulieu, Dr. Goulven Quéméner, Dr. Nadia Bouloufa and Dr. Romain Vexiau for their theoretical supports. Through discussing with them, especially Dr. Goulven Quéméner, I have gained a good understanding on basic molecular structures as well as the interaction between the molecules. They are patient to my questions and spare no effort in explaining all the details to me. I also thank the help of Dr. Yige Lin in Chinese National Institute of Metrology, where I learned to set up narrow linewidth lasers. I would like to thank the staffs and the technicians in our department for their assistances.

Last but not the least, I cannot express my gratitude in words to my parents and my brother for their support.

Dedicate to my family

for their selfless love and support.

Contents

Abstract **i**

Acknowledgement **iv**

1 Introduction **1**

1.1 Dipole-dipole interaction in ultracold gases 2

1.2 Dipolar $^{23}Na^{87}Rb$ molecule 4

1.3 Stimulated Raman adiabatic passage 8

1.4 Thesis outline 12

2 Experimental Apparatus **14**

2.1 Overview 15

2.2 Weakly-bound Feshbach molecules 17

2.3 Removal of residual atoms 19

2.4 Raman laser system 21

2.4.1 The ULE cavity 23

2.4.2 PDH locking 25

2.5 High voltage electrodes 30

3 Spectroscopy of $^{23}Na^{87}Rb$ Feshbach Molecules **33**

3.1 Requirements of the intermediate state 34

3.2 Potentials of $^{23}Na^{87}Rb$ molecules 35

3.3 The $A\,^1\Sigma^+ - b\,^3\Pi$ mixed states 37

3.3.1 The $A\,^1\Sigma^+ - b\,^3\Pi$ mixed vibrational states 40

3.3.2 Hyperfine structures of the $A\,^1\Sigma^+ - b\,^3\Pi$ mixed states . . . 41
3.3.3 Calibration of the transition strengths 50
3.4 Ground state spectroscopy 52
3.5 The $B\,^1\Pi - c\,^3\Sigma^+$ coupled states 56

4 Creation of the Ground-state ^{23}Na^{87}Rb Molecules 61
4.1 STIRAP to the absolute ground state 62
4.2 Properties of the ground-state molecules 65
4.2.1 The permanent electric dipole moment 65
4.2.2 The polarizability 70
4.3 Full internal state control 73

5 State Controlled Molecular Collisions 84
5.1 Collisions with controlled chemical reactivities 86
5.1.1 Universal model for chemical reaction 87
5.1.2 The sticky model 89
5.1.3 Temperature dependent loss coefficient 90
5.1.4 Full model for the chemically stable collisions 96
5.2 Effect of STIRAP efficiency 100
5.3 Molecular loss in different internal states 101

6 Ultracold Dipolar Collisions 104
6.1 Stability and inhomogeneity of the E-field 104
6.1.1 The E-field stability 105
6.1.2 The E-field inhomogeneity 105
6.2 Molecular collisions with dipole-dipole interactions 108
6.3 The dipolar collisions 114
6.4 Temperature dependence of the dipolar collisions 117

7 Conclusion and Outlook 122
7.1 Conclusion 122

7.2 Outlook 123
7.2.1 Figuring out the loss mechanism 123
7.2.2 Obtaining colder molecular samples 124
7.2.3 Molecular samples in an optical lattice 127

Bibliography **129**

List of Figures

1.1 STIRAP scheme for a three-level system. 10

2.1 The two-chamber vacuum system. 16
2.2 Production of FMs from atomic mixture. 18
2.3 Lifetime of the FMs. 19
2.4 The Raman laser system. 22
2.5 The ULE optical cavity. 24
2.6 Cavity FSR measurement. 25
2.7 Cavity ring down signal. 26
2.8 Scheme for PDH locking. 27
2.9 The error signal for PDH locking and the transmission signal. . . 28
2.10 Noise spectral density of the two diode lasers. 29
2.11 The Electrodes setup. 31
2.12 E-field simulation. 32

3.1 The potential of energy curves of $^{23}Na^{87}Rb$ molecule. 36
3.2 Calculated TDMs of $A\,^1\Sigma^+ - b\,^3\Pi$ mixed vibrational states to the Feshbach state and the singlet ground state. 38
3.3 The observed $A\,^1\Sigma^+ - b\,^3\Pi$ mixed vibrational states through one-photon spectroscopy. 40
3.4 HFS of the $|v' = 60\rangle$ state. 43
3.5 HFS of the $|v' = 59, J' = 1\rangle$ state. 45
3.6 Anomalously HFS of the $|v' = 55, J' = 1\rangle$ state. 46

3.7 Computed values of the spacings between 0^+ and adjacent 0^- levels. 47
3.8 Comparison between the experimentally extracted and the theoretically calculated TDMs of the $|v' = 55, J' = 1\rangle$ hyperfine levels. 48
3.9 Calibration of the pump transition strengths. 51
3.10 Two-photon spectroscopy to locate the singlet ground state through the $|v' = 55, J' = 1\rangle$ state. 53
3.11 Two-photon spectroscopy of the rovibrational ground state with resolved HFS. 55
3.12 Two-photon dark-state spectrum for calibrating the dump transition strength. 56
3.13 SOC potentials near the $B\,^1\Pi - c\,^3\Sigma^+$ mixing region. 57
3.14 HFS of the 12449 cm^{-1} vibrational state of the $B\,^1\Pi$ potential. . . 58
3.15 One- and two- photon lineshape of the 12449 cm^{-1} hyperfine level. 59

4.1 Time evolution of STIRAP transfer process. 63
4.2 STIRAP spectrum of the rovibrational ground state with different Raman pulse durations. 64
4.3 One- and two- photon spectrum under different static E-fields. . . 66
4.4 DC start shift of the intermediate state and the absolute ground state. 68
4.5 The effective dipole moments of the first two rotational states. . . 69
4.6 Real part of the theoretical polarizability of a singlet vibrational ground-state molecule. 71
4.7 Center-of-mass motion of the Feshbach molecules and the absolute ground-state molecules in the ODT. 72
4.8 STIRAP spectrum of the first excited vibrational state $|v = 1, J = 0\rangle$. 74
4.9 STIRAP spectrum of the second excited rotational state. 76
4.10 Microwave spectroscopy to probe the $J = 1$ hyperfine levels. . . . 77

4.11 STIRAP spectrum of the rovibrational ground state with ODT turned off. 78
4.12 Coherent microwave control of $J = 0$ hyperfine levels through a $J = 1$ level. 82

5.1 Typical number and temperature evolution of $v = 0$ and $v = 1$ molecules. 92
5.2 Fitting result by separating the whole loss curve into four sections 93
5.3 Temperature dependent β for $v = 0$ and $v = 1$ molecules. 95
5.4 Comparison between the fits with two-body model and the full model. 98
5.5 Extracted β for different STIRAP efficiencies. 100
5.6 Molecular loss coefficients of the different hyperfine and rotational levels of the vibrational ground state. 102

6.1 Stability of the E-field. 106
6.2 Characterizing the E-field inhomogeneity. 107
6.3 Adiabatic potentials for s-wave and d-wave. 110
6.4 Characteristic energy of the barrier-less s-wave potentials. 111
6.5 Barrier heights of the d-wave scattering channels. 112
6.6 Barrier heights of the g-wave scattering channels. 113
6.7 Typical molecule evolutions at an E-field. 114
6.8 d dependence of the loss coefficient. 116
6.9 The separated contributions of s-wave and d-wave scatterings to the molecular loss. 118
6.10 Temperature dependence of the dipolar collision loss rates. 120

7.1 The ratio between the elastic and the inelastic collision rates of the $J = 1$ molecules as a function of the E-field. 125

7.2 The rate coefficients for a 2D sample of the absolute ground-state $^{23}Na^{87}Rb$ molecules. 126

List of Tables

3.1 Calculated components fraction of each observed vibrational state. 39

4.1 Fitted hyperfine coupling constants of the singlet vibrational ground state. 79

4.2 Components of the relevant $J = 0$ hyperfine levels. 80

4.3 Components of the relevant $J = 1$ hyperfine levels. 81

5.1 Binding energies of relevant dimers and trimers. 86

5.2 The dispersive C_6 coefficients, the van der Waals temperatures, and the universal loss rates in the Wigner regime. 89

5.3 Parameters for the three fits in Fig. 5.4. 99

Chapter 1

Introduction

After more than two decades of development, ultracold quantum gas, which can now be routinely created using standard laser cooling [1, 2] and evaporative cooling [3] techniques, has become an indispensable branch of experimental physics. It has been successfully applied to search novel quantum matters, including the realization of Bose-Einstein condensation (BEC) [4, 5, 6] and degenerate Fermi gas [7]. The clean environment and full controllability over the internal and external degrees of freedom make it an ideal platform to implement precise measurements [8, 9] and quantum simulations for condensed matter physics [10, 11, 12]. Utilizing Feshbach resonances [13, 14] to precisely control the mutual interaction strengths, landmark results have been achieved including the observations of BCS–BEC crossover in degenerate Fermi gases [15, 16], the universal Efimov physics [17, 18, 19] and creation of ultracold molecules from atom pairs [20, 21, 22, 23]. Moreover, the emergence of optical lattices, controlling the external potentials, has enabled the observation of phase transition from a superfluid phase to a Mott insulating phase [24, 25]. With the recently realized quantum gas microscopy on both bosons [26, 27] and fermions [28, 29, 30], investigations on strongly correlated systems and antiferromagnetic order [31, 32, 33] to the single lattice site and single atom resolution have become feasible. Furthermore, investigations on systems with more than one atomic species to obtain

extra controllability are also fast developing.

1.1 Dipole-dipole interaction in ultracold gases

For most ultracold atomic systems, the interaction between the particles is typically dominated by an effective contact interaction [34], which can be expressed as

$$U_{\text{contact}}(\mathbf{r}) = \frac{4\pi\hbar^2 a}{m}\delta(\mathbf{r}), \tag{1.1}$$

for weakly interacting gases. Here, $\hbar$ is Planck constant over 2π, a represents the s-wave scattering length and m is the mass of the particles. Although the contact interaction can be widely tuned with the help of Feshbach resonances, its isotropic and short-range properties intrinsically limit its applications and the attainable models. However, within particles possessing magnetic dipole moments or permanent electric dipole moments or both, another kind of interaction called the dipole-dipole interaction (DDI) can emerge. For two dipoles that are polarized along a direction with an angle θ with respect to their relative position $\mathbf{r}$, the mutual DDI can be expressed in the form [35]

$$U_{dd}(\mathbf{r}) = \frac{C_{dd}}{4\pi}\frac{1-3\cos^2\theta}{r^3}. \tag{1.2}$$

Here, the coupling parameter C_{dd} equals to $\mu_0\mu^2$ for magnetic dipole moments μ (μ_0 the vacuum permeability) and d^2/ϵ_0 for electric dipole moments d (ϵ_0 the vacuum permittivity). In analogous to the s-wave scattering length a, a parameter called dipole length

$$a_{dd} = \frac{C_{dd}m}{4\pi\hbar^2}, \tag{1.3}$$

is introduced to characterize the strength of the dipolar interaction. To achieve strong DDI, the dipole length should be larger than the s-wave scattering length a and comparable to the inter-particle spacing.

Distinct from the contact interaction, the DDI is long range, proportional to $1/r^3$, and spatially anisotropic. The interaction is attractive for head-to-tail

($\theta = 0°$) configuration while repulsive for side-by-side ($\theta = 90°$) fashion. Furthermore, the scattering property with the presence of the DDI is also starkly different. In ultracold systems with dominant contact interaction, only s-wave scattering, characterized by the s-wave scattering length a, can take place. While, higher partial waves are suppressed due to their centrifugal barriers, which are too high for the ultracold samples. However, with the presence of the anisotropic DDI, which couples partial waves with the same parity, higher partial waves also significantly contribute to the scattering processes even in the ultracold regime.

Due to its distinct properties from conventional atomic systems, ultracold dipolar gas has been proposed to be a good platform for realizing new types of quantum simulators and novel quantum phases [36, 37, 38] including the long pursuing supersolid phase [39, 40, 41]. Stimulated by the applications, experimental investigations on ultracold dipolar gases are developing fast in recent years. The observations of the trap-geometry dependent stability [42], d-wave collapse of a dipolar BEC [43] and Fermi surface deformation [44] have manifested the angular dependence of the DDI. Effects of the anisotropic interaction on the collisions and rethermalization processes have also been investigated in samples of magnetic atoms [45, 46, 47, 48, 49] as well as polar molecules [50]. Furthermore, exotic quantum magnetism [51, 52, 53] with dipolar gases loaded into optical lattices has been studied with the KRb molecules [54, 55]. The extended Hubbard model with direct nearest-neighbor interactions via the DDI was also investigated [56]. More recently, a novel phase of self-bound droplets has also been obtained in magnetic atom samples [57, 58, 59, 60]. Moreover, chaotic scattering resonances within magnetic atoms were also observed [61, 62, 63].

To realize the DDI in quantum gases, the constituents must possess either magnetic dipole moments, or permanent electric dipole moments, or both. Up to now, three atomic species, including chromium (Cr), Erbium (Er) and Dysprosium (Dy) with relatively large magnetic dipole moments of 6 μ_B, 7 μ_B and 10 μ_B, have been successfully cooled down to quantum degeneracy [64, 65, 66, 67]. Ry-

dberg atom in a highly excited electronic state is also an option to realize strong DDI with the interaction energy scaling as n^4, where n is the principal quantum number of the excited state [68]. Another choice with large electric dipole moments is heteronuclear molecules in their absolute ground states.

1.2 Dipolar ^{23}Na^{87}Rb molecule

Among the three choices for realizing ultracold dipolar gases, the DDI through magnetic dipoles (magnetic atoms) is intrinsically much weaker than the that via electric dipoles as

$$\frac{\mu_0\mu^2}{d^2/\epsilon_0} \sim \alpha^2 \sim 10^{-4}, \tag{1.4}$$

where $\alpha \approx 1/137$ is the fine structure constant. Dy atoms, which possess the largest magnetic dipole moment of 10 μ_B, only reach $a_{dd} = 395\ a_0$, with a_0 the Bohr radius. While, polar molecule, say ^{23}Na^{87}Rb molecule with an effective electric dipole moment of 1 D, can achieve $a_{dd} = 31000\ a_0$, which is about two orders of magnitude larger than Dy atoms. Besides, the strength of the DDI within magnetic atoms is hard to be experimentally controlled. However, magnetic atoms are easier to be cooled down to quantum degeneracy relative to polar molecules. Actually, many pioneer studies on the DDI are achieved in magnetic atom systems. For Rydberg atoms in highly excited states, realizing strong DDI is easy due to their large electric dipole moments. However, Rydberg systems are limited by their short lifetimes, typically less than 1 ms [68]. On the other hand, polar molecules in their absolute ground state can possess large permanent electric dipole moments. Furthermore, the interaction strength can be well controlled by tuning external electric fields. However, efficient cooling methods for polar molecules are still under explored. Since the first creation of ultracold ^{40}K^{87}Rb molecules in 2008 [69], degenerate polar molecules have not yet been achieved. Each of the three choices has certain advantages and drawbacks, and fruitful achievements have been accomplished on these areas. In this thesis, I will

demonstrate the realization of the strong DDI with ultracold $^{23}Na^{87}Rb$ molecules in our group.

Besides their large permanent electric dipole moments, heteronuclear molecules also have much richer internal states compared to atomic species. On one hand, the extra internal degrees of freedom make it more difficult to manipulate and directly cool the molecules. On the other hand, they also provide additional knobs to control the molecular systems in order to achieve novel applications, such as realizing exotic spin models [52, 54, 70], new types of quantum qubits [71, 72, 73] and state controlled quantum chemistry [74, 75].

To obtain ultracold samples of molecules, a straightforward method is cooling the exist molecules directly. However, due to the lack of cycling transitions, direct laser cooling of molecules is quite inefficient. Although breakthroughs have been achieved on the techniques for molecular cooling and trapping, including the realization of molecular magneto-optical trap (MOT) [76, 77, 78], directly cooled molecules have not yet reached the ultracold regime. At present, the most successful way to create ultracold molecules in definitive quantum states is via magneto-association of pairs of ultracold atoms into molecules, followed by a two-photon Raman process to reach their ground states. The method is first implemented by JILA on producing fermionic $^{40}K^{87}Rb$ molecules close to degeneracy in 2008 [69]. Following the same scheme, more species were then created including fermionic $^{23}Na^{40}K$ molecules [79], bosonic $^{87}Rb^{133}Cs$ molecules [80, 81] and $^{23}Na^{87}Rb$ molecules in our group [82], and more recently $^{6}Li^{23}Na$ molecules in their triplet ground state [83].

Among the ten bialkali heteronuclear molecules that can be associated from two different alkali-metal atoms of Li, Na, K, Rb and Cs, not all of them are chemically stable even in their rovibrational ground states. The loss of ground-state KRb molecules due to the exchange chemical reaction $2KRb \rightarrow K_2 + Rb_2$ has already been reported in Ref. [84, 85]. Actually, only five (NaK, NaRb, NaCs, KCs and RbCs) out of the ten molecular species are stable when two ground-sate

molecules collide [86].

With more and more ultracold molecular species becoming available, the research area is fast developing. Through extra microwave pulses, controlling the molecular internal states, including the rotational and hyperfine degrees of freedom, was achieved [87, 88, 89, 90]. Besides, long coherent time between two hyperfine levels of NaK molecules was observed [73], which can be utilized for quantum computation. The molecular collisions of the reactive KRb molecules were also systematically studied, including collisions with different quantum statistics [84], with the presence of the DDI [50], as well as in reduced dimensions [85]. Loading the molecules into optical lattices [91], high filling factors up to 30% were achieved both with KRb [92] and RbCs [93] molecules. Furthermore, direct spin-exchange within two rotational states of lattice confined KRb molecules were also observed [54, 55].

However, even after about nine years developments since the first creation of ultracold KRb molecules, some basic collisional properties of these molecules are still not clear. Recently, unexpected severe molecular losses were observed within the chemically stable ground-state molecules, including bosonic $^{87}Rb^{133}Cs$ [80] and $^{23}Na^{87}Rb$ [82] as well as fermionic $^{23}Na^{40}K$ [79] molecules. To explain the fast molecular loss, a mechanism called the "sticky" collision [94] was proposed, but has not yet been experimentally verified. Although the molecular loss can be avoided by loading the molecules into optical lattices [91, 92, 93] with each lattice site populating only one molecule, the loss mechanism itself, which can shine new light on our understandings of ultracold collisions, is of great interest and importance. What happens when two molecules are close together and whether the loss possibility in the short range is unity or not can give us valuable information on short-range physics and the structures of more complex molecular states that consist of four atoms, which cannot even be theoretically calculated at present. Moreover, the dipolar collisions were only studied in the reactive KRb molecules with small effective dipole moments less than 0.2 D [50, 85]. How the

strong DDI affects the molecular collisions especially the loss within the stable molecules was not experimentally studied previously. Whether it is possible to suppress the molecular loss and realize efficient evaporative cooling within bulk molecular samples with the help of the DDI are still remained to be answered. These questions motivate us to investigate the collisional properties of $^{23}Na^{87}Rb$ molecules, including the molecular loss with controlled chemical reaction and with strong DDI, which will be demonstrated in details in the next chapters.

The ground-state $^{23}Na^{87}Rb$ molecules studied in our system are chemically stable and have the largest permanent electric dipole moments among the obtained ultracold molecular species [95]. Due to the large dipole moments, we can realize strong DDI even with moderate electric fields, which are experimentally feasible. Furthermore, the rich internal degrees of freedom (vibrational, rotational and hyperfine) enable us to investigate the chemical reactions and inelastic processes within the molecules in fully controlled manners. Specifically, $^{23}Na^{87}Rb$ molecule is chemically stable in its rovibrational ground state, while chemical reaction is energetically allowed in vibrational excited states [96, 97, 98]. By preparing $^{23}Na^{87}Rb$ molecule to vibrational ground state or excited state, we can selectively turn off or on the chemical reaction. Besides, molecules in excited hyperfine and rotational states allow extra inelastic channels to take place. Thus, ultracold collisions of the molecules in different scenarios can be investigated by controlling their internal states.

To produce ground-state $^{23}Na^{87}Rb$ molecule, we follow the three-step method utilized by JILA [69, 99]. Firstly, an ultracold mixture of ^{23}Na and ^{87}Rb atoms in definitive hyperfine states is prepared in an optical dipole trap (ODT) [100]. Then, magneto-association is implemented by ramping the magnetic field (B-field) across the Na-Rb interspecies Feshbach resonance near 347.7 G [101, 102]. Directly after the association, residual atoms are removed. Finally, after pure samples of weakly-bound Feshbach molecules (FMs) are created, a two-photon Raman process is applied to coherently and efficiently transfer the molecules to

their absolute ground state [82].

1.3 Stimulated Raman adiabatic passage

As the first two steps of producing ultracold atomic mixture and weakly-bound FMs have been depicted in details in the previous theses of our group [103, 104], I will just introduce them briefly in this thesis. For the last step to realize efficient population transfer from the Feshbach state to the ground state, a two-photon Raman process called stimulated Raman adiabatic passage (STIRAP) [105, 106] is implemented.

The STIRAP involves three molecular levels coupled by two laser lights, as illustrated in Fig. 1.1(a). Here, the initial FM state $|F\rangle$ and the final ground state $|G\rangle$ are coupled by two coherent lasers, pump light L_P and dump light L_D, through an intermediate level $|e\rangle$, which is an electronic excited state with a spontaneous decay rate of Γ. Δ (δ) represents the one-photon (two-photon) detuning. The three-level system can be described by the Hamiltonian

$$\hat{H} = \hat{H}_0 - \sum_i \vec{d}_i \cdot \vec{E}_i - i\hbar\gamma. \tag{1.5}$$

Here,

$$\hat{H}_0 = \hbar\omega_F |F\rangle \langle F| + \hbar\omega_e |e\rangle \langle e| + \hbar\omega_G |G\rangle \langle G|, \tag{1.6}$$

is the Hamiltonian of the three bare levels with energies of $\hbar w_i$ ($i = F, e, G$) . The second term in Eq. 1.5 represents the couplings induced by the two laser beams and the last term with $\gamma = \Gamma/2$ accounts the decay of the intermediate state.

To obtain a more intuitive picture on the adiabatic transfer, the Hamiltonian is transformed from the bare-state basis to the dark-state basis following the transformation

$$\begin{pmatrix} |+\rangle \\ |-\rangle \\ |e\rangle \end{pmatrix} = \begin{pmatrix} \frac{\Omega_P}{\Omega} & \frac{\Omega_D}{\Omega} & 0 \\ i\frac{\Omega_D}{\Omega} & -i\frac{\Omega_P}{\Omega} & 0 \\ 0 & 0 & 1 \end{pmatrix} \begin{pmatrix} |F\rangle \\ |G\rangle \\ |e\rangle \end{pmatrix}, \tag{1.7}$$

where $\Omega(t) = \sqrt{\Omega_P(t)^2 + \Omega_D(t)^2}$ with Ω_P (Ω_D) the Rabi frequency of the pump (dump) transition. $|-\rangle$ ($|+\rangle$) is the dark (bright) state. As the Rabi frequencies are typically time dependent, the dark state is not a steady state but evolving with time, i.e. it is a instantaneous state. Correspondingly, the wavefunction of system is also transformed to

$$\begin{aligned} |\psi\rangle &= c_F |F\rangle + c_e |e\rangle + c_G |G\rangle \\ &= c_- |-\rangle + c_+ |+\rangle + c_e |e\rangle . \end{aligned} \tag{1.8}$$

In the condition of two-photon resonance, $\delta = 0$, the evolution of the state amplitudes under the rotating wave approximation follows [105, 107]

$$\frac{d}{dt}\begin{pmatrix} c_+ \\ c_- \\ c_e \end{pmatrix} = \begin{pmatrix} 0 & i\Omega_- & i\Omega \exp^{-i\Delta t} \\ i\Omega_- & 0 & 0 \\ i\Omega \exp^{-i\Delta t} & 0 & -\gamma \end{pmatrix} \begin{pmatrix} c_+ \\ c_- \\ c_e \end{pmatrix} . \tag{1.9}$$

Here, $\Omega_- = \frac{\dot{\Omega_P}\Omega_D - \dot{\Omega_D}\Omega_P}{\Omega^2}$ represents the effective coupling between state $|-\rangle$ and state $|+\rangle$, while state $|+\rangle$ couples to state $|e\rangle$ with strength of Ω. In this basis, no direct coupling exists between states $|-\rangle$ and $|e\rangle$, as shown in Fig. 1.1(b). Thus, state $|-\rangle$ can survive from the spontaneous decay of the excited state $|e\rangle$. This is the reason why state $|-\rangle$ is called the dark state.

For laser pulses with the shape as shown in Fig. 1.1(c), the dark state $|-\rangle$ is just the Feshbach state $|F\rangle$ before t_1 as a result of $\Omega_P(t < t_1) = 0$. However, after t_2 with $\Omega_D(t > t_2) = 0$, state $|-\rangle$ exactly corresponds to state $|G\rangle$. Ideally, if the system stays always in the dark state $|-\rangle$, i.e. the system adiabatically evolves, one can accomplish nearly 100% transfer efficiency from the initial Feshbach state $|F\rangle$ to the ground state $|G\rangle$. To achieve the adiabatic evolution, Ω_- should be much smaller than the field-induced splitting [105, 108], i.e.

$$|\frac{\dot{\Omega_P}\Omega_D - \dot{\Omega_D}\Omega_P}{\Omega^2}| \ll |\omega^{\pm} - \omega^0|, \tag{1.10}$$

which is the so-called adiabatic condition. With $\Delta = 0$, the adiabatic condition is simplified to

$$|\frac{\dot{\Omega_P}\Omega_D - \dot{\Omega_D}\Omega_P}{\Omega^2}| \ll |\omega^{\pm} - \omega^0| = \Omega. \tag{1.11}$$

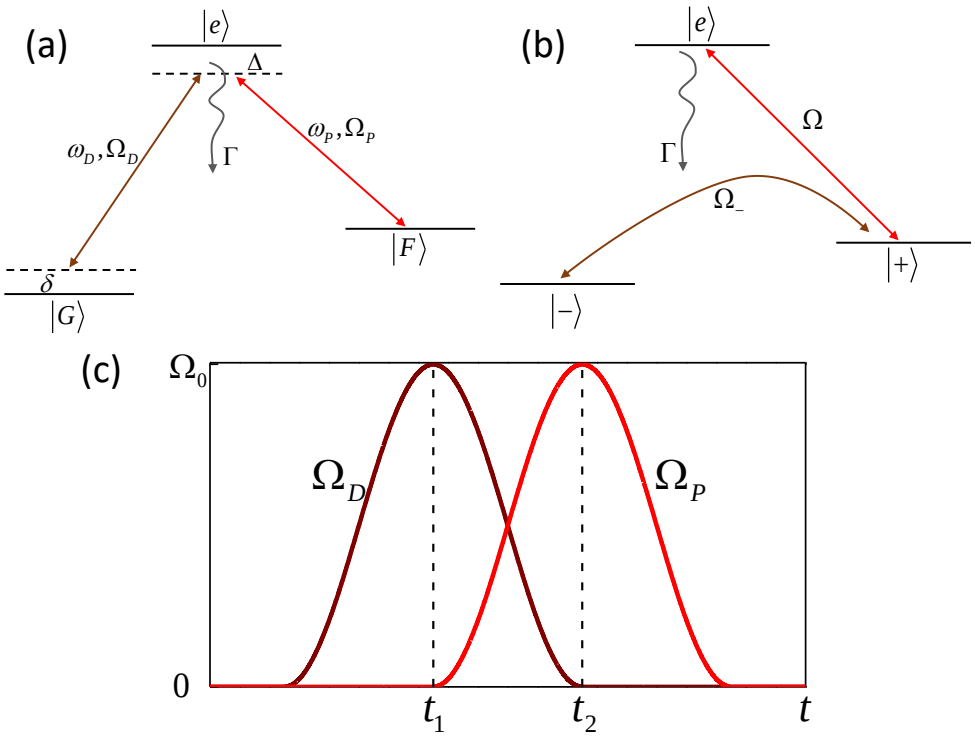

Figure 1.1: (a) Typical STIRAP scheme of a three-level system in the bare-state basis. The initial Feshbach level $|F\rangle$ is coupled to the intermediate state $|e\rangle$ by a pump light L_P with a frequency of ω_P and a Rabi frequency of Ω_P. A dump light L_D couples level $|e\rangle$ and the ground state $|G\rangle$ with a strength of Ω_D. Here, Δ and δ denote the one- and two-photon detuning. Level $|e\rangle$ is an excited state with a spontaneous decay rate of Γ, which corresponds to a typical lifetime of less than 1 μs. (b) The same STIRAP scheme but represented in the dark-state basis. The dark state $|-\rangle$, which is a superposition state of $|F\rangle$ and $|G\rangle$, decouples from the excited level $|e\rangle$. With well designed pulse shape such as the one shown in (c), the coupling Ω_- between $|-\rangle$ and $|+\rangle$ approaches zero, i.e. level $|-\rangle$ is isolated from the other part of the system. (c) Typical sine-shaped laser pulses for a STIRAP transfer.

For smooth varying laser pulses like Fig. 1.1(c), $\Omega_- \propto 1/\tau$, where $\tau = t_2 - t_1$ is the overlap of the two laser pulses. Thus, the adiabatic condition is reduced to

$$\Omega_0 \tau \gg 1. \tag{1.12}$$

To fulfill the adiabatic condition and achieve high transfer efficiency, it is favorable to have large peak Rabi frequency Ω_0 and long pulse overlap τ. However,

the pulse length is limited by the coherence time of the system, which is not considered in the above discussion. Decoherence can be introduced into the system via many effects, such as the fluctuation of the B-field, which affects the state energies, noise of the coupling lasers, and spontaneous decays of the involved levels besides state $|e\rangle$. To account the decoherence effects, which are mainly from the frequency noise of the two laser beams [109] in our system, the optical Bloch equation is implemented [110, 111]

$$\dot{\rho} = -\frac{i}{\hbar}[H, \rho] - \frac{1}{2}\{\Gamma, \rho\} + L_d(\rho). \tag{1.13}$$

Here, ρ is the density matrix, H is the Hamiltonian of the three-level system. The second term represents the spontaneous decay of the involved levels and the last term $L_d(\rho)$ is the Lindblad superoperator [112] to account the decoherence effects induced by the laser frequency noise. For the spontaneous decays, we assume decaying out from the three-level system once it happens. Thus, this spontaneous decay only induces loss of molecules but do not bring decoherence into the system. For the laser frequency noise, characterized by the laser linewidths, the Lindblad operator follows [111]

$$L_d(\rho) = \begin{pmatrix} 0 & -\gamma_P \rho_{Fe} & 0 \\ -\gamma_P \rho_{eF} & 0 & -\gamma_D \rho_{eG} \\ 0 & -\gamma_D \rho_{Ge} & 0 \end{pmatrix}. \tag{1.14}$$

Here, γ_P and γ_D are the linewidths (half width half maximum) of the pump and dump lights. Within our simulation, we assume no correlations between the two lasers, i.e. γ_P and γ_D are independent. Based on the parameters obtained from experimental calibrations, the simulation result of the STIRAP transfer process by numerically solving Eq. 1.14 agrees well with our measurements, as illustrated in Fig. 4.1.

1.4 Thesis outline

In this thesis, I summarize the studies on ultracold ^{23}Na^{87}Rb molecules during my PhD period, focusing on the first creation of pure ^{23}Na^{87}Rb molecular samples in their singlet ground state and the investigations on the collisional properties of the molecules with well controlled internal states and the dipole-dipole interaction. In addition to the introduction part in this chapter, the other six chapters are organized as below.

In chapter 2, the experimental apparatus and previous results realized in our group on preparing ultracold mixture of ^{23}Na and ^{87}Rb atoms and creating weakly-bound FMs are briefly described. Then, new atom removal scheme to obtain pure molecular samples is introduced. Finally, a stable Raman laser system for STIRAP transfer and the electrodes setup to manipulate the dipole-dipole interaction are presented in details.

Chapter 3 describes the high-resolution molecular spectroscopy carried out to identify suitable intermediate states for efficient STIRAP. The spectrum focuses on excited states with strong $A\,^1\Sigma^+ - b\,^3\Pi$ mixing, which is the one implemented in our experiments. Another scheme with $B\,^1\Pi - c\,^3\Sigma^+$ coupled intermediate states is also briefly introduced.

In chapter 4, the first successful creation and characterization of the absolute ground-state ^{23}Na^{87}Rb molecules are demonstrated. By combining the high-resolution STIRAP with extra microwave pulses, full control over the molecular internal states including their vibrational, rotational and hyperfine degrees of freedom are achieved.

Chapter 5 discusses the observation of unexpected fast loss of the ground-state molecules that are chemically stable. Enabled by the full control of the molecular internal states, we investigate the molecular loss with and without chemical reactions, where amazingly similar behaviors are observed. Moreover, collisions of molecules in different internal states with extra inelastic channels are

also studied.

In chapter 6, dipolar nature of the ground-state $^{23}Na^{87}Rb$ molecules is investigated by measuring the molecular loss with the presence of the dipolar interaction. With the largest effective dipole moments ever achieved, saturated s-wave scattering and non-ignorable d-wave scatterings are observed for the first time in the ultracold regime.

Finally, chapter 7 summarizes the main contents of this thesis and gives an outlook on future studies.

□ End of chapter.

Chapter 2

Experimental Apparatus

Although most of the spectroscopy work as well as the first signal of the ground-state $^{23}Na^{87}Rb$ molecules was done with our old system, I will focus on the new apparatus, where the characterization of the molecules and the investigations of their collisional properties were realized. The new machine, designed for the molecular experiments, is a two-chamber system with mechanical transportation. The two-chamber configuration enables us to achieve higher vacuum level and better optical accesses in the side of the science cell. Typically, the obtained molecule number in our new setup is more than 5 times larger than that with the old one. Moreover, the smaller size of the science glass cell make it possible to induce strong dipole-dipole interaction even with the electrodes placed outside of the cell. This new machine was built during my time in CUHK and I participated in the constructions of the system, including the ultra-high vacuum (UHV) part, the laser systems as well as the parts for generating external fields. As the whole setup has been described in details in previous theses of our group [103, 104], I will save effort in repeatedly introducing the system and the experimental sequences for creating the ultracold atomic mixture and FMs. Besides describing the main procedures, this chapter will focus on the new scheme to selectively remove residual atoms, the Raman laser system for the STIRAP transfer and the high-voltage electrodes to induce dipole-dipole interaction within the ground-

state molecules.

2.1 Overview

Figure 2.1 shows the setup of the two-chamber UHV system. The MOT cell (outer size: 100 mm×40 mm×40 mm, 3 mm wall thickness) and the science cell (outer size: 100 mm×20 mm×20 mm, 3 mm wall thickness) are connected through a differential tube to maintain the pressure difference between the two chambers. The typical vacuum pressure is about 3×10^{-11} Torr for the MOT cell and better than 10^{-11} Torr for the science cell. The transfer coil, part I in Fig. 2.1, working in the anti-Helmholtz configuration, is mounted on a mechanical translation stage (K) for transferring atoms from the MOT cell to the science cell.

Firstly, ^{23}Na and ^{87}Rb atoms are captured by a two-species 3D magneto-optical trap (MOT) with the translation stage on the side of the MOT cell. After standard procedures of molasses cooling and optical pumping, the atoms are trapped in the magnetic quadrupole trap generated by the transfer coil. Then, the atoms are transferred to the science cell following the translation stage with a transfer efficiency up to 90%. During the transfer process, both ^{23}Na and ^{87}Rb atoms are in $|F = 1, M_F = -1\rangle$ states, with F the total atomic angular momentum and M_F the corresponding projection.

After the transfer, the current of the transfer coil is gradually decreased to zero while the bias coil in the anti-Helmholtz configuration is synchronously ramped on, after which the atoms are loaded into the magnetic quadrupole trap generated by the bias coil. Then, the translation stage moves back to the MOT cell, giving room for the ODT. For further cooling of the atomic mixture, microwave force-evaporative cooling is implemented by driving transitions of ^{87}Rb atoms from $F = 1$ to $F = 2$, spilling hot ^{87}Rb atoms out. To suppress the undesired Majorana loss near the center of the quadrupole trap [113], one optical trap beam, displaced horizontally from the center of the quadrupole trap, is turned on to shift the trap

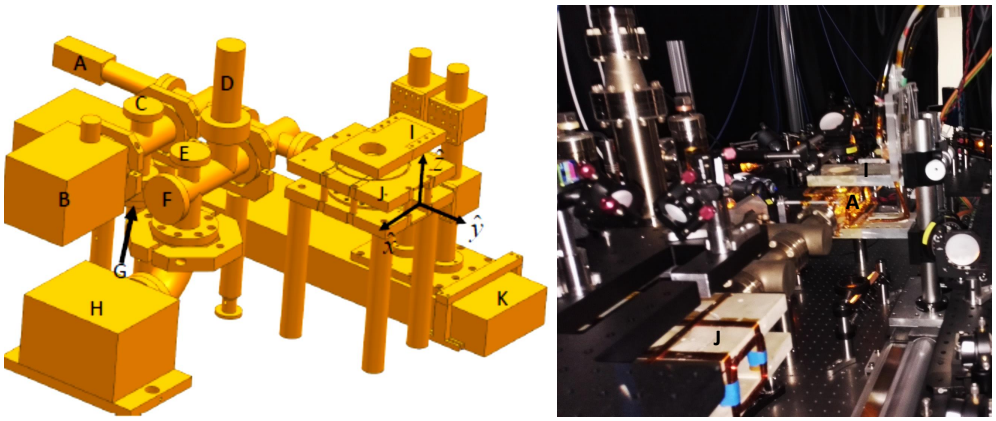

Figure 2.1: 3-D model and picture of the vacuum system. The 3-D model is taken from [103]. A: MOT cell; B: 25S ion pump; C and E: angle valves; D: Titanium Sublimation Pump; F: ion gauge; G: feedthrough; H: 45S ion pump; I: transfer coil; J: bias coil; K: translation stage; L (inside J): science cell.

minimum from the position with zero B-field. The combination of the quadrupole trap and the single beam form a hybrid trap [114, 115]. Thanks to the favorable background scattering length between ^{23}Na and ^{87}Rb atoms [101], ^{23}Na atoms are sympathetically cooled during the microwave evaporation.

After evaporative cooling in the hybrid trap, atoms are loaded into a crossed-beams ODT by turning on the other trap beam and shutting off the quadrupole trap. The ODT lights, generated from a single frequency fiber amplifier, work at a wavelength near 1064 nm, which can be tuned by changing the frequency of the seeding laser. The two beams propagate horizontally with an angle of 20.8° and both have beam waists of about 65 μm. To avoid interference, the polarizations of the two beams are orthogonal and a frequency difference of 220 MHz is imposed. As the trap depth for ^{23}Na atoms is smaller than that for ^{87}Rb atoms, hotter ^{23}Na atoms are rejected out of the trap while ^{87}Rb atoms are sympathetically cooled during the evaporation in the ODT. As a consequence, the number of ^{87}Rb atoms is barely changed in the ODT. By tuning the end ODT power of the evaporation, we can control the sample temperature of the atomic mixture. Furthermore, by changing the number of ^{87}Rb atoms loaded into the ODT, we

can tune the relative number between the two species.

2.2 Weakly-bound Feshbach molecules

To associate the FMs from the ultracold atomic mixture, an interspecies Feshbach resonance near 347.7 G is utilized [101, 102]. The Feshbach resonance is for ^{23}Na and ^{87}Rb atoms both in $|F = 1, M_F = 1\rangle$ states. As the atoms loaded from the hybrid trap are in $|1, -1\rangle$ states, a radio frequency (RF) adiabatic rapid passage (ARP) is applied to transfer the atoms to $|1, 1\rangle$ states under a B-field of about 3.5 G. As ^{23}Na and ^{87}Rb atoms have quite similar Zeeman splittings at low B-fields, a single ARP can transfer both species to $|1, 1\rangle$ states simultaneously with efficiencies up to 99%.

To achieve high association efficiency, it is favorable to have large phase space overlap between the samples of the two species. Although high phase space density can be achieved by preparing both species to be condensates, the fact that double BECs of ^{23}Na and ^{87}Rb atoms are immiscible with background interspecies scattering length [100] results in rather small density overlap between the two clouds. As a trade-off, we prepare ^{23}Na atoms to be a condensate while ^{87}Rb atoms are near degeneracy. The starts point for magneto-association is about 2×10^5 atoms for both species with a temperature of about 300 nK.

The experimental sequence for the magneto-association is shown in Fig. 2.2. Firstly, the B-field is jumped to 350 G, above the Feshbach resonance. After equilibrium is reached, the B-field is ramped across the Feshbach resonance, associating free atoms into weakly-bound FMs. The association process can be described by the Landau-Zener theory, which favors a slow B-field ramp for high conversion efficiency [116]. However, the severe three-body loss near Feshbach resonances [13, 117] prevents efficient production of the FMs with a slow B-field ramp. Thus, the association process is rather complicated and the ramp speed is empirically determined by optimizing the obtained FMs number. For our present

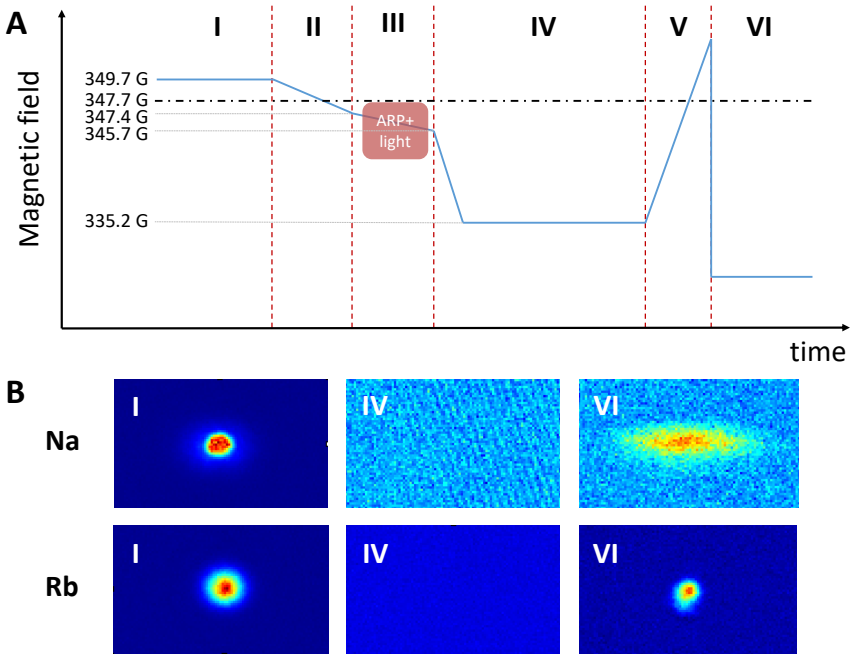

Figure 2.2: (A) Typical time sequence for magneto-association. I: atomic mixture at a B-field of 350 G; II: 1 ms B-field ramp across the Feshbach resonance for magneto-association; III: B-field ramp for removing residual atoms (Sec. 2.3); IV: pure FM samples; V: dissociation back to free atoms for detection; VI: detection of the free atoms at low B-field. (B) three pairs of absorption images of free atoms at three different stage of the sequence as labeled in the pictures. The first pair is the clouds of atomic mixture before association with long TOF. No signal is observed in the second pair as free atoms are removed and FMs cannot be detected directly. The last pair is the signal of the FMs after being dissociated back to free atoms for detection. The distinct shapes of ^{23}Na and ^{87}Rb clouds are due to different imaging directions.

experimental sequence, the typical atom-molecule conversion efficiency is only about 7%, i.e. 1.5×10^4 FMs. Due to the heating effects during the association process, the obtained molecular sample typically has temperature of about 600 nK.

As direct detection of the FMs is not available, we have to dissociate the molecules back into free atoms and then detect the atoms at a low B-field, as shown in Fig. 2.2(A) the stage **V** and **VI**. Due to the residual B-field after shut-

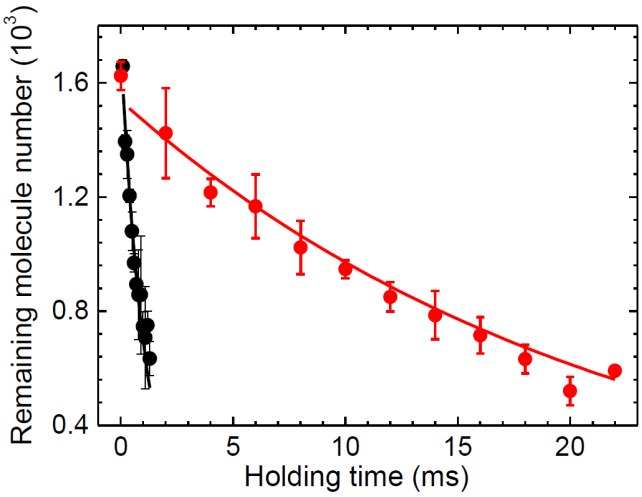

Figure 2.3: Lifetime of the FM with residual atoms removed (red) and with the presence of free atoms (black) at a B-field of 335 G. Solid curves are exponential fitting to the experimental data. Reproduced from Ref. [102]

ting off the high B-field, we must hold the dissociated atoms for several tens of millisecond in order to precisely detect the atom number, which corresponds to the molecule number assuming no loss during the procedure of dissociation and atom holding. However, this method does not work for measuring the temperature of the molecules as the process of dissociation heats the sample [118, 119]. Thus, we first turn off the ODT before dissociation, letting the FMs undergo free time-of-flight (TOF) expansion, and dissociate the molecules about 1 ms before the imaging pulse. Although the dissociated atoms still expand for about 1 ms, once the expansion time of the molecules is much longer, the detected clouds sizes are mainly contributed by the molecular expansion. Here, we assume the residual B-field do not affected the cloud size detection, which should be valid. In this way, we can extract the molecular temperature in a relatively accurate manner.

2.3 Removal of residual atoms

After magneto-association, the FMs coexist with the unassociated free atoms. As shown in Fig. 2.3, with the presence of free atoms, lifetime of the FMs is greatly

reduced. Thus, it is necessary to remove the residual atoms to create long-lived pure samples of the FMs. Previously, we applied a magnetic gradient pulse to realize the removal [102], utilizing the different magnetic dipole moments of the atoms and FMs. With carefully chosen gradient strength, the residual atoms can be rejected out from the trap while maintaining the FMs being trapped. However, due to the non zero magnetic dipole moments of the FMs, undesired motion of the molecular sample is induced by the magnetic gradient pulse. Moreover, this method can only remove the two atomic species simultaneously, which cannot meet our requirement of preparing mixtures of the FMs and ^{23}Na or ^{87}Rb atoms at certain conditions. Thus, we implement a new scheme combining microwave pulses and resonant lights to selectively remove the residual atoms. Enabled by this newly applied method, we have successfully investigated the collisions between the FMs with individual species of ^{23}Na and ^{87}Rb atoms to study the three- and four- body physics in our heteronuclear system. More details about the work can be found in Ref. [120].

The idea of the removal scheme is actually quite simple. As there are no cycling transitions for the residual atoms in $|F = 1, M_F = 1\rangle$ state, we first apply a microwave ARP to transfer the atoms to $|2, 2\rangle$ state and then pulse on a resonant light driving cycling transitions between the $|2, 2\rangle$ state and the $|3, 3\rangle$ state of the D_2 line. Here, we implement an ARP instead of a direct microwave π pulse as the transition energy is quite sensitive to the B-field. The typical fluctuation of our B-field of about 10 mG can shift the transition energy for 21 kHz, which is comparable to the $\sim$ 40 kHz Rabi frequency achieved. For each ARP, the span of the transition energy by ramping the B-field, as shown in Fig. 2.2 the stage III, is about 300 kHz in 75 μs with typical efficiency of $\sim$ 85%. Following each ARP is a 10 μs resonant light pulse to kick the $|2, 2\rangle$ state atoms out from the ODT. To fully remove the residual atoms, five such sequences are subsequently implemented, resulting in less than 0.1% atoms left within 450 μs. What's more, although the binding energy of the FMs is only about 0.15 MHz when the first

microwave pulse is applied, no obvious effects on the FMs are observed. Thus, the removal process should have little influence on the FMs.

2.4 Raman laser system

To transfer the FMs to the ground state, a stable Raman laser system was set up, as shown in Fig. 2.4. The two external cavity diode lasers (ECDL) operate near 1248 nm (pump laser) and 769 nm (dump laser). Originally, the 1248 nm laser is a quantum dot laser from Sacher and the 769 nm one is from Uniquanta. However, due to the limitations of available power and achieved linewidths, the two lasers are replace by TOPTICA TA Pro and DL Pro, with which the transfer efficiency increased from 80% to 93%. The output of each laser is spit to three parts, one is sent to the wavelength meter (WS7-60), one for laser locking and the other is used for STIRAP transfer. As the STIRAP requires phase coherence between the two largely detuned laser beams, the two lasers are locked to an ultra-low expansion high finesse optical cavity (ULE cavity) through Pound-Drever-Hall (PDH) technique [121], which will be described in details below.

As the pump light is out of the working range of our wavelength meter, we have to double its frequency to measure its absolute wavelength, as shown in Fig. 2.4(a). The zero order beam of the 110 MHz acoustic-optical-modulator (AOM) is focused to a frequency doubler ($LiNbO_3$ crystal) and a dichroic mirror is utilized to filter the non-doubled lights. Although the doubling efficiency is only 0.002% with an incident power of 210 mW, it is sufficient for the wavelength meter to monitor the laser frequency.

To matching the laser frequency to the cavity mode, the beams pass through AOMs in certain configurations before being coupled to the cavity. By tuning the driving frequencies of the AOMs, we can vary the laser frequencies while keep the laser locked to the cavity. To cover a whole free spectral range (FSR) of about 1.5 GHz, the 769 nm light passes through a 400 MHz AOM (bandwidth:

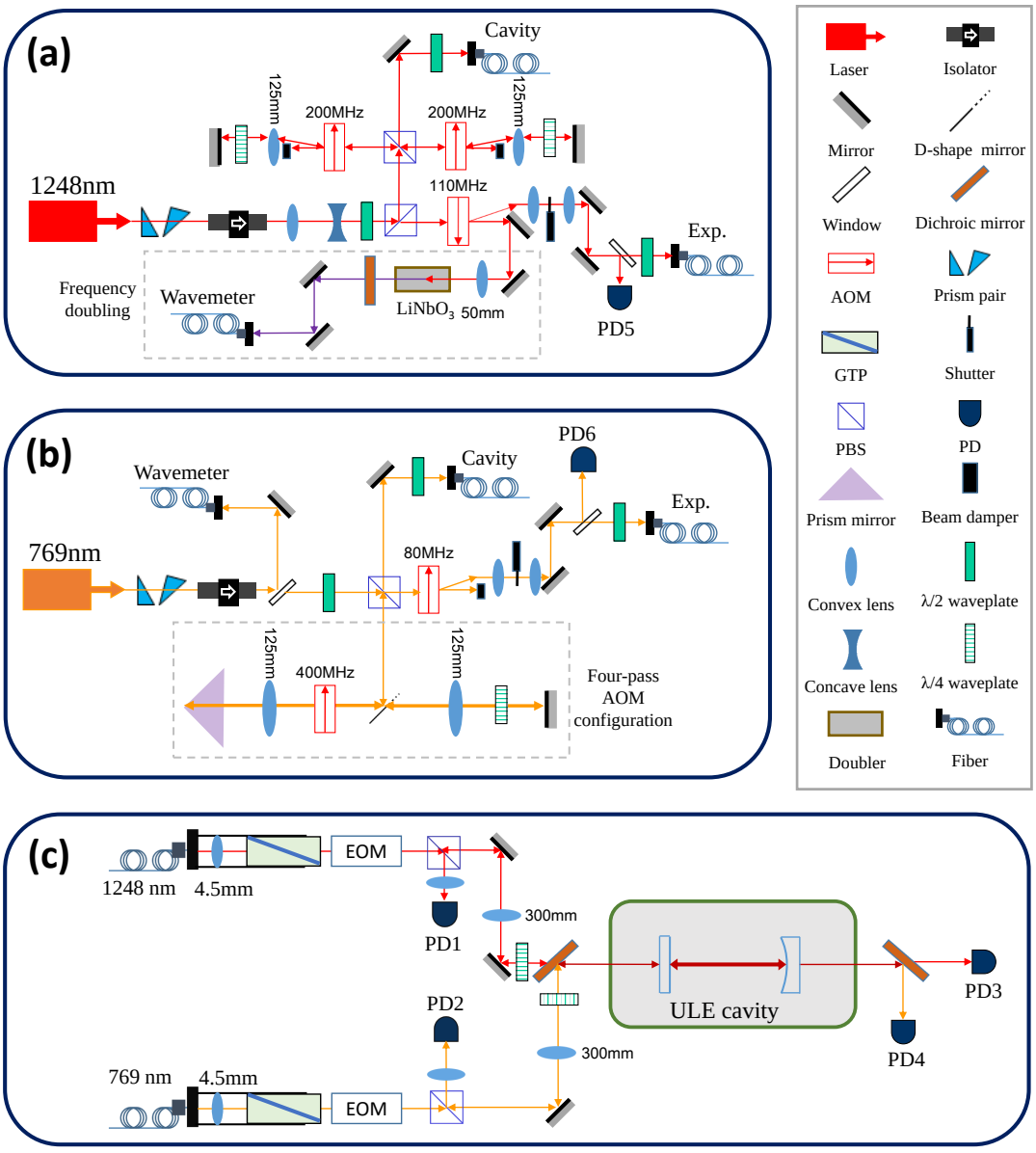

Figure 2.4: Layout of the Raman laser system. (a) The pump laser setup. The dashed box is the frequency doubling part to measure its absolute wavelength. (b) The dump laser setup. The dashed box is the four-pass AOM configuration for matching the dump light frequency to the cavity. (c) Optical layout near the ULE cavity for locking the lasers. The lights pulses for experiments are manipulated by the two AOMs on the paths to experiment and monitored by PD5 and PD6.

200 MHz) in a four-pass configuration [122]. The typical efficiency is higher than 10%, enough here as the light injected to the cavity is only 100 μW. Due to the

lack of high bandwidth AOMs, the 1248 nm lights goes through two 200 MHz AOMs, each in a double-pass configuration [123], as shown in Fig. 2.4(a).

2.4.1 The ULE cavity

To maintain phase coherence between the two laser beams with so large frequency difference, both lights are referred to a dual-wavelength coated ULE cavity (AT-Films 6010-4, custom cavity). The cavity is 100 mm long and in hemispherical configuration with the concave mirror of 500 mm radius of curvature. The reflection of the coating in the two wavelength ranges is higher than 99.985% [Fig. 2.5(a) and (b)], corresponding to a finesse over 21000 and a linewidth of 71 kHz. The cavity is supported by a Zerodur mounting block with four Viton balls in between to isolate the vibration, as shown in Fig. 2.5(c). The block is placed inside a vacuum chamber with the pressure maintained to 10^{-7} Torr and the temperature stabilized to 0.01 °C. Although the temperature is not set to the exact zero crossing point, the day-to-day drift of the cavity is less than 4 kHz by measuring the two-photon resonance of the molecular transitions.

To characterize the ULE cavity, a series of measurements were carried out. The layout shown in Fig. 2.6(a) was used to precisely measure the cavity FSR. Besides a locking light to lock the laser, a probe light, which was generated from the same laser but with frequency shifted for about 1.5 GHz from the locking light via AOMs, was also coupled to the cavity. When the frequency difference between the two lights is exactly a FSR of the cavity, maximum transmission is observed by PD2, as shown in Fig. 2.6(b) and (c). The FSR of the cavity was extracted to be 1.4969368(2) GHz for the pump light and 1.4972179(2) GHz for the dump light, corresponding to cavity lengths of 100.135 mm and 100.117 mm respectively.

To estimate the finesse of the cavity, cavity ring-down experiment was implemented. After locking the laser to the cavity, the light was shut down by turning off the AOM and the dynamic response of the light inside the cavity was mon-

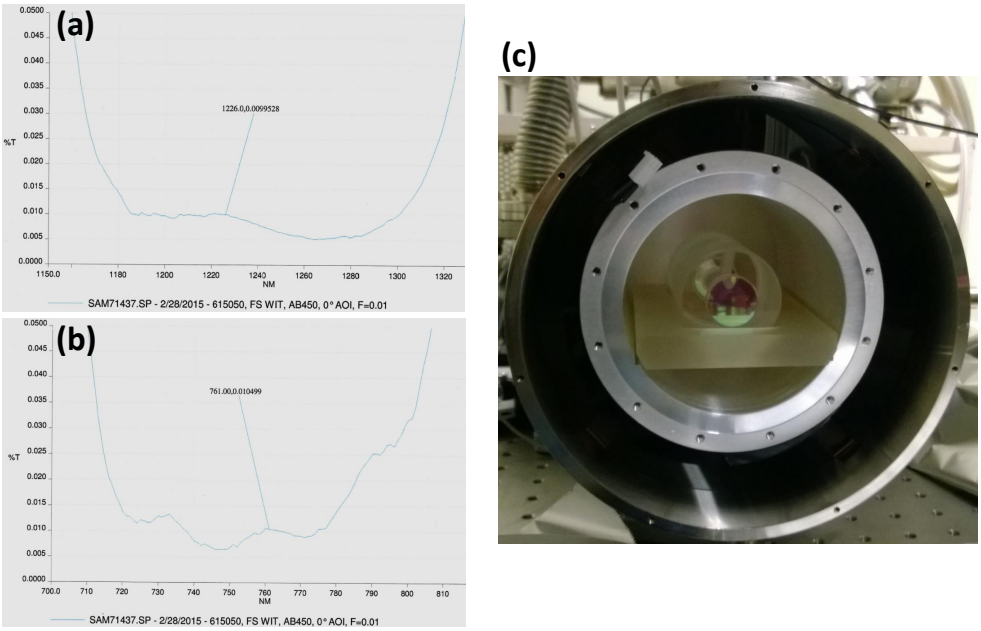

Figure 2.5: (a) and (b) the reflectivity of the cavity high-reflection coating near the two designed wavelength. (c) the setup of the ULE optical cavity.

itored through the transmission. Figure 2.7 demonstrates the ring-down signals for the two wavelength lights, extracting the photon lifetime inside the ULE cavity τ to be 3.094(4) μs and 2.740(6) μs. The reflections R, assumed to be the same for the two cavity mirrors, are

$$R = 1 - \frac{1}{c\tau} = 99.9892\% \text{ and } 99.9878\%, \tag{2.1}$$

and the finesses are

$$F = \frac{\pi\sqrt{R}}{1-R} = 29099 \text{ and } 25770, \tag{2.2}$$

correspondingly for the two wavelengths. The measured finesses are consistent with the data provided by the supplier. Together with the measured FSRs, the linewidths (full-width-at-half-maximum) of the cavity are extracted to be

$$\Delta v = \frac{FSR}{F} = 51.4 \text{ kHz and } 58.1 \text{ kHz}. \tag{2.3}$$

The narrow linewidth of the cavity makes it relatively easier to reducing the laser linewidths through referring to the cavity. To achieve laser linewidth of 1 kHz,

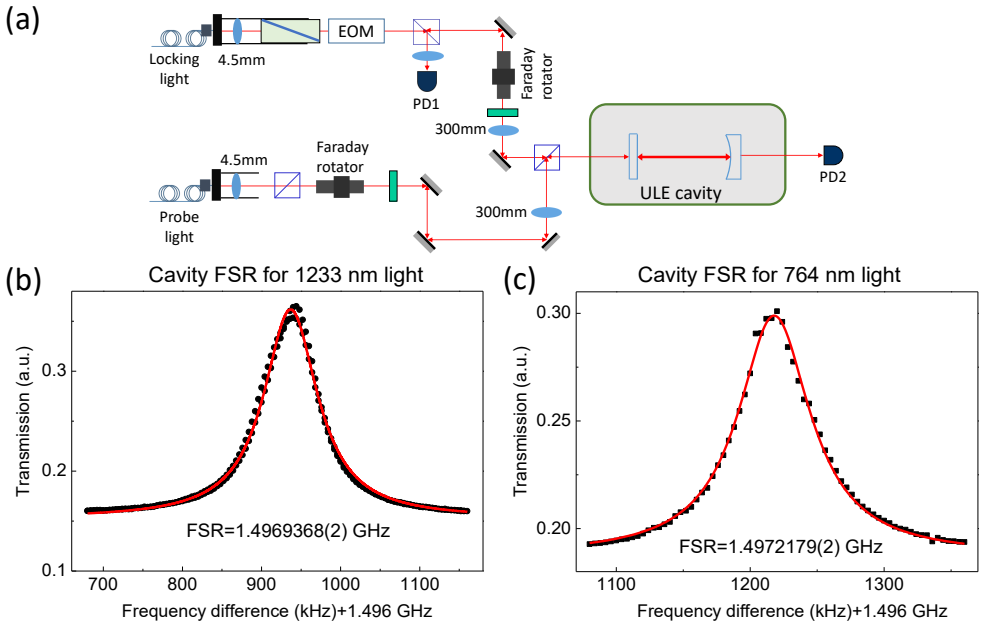

Figure 2.6: (a) Optical layout to precisely measure the cavity FSR. (b) and (c) signals of PD2 with respect to the frequency difference between the probe light and the locking light. Solid curves are Lorentz fittings to the data, from which the FSRs of the ULE cavity for the two wavelength lights are extracted.

which allows for long two-photon transfer duration up to 1 ms, the lower bound of the signal-to-noise ratio for locking is only 50. Thus, the narrow linewidth of the cavity benefits the transfer efficiency and resolution, as longer pulse typically results in narrower spectrum linewidth.

2.4.2 PDH locking

To build the prerequisite phase coherence between the two largely detuned lasers, the ULE cavity is supplied as a common reference and the frequency noise of the two laser is suppressed through the PDH locking. The PDH technique is a powerful tool used to stabilize the frequencies of lasers. There are many elegant reviews [124, 125, 126, 127] introducing the technique and the working principle, which will not be introduced here.

The locking scheme and experimental realization are illustrated in Fig. 2.8. A

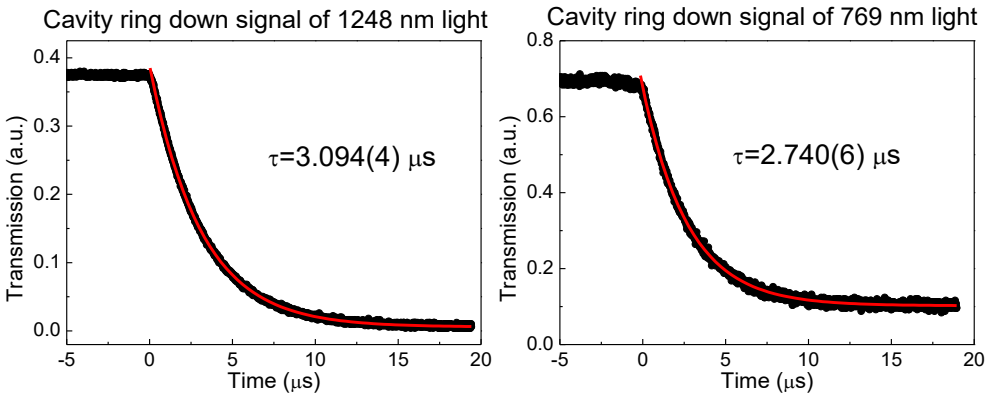

Figure 2.7: Cavity ring down signals to measure the two frequencies photon lifetime in the optical cavity, with which the cavity finesse can be extracted.

laser beam after frequency shifted by certain AOMs is carried to the cavity region via an optical fiber. After collimated (a bit converging) by a 4.5 mm aspherical lens, the laser beam passes through a Glan-Thompson prism to purify its polarization. Phase modulation is then imposed by an electro-optical modulator (EOM) driven by a 20 MHz RF signal. Aligning the light polarization to the optic axis of the EOM can greatly suppress the undesired amplitude modulation, which can induce fluctuation of the zero point of the error signal and thus affect the locking stability [128]. After the EOM, the light is sent to the ULE cavity with mode matching achieved through two mirrors and a $f = 300$ mm lens. The coupling efficiencies are typically better than 40% from the transmission signal monitored by PD2. The reflection signal after passing through the Faraday rotator for a second time is reflected by the PBS and collected by the fast PD.

To generate the error signal, the reflection signal is mixed with a 20 MHz local oscillation signal, whose phase is delayed by a coaxial cable (phase delay line) to realize phase matching. The undesired 20 MHz oscillation signal and higher order harmonics in the IF port of the mixer are filtered by a 15 MHz low pass filter. Left column of Fig. 2.9 shows the filtered error signal and the transmission signal with scanned laser frequency. The central peak corresponds to the main carrier while the other two are the sidebands generated by the phase modulation. As the

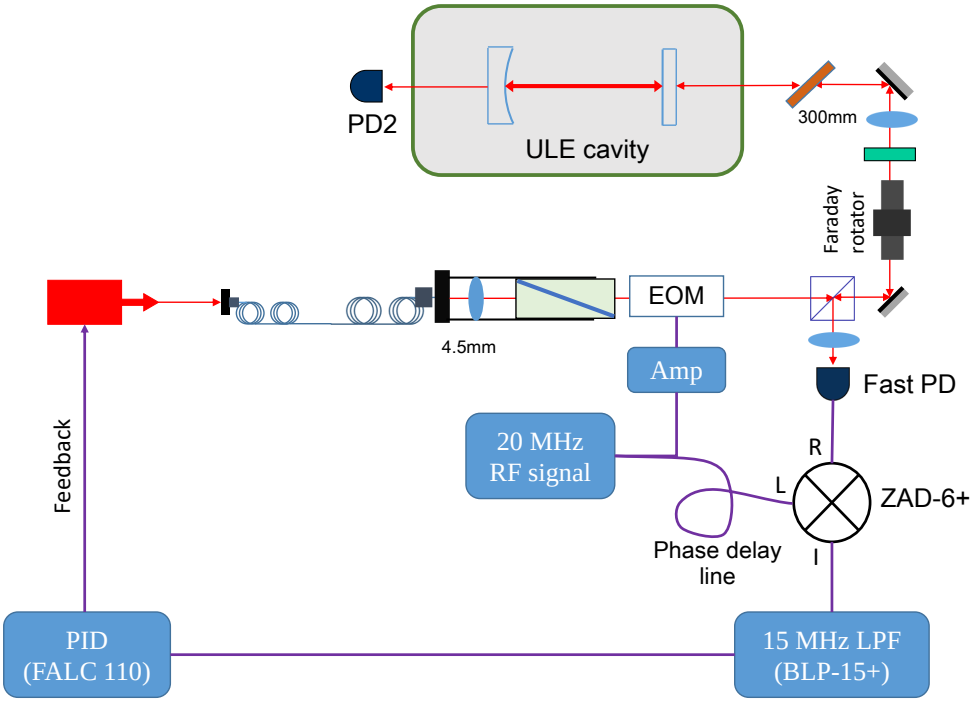

Figure 2.8: The schematic optical layout and electronic components to realize the PDH locking. The fast PD with bandwidth larger than 20 MHz is PDA10A (PDA10CF) from Thorlabs for the pump (dump) light. The phase delay line is used as a phase shifter to match the phase of the 20 MHz demodulation signal to the reflection signal detected by the fast PD. Mixing of the two signals via the frequency mixer generates the error signal.

slope of the central error signal has different sign from those of the two sidebands, the laser can be definitely locked to the central carrier instead of the sidebands with proper feedback polarity.

Finally, the error signal is sent to a fast PID controller to generate a high-bandwidth feedback signal to locking the laser by controlling both its PZT and current. As shown in the right column of Fig. 2.9, the light is locked to the cavity resonant peak as indicated by the largest transmission signal.

In order to optimize the PID parameters and evaluate the locking quality, it is more convenient to monitor the error signal in the frequency domain, i.e. the frequency noise spectral density (Fig. 2.10), instead of in the time domain

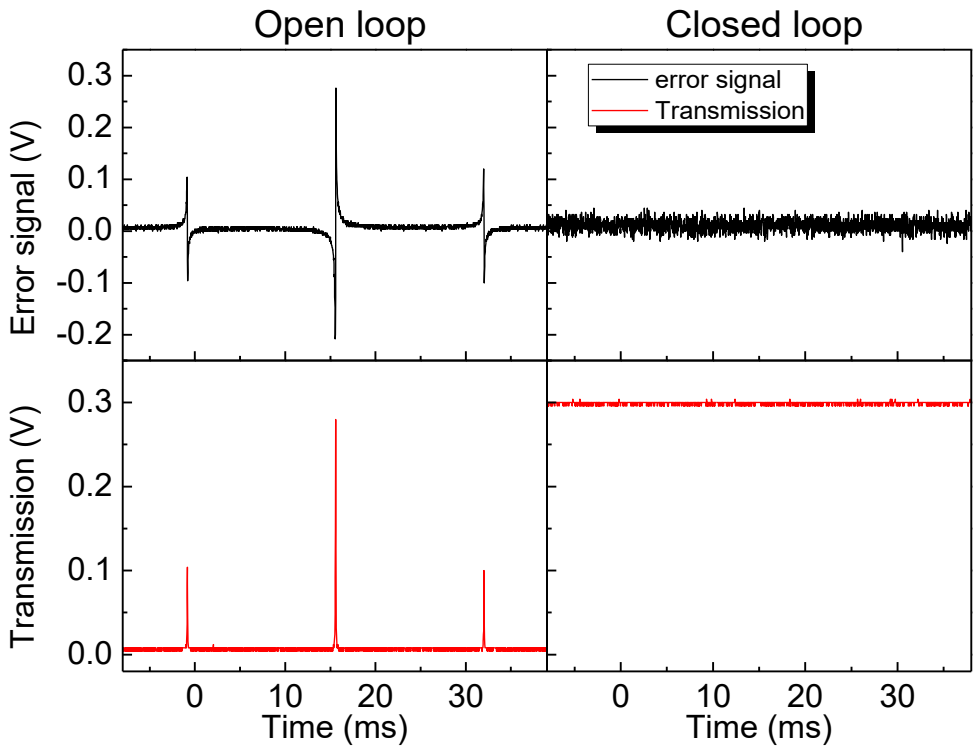

Figure 2.9: The error signal after the low pass filter for PDH locking and the transmission signal with the PID feedback loop open while laser frequency scanned and the laser locked.

(Fig. 2.9) [126, 129, 130]. The ULE cavity is served as a frequency discriminator transforming frequency noise of the light to the detected intensity fluctuation. Figure 2.10 shows the frequency noise spectral density of the two diode lasers obtained by sending the error signal to a spectrum analyzer (Keysight N9342C). The black ones are the background noise and the blue ones are the frequency noise of the free running lasers by keeping the laser resonant to the ULE cavity (with very weak and slow feedback). The criterion for optimizing the PID controller is to obtain large gain at low frequency and high feedback bandwidth, which indicates the limit below which the noise is suppressed. As shown in Fig. 2.10 by the red circles, the feedback bandwidths for the two diode lasers are as large as 1 MHz after optimizing the PID parameters and the frequency noise are greatly suppressed.

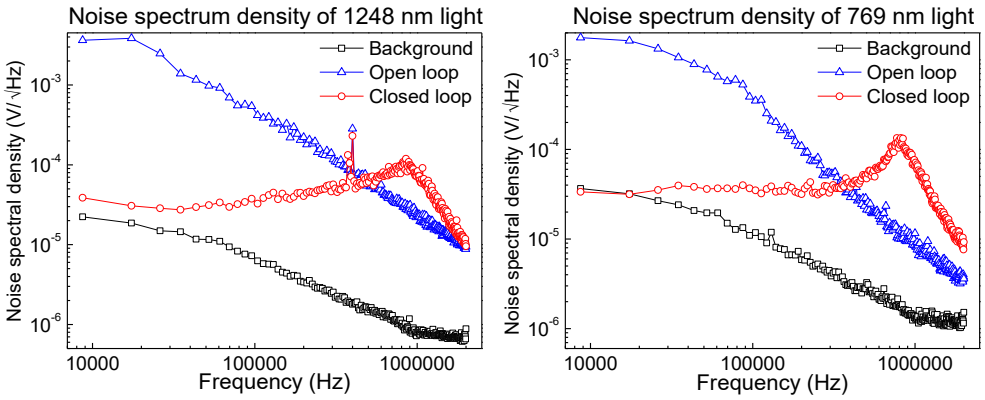

Figure 2.10: Noise spectral density of the two diode lasers with the injected lights off resonance (black square), on resonance with weak feedback (blue triangle) and tightly locked (red circle). The resonance peaks (broad) in the closed-loop spectrum indicate the positions of unity gain, from which the feedback bandwidths are extracted to be about 1 MHz. The narrow peaks in the spectrum of 1248 nm light are probably due to occasional resonance within the system.

To estimate the locked laser linewidths, the most accurate methods are through the heterodyne interference and the delayed self-heterodyne interference. However, due to the lack of another similar laser system for heterodyne interferometry and long optical fiber (> 300 km for a laser linewidth of 1 kHz) for delayed self-heterodyne interference, these methods are not feasible in our laboratory. As a trade-off, we evaluate how well the lasers are locked to the ULE cavity, i.e. the laser linewidths relative to the cavity, from the error signal. After closing the feedback, the error signals still have certain fluctuation, which represents the laser frequency deviation from the cavity resonance. The relation between the frequency deviation and the error signal is determined by the slope, D, of the error signal (Fig. 2.9 left column) near zero point

$$D = \frac{2\ V_{pp}}{\Delta v}. \tag{2.4}$$

Here, V_{pp} is the peak-to-peak voltage of the error signal with the loop opened and Δv is the cavity linewidth. With this relation, the noise in the error signal can be converted to the laser frequency fluctuation. Assuming Gaussian lineshape,

the laser linewidth (FWHM) relative to the ULE cavity can be extracted as [131]

$$\Delta_{\mathrm{FWHM}} = 2\sqrt{2\ln 2}\frac{V_{\mathrm{rms}}}{D}, \tag{2.5}$$

with V_{rms} the root-mean-square of the error signal after locking the laser (Fig. 2.9 right column). Applying this method, we estimate the linewidths of both Raman lasers to be about 1 kHz (5 kHz for the old ones). From the noise spectral density, the laser linewidths relative to the ULE cavity can also be extracted, once the transformation from the frequency noise to the voltage signal, i.e. the slope D, is know. However, limited by the resolution of the spectrum analyzer especially it lowest frequency limit of only 9 kHz, it is hard to accurately estimate the laser linewidth relative to the ULE cavity with this method.

Although we need to account the fluctuation of the ULE cavity itself to get the absolute laser linewidths, it is the relative linewidths of the two lasers that is more important in the two-photon Raman process. As the two lasers refer to the same cavity, the cavity fluctuation, which is common to the two lasers, should have minor effect on their relative linewidth. Thus, we just take the estimated linewidths to simulate the STIRAP process, which agrees well with our experiment (see Fig. 4.1).

2.5 High voltage electrodes

Although the ground-state ^{23}Na^{87}Rb molecules have permanent electric dipole moments, their orientations are randomly distributed in the lab frame, resulting in zero effective dipole moments. One way to induce effective dipole moments is by applying a static electric field (E-field), aligning the molecules along the E-field. In our experiment, the E-field is generated by two parallel Indium-Tin-Oxide (ITO) coated glass plates (80 mm$\times$23 mm$\times$0.7 mm), whose transmission for 1064 nm lights is lager than 85%. The two electrodes are placed outside the science cell along vertical direction and separated for about 25 mm from each other, as shown in Fig. 2.11. To achieve strong E-fields, the plates are

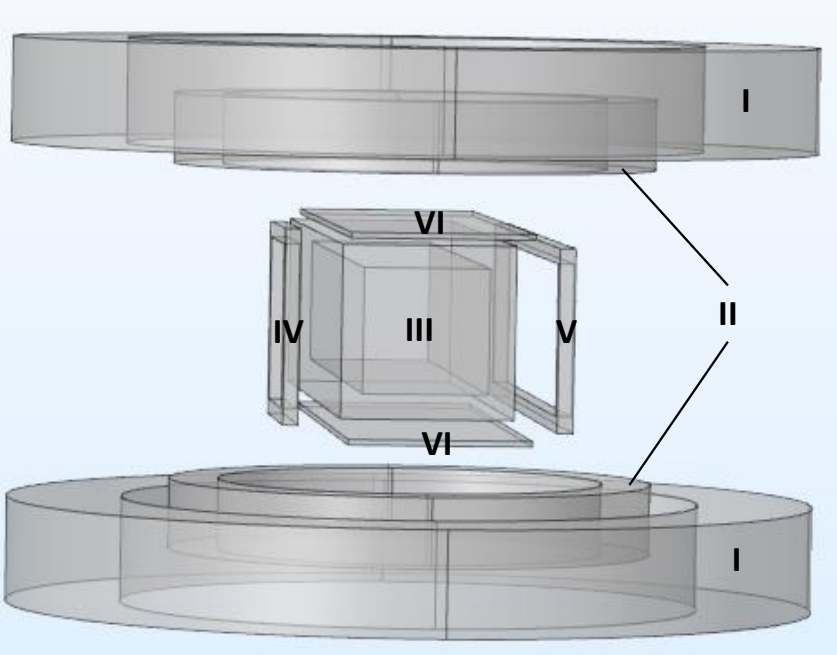

Figure 2.11: The setup of the electrodes with nearby conductors. **I**: bias coils; **II**: Stern-Gerlach coils; **III**: science cell; **IV** and **V**: loop antennas of different sizes for generating RF and microwave fields; **VI**: the electrodes of two ITO glass plates. Most of these conductors are grounded except for the bias coils when the E-field is applied.

connected to independent high voltage amplifiers (AMT-5B20) with maximum output voltage of ± 5 kV. The amplifiers have a fast slew rate of 360 V/μs and are controlled by two arbitrary waveform generators. Thus, we can generate a fast modulated E-field as well as a static one.

As the generated E-field at the sample position cannot be experimentally measured, we use the simulated values instead. For the simulation, the nearby conductors, most of which are grounded when the E-field is applied, are also taken into account. The simulation result with applied voltages of ± 0.75 kV is shown in Fig. 2.12, giving the E-field at the position of molecular sample to be 0.605 kV/cm along the vertical direction.

Obviously, there are certain drawbacks with the electrodes placed outside the glass cell. As the loop antenna, **V** in Fig. 2.11, is very close (less than 4.5 mm)

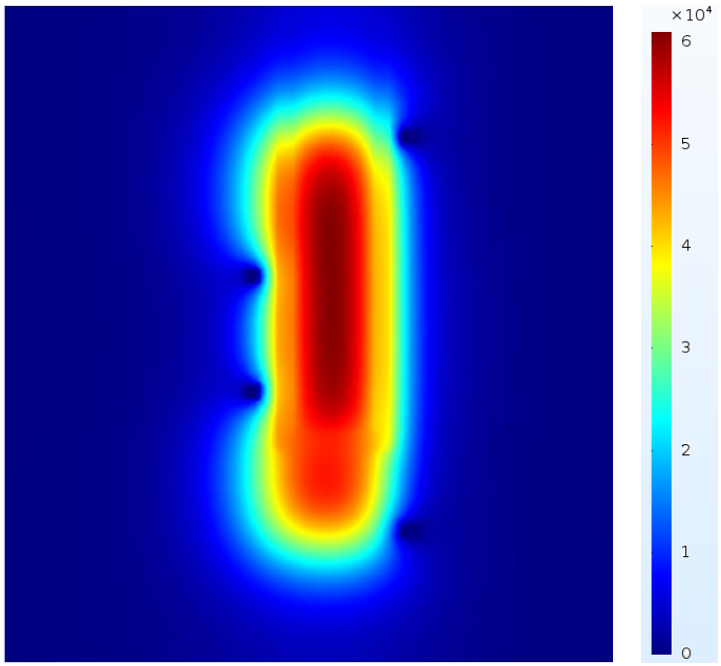

Figure 2.12: Simulated E-field at the center of the cell (looking down) with applied voltages of ±0.75 kV on the electrodes. The E-field strength along the vertical direction is color coded in unit of V/m. For the simulation, the nearby conductors are also considered.

to the edge of the plates, discharging between them can happen even with low applied voltage. The discharging was tested to emerge with applied voltages of ±3.5 kV before the electrodes were placed to the cell. However, another problem we encountered is the polarization of the glass cell, which do not relax back immediately after turning off the E-field. This phenomenon is observed through the sensitive two-photon spectrum. It is interesting to find that the polarization of the cell does not emerge with ±2 kV voltages (1.50 kV/cm E-field) imposed for 2 ms but happens with ±1.5 kV (1.15 kV/cm) E-field turned on for 20 ms. To avoid the problem, we limit the applied voltages within ±1.25 kV, corresponding to an E-field of 0.934 kV/cm. With this E-field, we can still successfully induce an effective dipole moment as large as 0.7 D.

□ End of chapter.

Chapter 3

Spectroscopy of $^{23}Na^{87}Rb$ Feshbach Molecules

The weakly-bound FMs, which are subjected to inelastic collisions and chemical reactions, have rather short lifetime. Furthermore, the large internuclear distance between the two atoms within the FM results in nearly zero electric dipole moments. Thus, it is necessary to transfer the molecules to the singlet rovibrational ground state, where chemical reaction is energetic forbidden and large permanent electric dipole moments can be obtained. As depicted in Sec. 1.3, the intermediate state for an efficient STRIAP transfer must strongly couple to both the Feshbach state and the ground state. The created FM is actually a superposition state of the molecular bound state (close channel) and the atomic scattering state (open channel) [102], especially near the Feshbach resonance. As bound-bound transitions are typically much stronger than free-bound couplings, it is favorable to have the FM with a large close-channel fraction to achieve a strong coupling to the intermediate state. Thus, it is favorable to apply the STIRAP under a B-field far away from the Feshbach resonance. In our experiments, the B-field for the spectroscopy and the STIRAP transfer is about 335.6 G, where the FM is close channel dominated [14]. On the other hand, identifying a suitable intermediate state is of great importance for the STIRAP transfer, which will be elaborately described in this chapter. The major results of this chapter can be found in the

published paper Ref. [132].

3.1 Requirements of the intermediate state

For the STIRAP transfer, searching a suitable intermediate state is not trivial. To achieve strong couplings to both the Feshbach state and the ground state, the intermediate state must satisfy certain requirements, as listed below specifying to our ^{23}Na^{87}Rb molecule.

Firstly, the intermediate state must be strongly singlet-triplet mixed. As the Feshbach resonance used to create the FMs corresponds to the last vibrational level of the $a\,^3\Sigma^+$ potential [101, 102], the FMs have predominant characteristic of spin triplet. While, the ground state is purely singlet. Due to the forbidden electric dipole transitions between spin singlet and spin triplet states, the intermediate state must have significant singlet and triplet components simultaneously.

Secondly, as the FM is weakly-bound while the ground state has a large binding energy of about 5000 cm^{-1} [96], the spatial wavefunctions of the two states greatly mismatch, as shown in Fig. 3.1 their theoretical wavefunctions. To achieve strong couplings to both states, the Franck-Condon factors (FCFs), representing the vibrational wavefunction overlaps between the intermediate state and the two states, must be large enough.

Finally, the hyperfine splittings of the intermediate state should be large enough to have fully resolvable hyperfine levels. An ideal STIRAP only involves three states as described in Sec. 1.3. The existence of a second intermediate level can provide another path between the Feshbach state and the ground state, which may induce destructive interference with the original one and destroy the transfer process [105, 133, 134]. Thus, the hyperfine splittings of the intermediate state should be larger than its natural linewidth, making its hyperfine structure fully resolvable to avoid simultaneously couplings to other hyperfine levels.

These prerequisites provide criteria for identifying suitable intermediate states.

Besides, the searching region is also greatly reduced as these requirements are more likely to be fulfilled only in certain areas of the excited potentials, which will be discussed in details below.

3.2 Potentials of $^{23}Na^{87}Rb$ molecules

Before referring to the experiment on the spectroscopy, it is necessary to introduce the molecular structure of ^{23}Na^{87}Rb molecules first and specify the regions where excited states have higher possibilities to satisfy the requirements. Here, only the potential of energy curves (PECs) below the Na($3\,^2S_{1/2}$)+Rb($5\,^2P_{3/2}$) asymptotic limit are discussed, as illustrated in Fig. 3.1.

Below the asymptotic limit, there are two ground potentials, a singlet one $X\,^1\Sigma^+$ with total electronic spin $\mathbf{S} = 0$ and a triplet one $a\,^3\Sigma^+$ with $\mathbf{S} = 1$. Both potentials have electronic orbital angular momentum $\mathbf{L} = 0$. In Hund's case (a), there are four excited PECs denoted as $A\,^1\Sigma^+$, $B\,^1\Pi$ for singlet and $b\,^3\Pi$, $c\,^3\Sigma^+$ for triplet. Here, the capital characters Σ and Π label the projections of $\mathbf{L}$ to the internuclear axis, $\mathbf{\Lambda}$. In hund's case (c), due to the spin-orbit couplings (SOCs), the coupled $\mathbf{L}$ and $\mathbf{S}$ split the four potentials into eight including two $\mathbf{\Omega} = 0^+$ ($A\,^1\Sigma^+$ and $b\,^3\Pi$), two $\mathbf{\Omega} = 0^-$ ($b\,^3\Pi$ and $c\,^3\Sigma^+$), three $\mathbf{\Omega} = 1$ ($b\,^3\Pi$, $c\,^3\Sigma^+$ and $B\,^1\Pi$), and one $\mathbf{\Omega} = 2$ ($b\,^3\Pi$) [135, 136]. Here, $\mathbf{\Omega} = \mathbf{\Lambda} + \mathbf{\Sigma}$ is the projection of the total electronic angular momentum, while $\mathbf{\Sigma}$ (distinguishing from the potential label Σ^+) is the projection of $\mathbf{S}$. To discriminate the spin-orbit coupled potentials with the same $\mathbf{\Omega}$, say the $\mathbf{\Omega} = 0^+$ potential from $A\,^1\Sigma^+$ will be denoted as $A(0^+)$ hereafter. Figure 3.1 shows the potentials of both Hund's case (a) and Hund's case (c) (not labeled). When the rotation of the nuclei, $\mathbf{N}$, is considered, $\mathbf{J} = \mathbf{L} + \mathbf{S} + \mathbf{N}$ is the total angular momentum of the molecules with ignored nuclear spins.

Thanks to previous studies on ^{23}Na^{87}Rb molecular spectrum, these PECs are well studied and reconstructed, including the ground potentials [96, 141, 142,

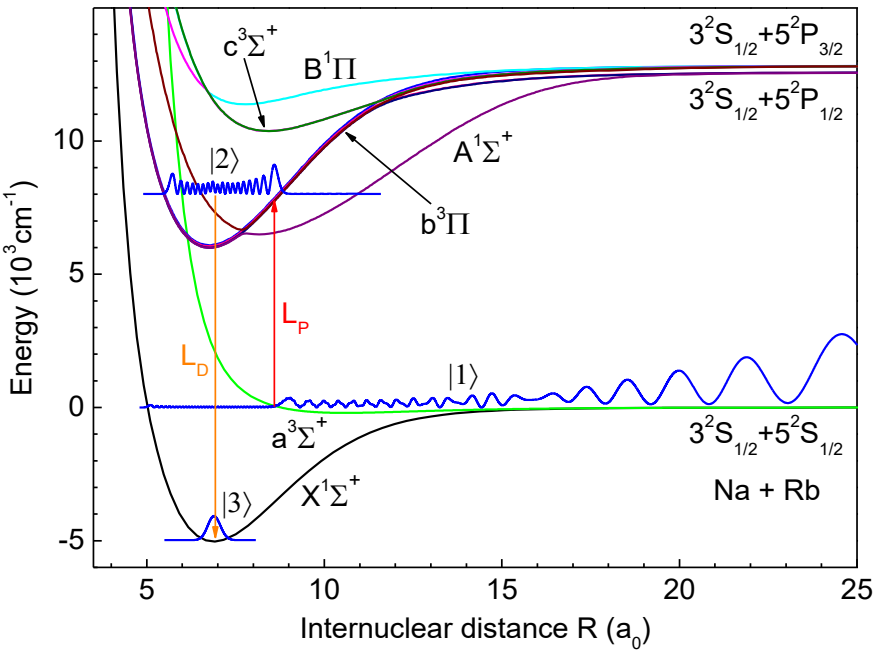

Figure 3.1: The potential of energy curves of ^{23}Na^{87}Rb molecule below the Na($3\,^2S_{1/2}$)+Rb($5\,^2P_{3/2}$) dissociation limit. Both the Hund's case (a) and the SOC (Hund's case (c), not labeled) potentials are plotted in the figure. The two electronic ground potentials are reconstructed from Ref. [96]. The PECs of $A\,^1\Sigma^+$ and $b\,^3\Pi$ as well as their SOC are taken from Ref. [137]. The $B\,^1\Pi$ potential is from Ref. [138] and the $c\,^3\Sigma^+$ potential is a computed one [139]. The other SOCs are unknown even theoretically, and shown here is taken as those for KRb [140]. The vibrational wavefunctions of the Feshbach state and the singlet ground state are also plotted, labeled as $|1\rangle$ and $|3\rangle$ respectively. The excited state wavefunction $|2\rangle$ shown here is that of the intermediate state used for STIRAP in our experiments.

143] and the excited ones [137, 138, 144]. These previous results make our identification of suitable intermediate states much easier. To achieve singlet-triplet mixing, the excited states should either be strongly $A\,^1\Sigma^+-b\,^3\Pi$ mixed or $B\,^1\Pi-c\,^3\Sigma^+$ coupled. The $A\,^1\Sigma^+-b\,^3\Pi$ coupled states was successfully applied to create the ground-state RbCs molecule [80, 145], while the $B\,^1\Pi-c\,^3\Sigma^+$ mixing scheme was implemented in KRb molecule [69, 99] and NaK system [79, 146]. As for ^{23}Na^{87}Rb molecules, states with strong $A\,^1\Sigma^+-b\,^3\Pi$ mixed character have

already been detected in Ref. [137, 144], where the SOC interaction was also precisely constructed. Guided by these studies, we focused our searching mainly on $A\,^1\Sigma^+ - b\,^3\Pi$ coupled states and successfully identified a suitable intermediate state [132], through which STIRAP with efficiency up to 93% has been achieved. At the end of this chapter, our exploration of $B\,^1\Pi - c\,^3\Sigma^+$ mixed states is also briefly introduced with several observed levels satisfying all the requirements. Thus, these levels should also support efficient transfers even though they are not implemented in our experiment.

3.3 The $A\,^1\Sigma^+ - b\,^3\Pi$ mixed states

Although the vibrational states with $A\,^1\Sigma^+ - b\,^3\Pi$ mixing are observed in Ref. [144, 137], the resolutions were not sufficient to resolve their hyperfine structure (HFS). What's more, transitions between these states and the Feshbach state are also not studied. Thus, more detailed investigations on the molecular spectrum is still necessary. Before our experimental studies, our theoretical collaborators, Romain Vexiau, Nadia Bouloufa-Maafa and Olivier Dulieu, have modeled these excited states theoretically. Based on Ref. [137], they set up a four-coupled-channel Hamiltonian [147] accounting the dominant SOC between the $A(0^+)$ and $b(0^+)$ components as well as the weak hyperfine interactions with the other $b(1)$ and $b(2)$ states. As the $b(2)$ component cannot directly reach the singlet rovibrational ground state, it is irrelevant here. The energies of the coupled states are extracted by diagonalizing the Hamiltonian matrix [147] and each vibrational state is assigned by a quantum number v'. To calculate the transition dipole moments (TDMs) between these vibrational states and the Feshbach state, and the ground state, the R-dependent electronic TDMs functions from their own quantum chemistry calculations are used [139]. Figure 3.2 displays the calculated TDMs with the shadowed region explored in our experiment, where both the pump and the dump TDMs have significant magnitude, which are sufficient to

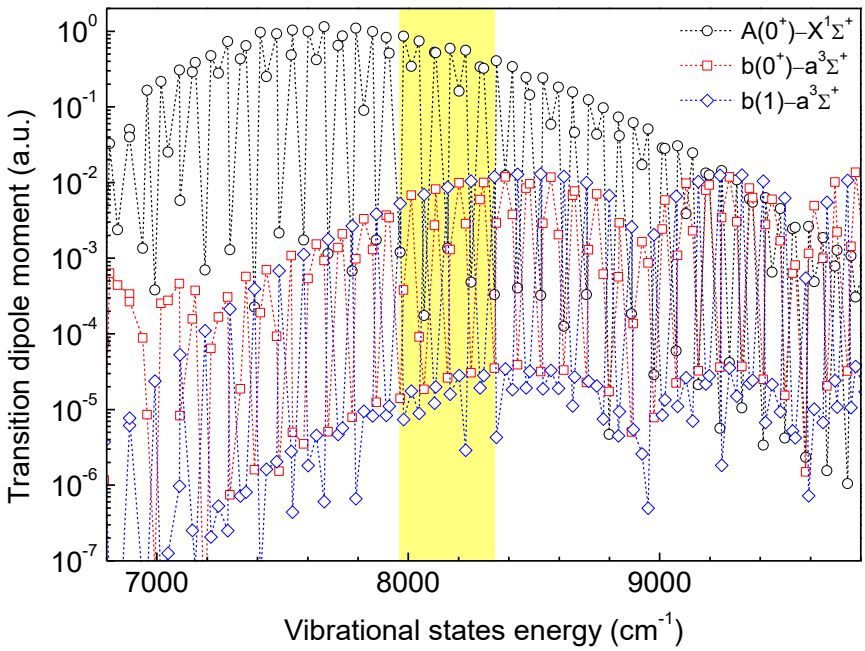

Figure 3.2: Theoretically calculated TDMs of the $A\,^1\Sigma^+ - b\,^3\Pi$ mixed vibrational states to the singlet ground state $[A(0^+) - X\,^1\Sigma^+]$ and the Feshbach state $[b(0^+) - a\,^3\Sigma^+$ and $b(1) - a\,^3\Sigma^+]$, while the rotational and hyperfine structures are ignored. Each point denotes a mixed vibrational state with x-axis their energies relative to the $\mathrm{Na}(3\,^2S_{1/2}) + \mathrm{Rb}(5\,^2S_{1/2})$ asymptotic limit. The shadowed region represents the area explored in our experiment.

realize large Rabi frequencies for efficient STIRAP transfer.

From the coupled-channel calculation, we also extracted the singlet/triplet fraction of each vibrational state. Table 3.1 shows the components fraction of the concerned vibrational states (Fig. 3.2). Many of these states are strongly singlet-triplet mixed, demonstrated as significant fractions of both $A(0)$ and $b(0)$ components. Thus, once these states possess resolvable HFS, they should be suitable for efficient STIRAPs.

For the $A\,^1\Sigma^+ - b\,^3\Pi$ mixed states, the singlet-triplet coupling is mainly achieved through the SOC between the $A(0^+)$ and $b(0^+)$ potentials, which have the same $\mathbf{\Omega} = 0^+$. However, pure $\mathbf{\Omega} = 0$ states typically have unresolved HFS due to zero electronic angular momentum projection. The hyperfine splitting mainly results

Table 3.1: Calculated components fraction of each observed vibrational state with respect to the $A(0)$, $b(0)$ and $b(1)$ SOC potentials. Here, the $b(2)$ potential is ignored. The comparison between the extracted positions and the theoretically predicted ones of the observed vibrational states is also demonstrated. Note that the two vibrational states $v' = 54, 56$ are not observed due to their weak couplings to the Feshbach state.

v'	$A_0(\%)$	$b_0(\%)$	$b_1(\%)$	Exp.(cm^{-1})	Th.(cm^{-1})
53	0	0	100	7967.84	7967.80
54	97	3	0	-	7981.77
55	5	95	0	8012.72	8012.75
56	95	5	0	-	8043.69
57	0	0	100	8062.46	8062.40
58	77	23	0	8014.66	8014.67
59	24	76	100	8109.00	8109.02
60	0	0	100	8156.54	8156.48
61	95	5	0	8166.42	8166.43
62	6	94	0	8202.64	8202.64
63	97	3	0	8228.93	8228.91
64	0	0	100	8250.04	8249.98
65	64	36	100	8285.50	8285.46
66	38	62	0	8300.15	8300.10
67	0	0	100	8343.01	8342.89

from the weak interactions within nuclear spins and nuclei rotation. Thus, in order to have resolved HFS, the states should also have significant $b(1)$ component, which is the case for the intermediate level used in RbCs systems [145]. However, from the calculated component fractions, non of the vibrational states in Table 3.1 possesses these properties simultaneously. Whereas, our experiments happened to find a fully resolved HFS of the $v' = 55$ state. The anomalously large hyperfine splitting results from coupling between the $b(0^+)$ and $b(0^-)$ states [148], which will be discussed in details below.

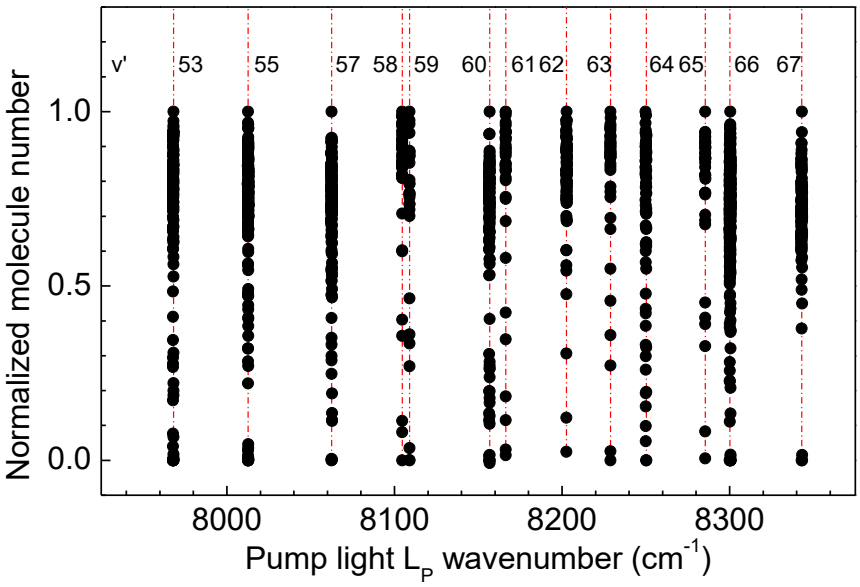

Figure 3.3: One-photon loss spectrum of the observed $A\,^1\Sigma^+ - b\,^3\Pi$ mixed vibrational states, ranging from v'=53 to v'=67. The black dots are experimental data and the vertical dot-dashed lines are the predicted positions. Several vibrational states are not observed due to weak couplings to the Feshbach state.

3.3.1 The $A\,^1\Sigma^+ - b\,^3\Pi$ mixed vibrational states

To identify suitable excited states, high-resolution one-photon loss spectrum is carried out with precision up to HFS level. The weakly-bound FMs are irradiated by the pump light, L_P, under a B-field of about 335.6 G. In this case, the excited states manifest as discrete losses of the FMs when L_P is on resonance. Figure 3.3 shows the spectrum covering the vibrational states of interest as indicated in Fig. 3.2. The positions of all the observed states agree with the calculated ones with corresponding deviations less than 4 GHz. As shown in Table 3.1, these states can be classified into two types based on their component fractions, one dominated by $\mathbf{\Omega} = 0$ potential and the other with major $\mathbf{\Omega} = 1$ component.

When the molecular rotation is considered, certain parity selection rule should be obeyed. Besides the rotational selection rule $\Delta J = 0, \pm 1$, electric dipole transitions only couple states with different parity. While, the Feshbach state dominated by the molecular close channel $a\,^3\Sigma^+ \,|v = 21, J = 1\rangle$ has a total parity

of "+", which is the same as the singlet rovibrational ground state. Thus, the total parity of the excited states must be "−". Starting from the Feshbach state, the accessible rotational levels of different $\mathbf{\Omega}$ are: for 0^+ states, $J' = 1$ is the only allowed rotational level; for 0^- states, both $J' = 0$ and 2 can be populated; for 1 states, $J' = 1, 2$ levels are allowed. Hereafter, for better distinguishing the labels, the quantum numbers for excited intermediate states are denoted with an extra prime symbol ($'$). Among these rotational levels, only the $J' = 1$ levels can be coupled to the singlet rovibrational ground state.

With the atomic nuclear spins ($I_{\mathrm{Na}} = I_{\mathrm{Rb}} = 3/2$) taken into account, the rotational selection rules $\Delta M_J = 0, \pm 1$ change to $\Delta M_F = 0, \pm 1$ corresponding to light polarization of $\pi, \sigma^{\pm}$. Here, M_J is the projection of J to the quantization axis provided by the B-field and M_F is the projection of the total molecular angular momentum $\mathbf{F} = \mathbf{J} + \mathbf{I}_{\mathrm{Na}} + \mathbf{I}_{\mathrm{Rb}}$. As the Feshbach state has $M_F = 2$, the accessible hyperfine levels of the excited states are $M_F' = 1, 2, 3$ with L_P of σ^-, π and σ^+ polarization respectively. For the singlet rovibrational ground state, the hyperfine level with lowest energy is $M_F = 3$ under a B-field of 335.6 G, thus Raman beams with π/σ^- or σ^+/π (pump/dump) polarization combinations can directly transfer FMs to the absolute ground state. Note that, with the Raman beams co-propagate horizontally (perpendicular to the B-field), σ^- and σ^+ polarizations always coexist.

3.3.2 Hyperfine structures of the $A\,^1\Sigma^+ - b\,^3\Pi$ mixed states

Table 3.1 shows that the observed vibrational states are dominated by either $\Omega = 0$ component, including $A(0)$ and $b(0)$ potentials, or $\Omega = 1$ component. These two types of states result in distinct HFSs as a result of their different hyperfine coupling strengths. However, there happens to be a $\Omega = 0$ dominant state in the region of interest with anomalously large hyperfine splitting. Thus, it is a perfect intermediate state for STIRAP.

The $b(1)$ states

For states with significant $\Omega = 1$ character, the hyperfine interaction is strong enough to induce fully resolved HFS. Figure 3.4 shows the observed HFS of the $|v' = 60\rangle$ state, which is a typical $\Omega = 1$ dominated state. Rotational series of both $J' = 1$ [Fig. 3.4(a)] and $J' = 2$ [Fig. 3.4(b)] are observed, consistent with the rotational selection rules as discussed above. For both rotational series, the hyperfine sub-levels are all distinguished without any ambiguity. Actually, the $|v' = 60, J' = 1\rangle$ level is our primary candidate for the intermediate state. Due to the favorable FCF, it can strongly couple to the ground state even with only a small singlet component. Our calculation indicates comparable transition strength to the pump one even the singlet fraction is only 0.001%. However, even with the position of the singlet ground state precisely located by the two-photon spectrum through the $|v' = 59, J' = 1\rangle$ level and the highest L_D power available, no two-photon signal was ever observed through this state. Thus, the $v' = 60$ state should have too small singlet component, if it has, to achieve strong enough coupling to the ground state.

To interpret the observed HFS, our collaborators developed an effective Hamiltonian $\mathbf{H}^{\text{eff}}$ by prompting the asymptotic model [149] in the spin-decoupled basis $|\alpha\rangle \equiv |J', \Omega, M'_J; I_{\text{Na}}, m_I^{\text{Na}}; I_{\text{Rb}}, m_I^{\text{Rb}}\rangle$. In a perturbative way, the $\mathbf{H}^{\text{eff}}$ is written as

$$\begin{aligned} H^{\text{eff}} &= E_{v',J'} + \omega_{\text{Na}} I_{\text{Na}} H_{\text{hfs}}(\text{Na}) + \omega_{\text{Rb}} I_{\text{Rb}} H_{\text{hfs}}(\text{Rb}) \\ &\quad + g_S \mu_B \mathbf{S} \cdot \mathbf{B} + g_L \mu_B \mathbf{L} \cdot \mathbf{B} + \frac{\mathbf{N}^2}{2\mu R^2}, \end{aligned} \tag{3.1}$$

where $E_{v',J'}$ is the bare energy of the rovibrational state, ω_i (i=Na,Rb) is the hyperfine coupling constant, g_S and g_L are the electronic spin and orbital g-factors, and N is the mechanical rotation of the molecule. In this model, the couplings between different electronic, vibrational and rotational states are ignored, i.e. J' and Ω are still good quantum number. Furthermore, the hyperfine interactions H_{hfs} are only taken to the first order.

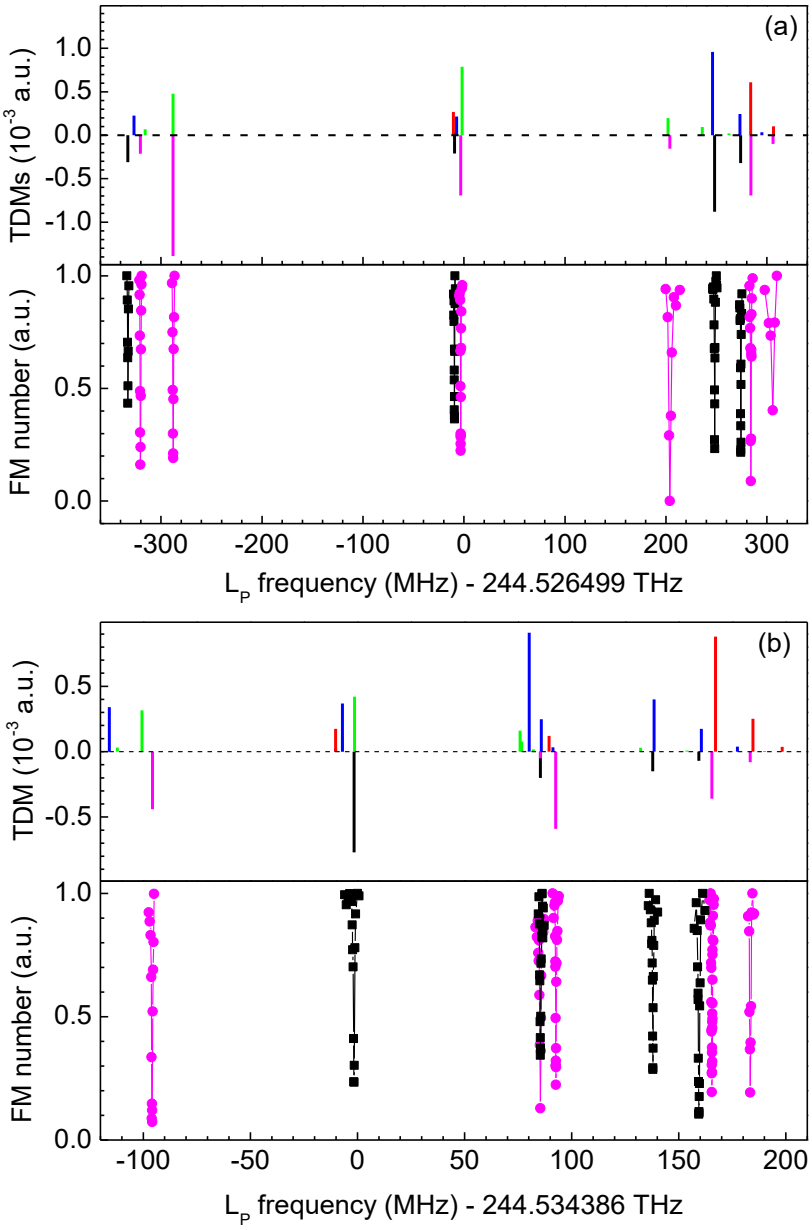

Figure 3.4: HFS of the $|v' = 60\rangle$ state with (a) $J' = 1$ and (b) $J' = 2$. In lower panels, black (pink) dots are experimental data with π ($\sigma^{\pm}$) polarized light. The extracted positions and TDMs of the hyperfine levels are shown as the negative bars (black and pink) in upper panels. The positive color-coded vertical bars indicate the theoretical predicted positions and TDMs of the hyperfine levels with $M'_F = 1$ in green, $M'_F = 2$ in blue and $M'_F = 3$ in red. The lifetime of the rovibrational state is extracted to be 404 ns (see Sec. 3.3.3).

Fitting the measured positions of the hyperfine levels of the $J' = 1$ state with the eigenenergies of H^{eff}, reasonable agreement has already been achieved by adjusting the two hyperfine coupling constants only. This leads to $\omega_{\text{Na}} = 23.9$ MHz and $\omega_{\text{Rb}} = 86.2$ MHz. Although the transition strengths and the hyperfine levels of $J' = 2$ are not included in the fitting procedure, the theoretical values are consistent with the experimental measurements, as shown in Fig. 3.4 the comparison between the calculation and the experiments.

The $A(0^+) - b(0^+)$ states

As for the other vibrational states with dominant $\Omega = 0$ fraction, the hyperfine splitting is typically much smaller due to zero electronic angular momentum projection. As shown in Fig. 3.5 the HFS of the $|v' = 59, J' = 1\rangle$ level, the hyperfine splittings are smaller than their natural linewidth, resulting in unresolved HFS. The whole HFS spans of only about 10 MHz, which is 60 times smaller than the $|v' = 60, J' = 1\rangle$ case, and only two loss peaks are distinguished. Although the unresolved HFS prohibits the level to be a suitable intermediate state for transfer, its significant $A\,^1\Sigma^+$ component as large as 24% (Table 3.1) results in strong coupling to the singlet ground state. Indeed, the first successful locating of the ground state was implemented with this level through the two-photon spectroscopy.

In principle, the HFS of the $|v' = 59, J' = 1\rangle$ level could also be interpreted by the effective Hamiltonian in Eq. 3.1. However, for $\Omega = 0$, all the terms in the equation vanish and second-order terms, including the interactions of the nuclear quadrupole moments, should be included. Considering the unresolved hyperfine structure observed, it is unworthy to implement the calculation, which needs a vast number of parameters to describe the second-order interactions. The vertical bars in Fig. 3.5 are the predicted positions of the asymptotic model [149], which is consistent with the span of the HFS.

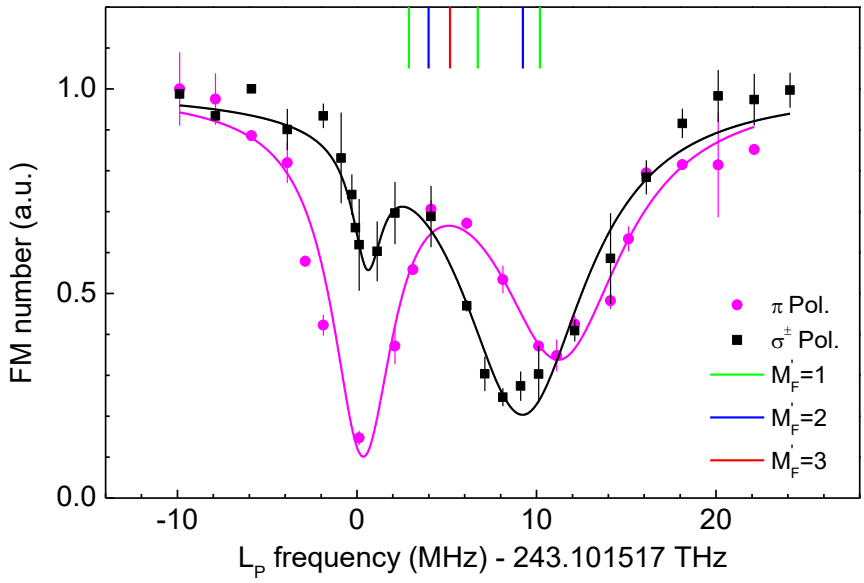

Figure 3.5: HFS of the $|v' = 59, J' = 1\rangle$ state with dominant $\Omega = 0$ components. The data is fitted with Lorentz lineshapes as shown by the color curves correspondingly. The notations of the vertical bars are the same as in Fig. 3.4.

The $0^+ - 0^-$ mixed state

Most of the other vibrational states listed in Table 3.1 have similar characteristics as either the $v' = 59$ state or the $v' = 60$ state. Following our previous discussions, non of the observed vibrational states should be suitable for the STIRAP. They have either no significant singlet component for coupling to the ground state as $|v' = 60\rangle$ or no $\Omega = 1$ character to have resolvable HFS like $|v' = 59\rangle$. Fortunately, in the region of interest, we observed an anomalously large hyperfine splitting in a $\Omega = 0$ dominated state $|v' = 55, J' = 1\rangle$. As shown in Fig. 3.6, the HFS spans over a wide range of about 2 GHz, even larger than the $\Omega = 1$ states (Fig. 3.4). Furthermore, all the hyperfine levels are well resolved, especially those on the two sides.

A more detailed study attributes the unusual large hyperfine splitting of the $|v' = 55, J' = 1\rangle$ level to the anomalous coupling between adjacent $\Omega = 0^+$ and $\Omega = 0^-$ components, which was observed recently for the first time in Rb_2

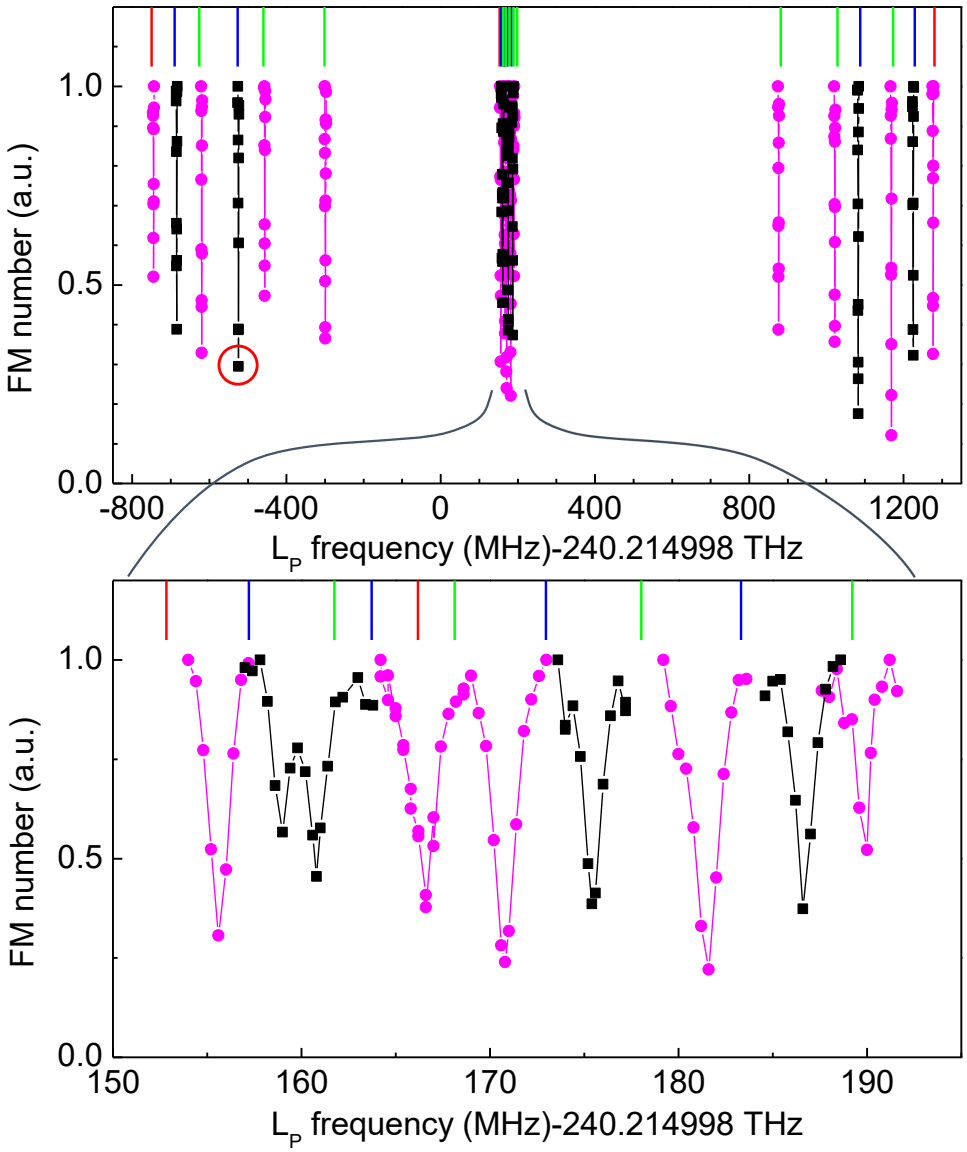

Figure 3.6: High-resolution spectrum of the $|v' = 55, J' = 1\rangle$ state with 21 hyperfine levels fully resolved. Up panel: overall hyperfine structure with an anomalously large hyperfine splitting spanning over 2 GHz due to the coupling between the 0^+ and 0^- states. Bottom panel: details of the central group lines. The vertical bars indicate the hyperfine positions from theoretical calculation with the same notions as in Fig. 3.4. The red open circle marks the hyperfine level with the largest coupling strength to the Feshbach state. It is also the level utilized for the STIRAP transfer in our experiment.

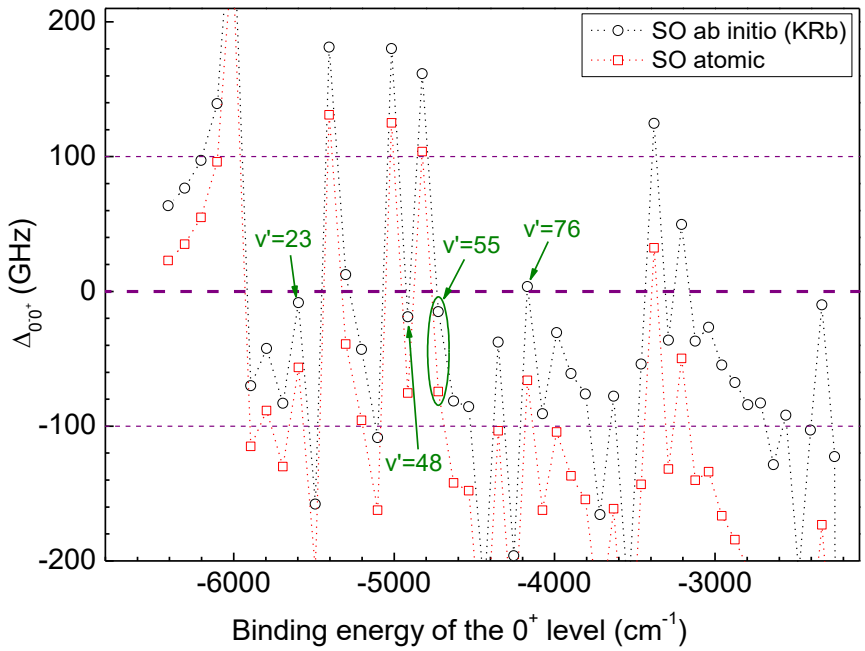

Figure 3.7: Computed values of the spacings $\Delta_{0^-0^+}$ between $v'_{0^+}, J' = 1$ levels and adjacent $v'_{0^-}, J' = 0$ levels. The calculations are implemented with the SOC between $b\,^3\Pi$ and $c\,^3\Sigma^+$ taken as an *ab initio* R-dependent one [140] (black circles) and a R-independent (atomic) one (red squares). Several levels with small spacings are pointed out and the $v' = 55$ level is circled.

molecule [148]. For this coupling, the energy spacing between the $0^+, J' = 1$ level and its adjacent $J' = 0, 2$ levels of 0^- is crucial. Here, the $0^-, J' = 1$ level is not considered as it has opposite parity from that of a $0^+, J' = 1$ level. For the $b(0^+)$ vibrational states, their energies are well known thanks to the well described SOC between $A\,^1\Sigma^+$ and $b\,^3\Pi$ potentials. However, it is still unknown for $b(0^-)$ states due to the unclear SOC between $b\,^3\Pi$ and $c\,^3\Sigma^+$ potentials, which perturbs the position of the $b(0^-)$ states in the range of interest. Note that, with the absence of the SOCs, the $b(0^+)$ states and the $b(0^-)$ states are degenerate as they both belong to the $b\,^3\Pi$ potential.

To obtain the spacings $\Delta_{0^-0^+}$ between $v'_{0^+}, J' = 1$ levels and adjacent $v'_{0^-}, J' = 0$ levels, the $c\,^3\Sigma^+$ potential is taken from quantum chemistry calculations [139] and the SOC between $b\,^3\Pi$ and $c\,^3\Sigma^+$ is approximated as the R-dependent *abinitio*

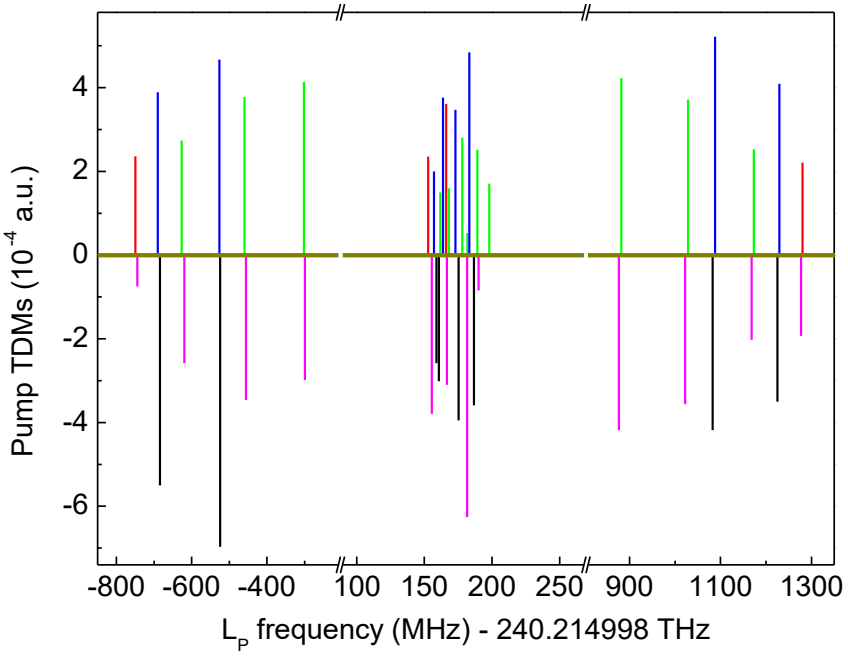

Figure 3.8: Comparison between the experimentally extracted and the theoretically calculated TDMs of the $|v' = 55, J' = 1\rangle$ hyperfine levels. Top panel: computed spectra positions and strengths ($M'_F = 1$ in green, $M'_F = 2$ in blue, $M'_F = 3$ in red). Bottom panel: spectra positions and strengths extracted from experimental data ($\sigma^{\pm}$ transitions in magenta and π transitions in black). The central part with smaller splittings is zoomed in for better view of the details.

data for KRb [140]. For comparison, the calculation is also done with the SOC set to R-independent atomic values. Figure 3.7 illustrates the calculation results with $\Delta_{0^-0^+}$ strongly varying between ± 200 GHz. The $\Delta_{0^-0^+}$ for $v' = 55$ level is about 15 GHz with the R-dependent SOC but can be greatly alerted by a slight change of the SOC parameters. It turns out that several levels could have relatively small $\Delta_{0^-0^+}$, which allows strong $0^+ - 0^-$ mixing to happen.

In order to check whether the $0^+ - 0^-$ coupling could reproduce the observed HFS in Fig. 3.6, the effective Hamiltonian (Eq. 3.1) is extended to include both

the 0^+ and 0^- components:

$$H^{\text{eff}} = \delta_{\epsilon\epsilon'}E_\epsilon + \omega_{\text{Na}}I_{\text{Na}}H^{(1)}_{\text{hfs}}(\text{Na}) + \omega_{\text{Rb}}I_{\text{Rb}}H^{(1)}_{\text{hfs}}(\text{Rb}) + \frac{1}{2}eqQ_{\text{Na}}H^{(2)}_{\text{hfs}}(\text{Na}) + \frac{1}{2}eqQ_{\text{Rb}}H^{(2)}_{\text{hfs}}(\text{Rb}) + w_z g_S \mu_B \mathbf{S}\cdot\mathbf{B} + w_z g_L \mu_B \mathbf{L}\cdot\mathbf{B} + \frac{\mathbf{N}^2}{2\mu R^2}. \tag{3.2}$$

Here, ϵ is used to label the 0^+ and the 0^- level and w_z is to account the singlet-triplet fraction. For the hyperfine interaction terms, the second-order interactions $H^{(2)}_{\text{hfs}}$ are also included with $(eqQ_i)/2$ the nuclear electric quadrupole moment interaction strength.

As the strengths of $H^{(2)}_{\text{hfs}}$ terms only have effects of several megahertz, they have litter influence on the two lateral bands with large splittings and mainly affect the central ones. Thus, we first set the $H^{(2)}_{\text{hfs}}$ terms to zero and adjust the other parameters to match the positions of the levels in the two lateral bands. This yields $w_{\text{Na}} = 245.291$ MHz, $w_{\text{Rb}} = 520.75$ MHz, $\Delta_{0^-0^+} = 181.228$ MHz, $w_z = 0.95$, $B_v^{0^-} = 1960.6$ MHz. The fitted w_z is exactly the value in Table 3.1. To fit the central lines, all the obtained parameters are fixed while the second-order hyperfine interactions are tuned, resulting in $(eqQ_{\text{Na}})/2 = -11.44$ MHz and $(eqQ_{\text{Rb}})/2 = 6.96$ MHz. Comparison between the fitting results and the experimental data are illustrated in Fig. 3.6 and Fig. 3.8. The predicted lines lie exactly at the positions of the experimental ones for the two lateral bands but the agreement is less impressive for the central levels. This is probably the consequence of the several ignored small competing interactions, which could induce contributions of several megahertz. Besides the well reproduced level positions, the transition strengths of these lines, which are not included in the fitting process, already reach fantastic consistence with the experimentally extracted values. These amazing reconstructions validate the mechanism of the anomalously large hyperfine splitting and high quality of the model. For more information on the calculated features of the $|v' = 55, J' = 1\rangle$ levels, such as the fractions of the 0^+ and 0^- components, please refer to our publication Ref. [132].

3.3.3 Calibration of the transition strengths

To calibrate the transition strengths between the Feshbach state and the excited levels, both the loss lineshape and the time evolution of the FMs are measured, as shown in Fig. 3.9 with the excited level of the marked one in Fig. 3.6. In the limit of the pump Rabi frequency Ω_P much smaller than the excited state decay rate $\Gamma = 1/\tau$, τ the excited state lifetime, the evolution of the FM number under irradiation time t follows [145]

$$N(t) = N_0 \exp(-t\Omega_P^2 \frac{\Gamma}{\Gamma^2 + 4\Delta_P^2}). \tag{3.3}$$

Here, N_0 is the initial FM number and Δ_P the pump detuning. However, the condition is not always fulfilled. To be more general, we numerical solve the differential equation of the two-level system

$$c''(t) + (\frac{\Gamma}{2} - I\Delta_P)c'(t) + \frac{\Omega_P^2}{4}c(t) = 0, \tag{3.4}$$

with initial condition $c(0) = 1$ and $c'(0) = 0$. The FM number follows $N(t) = N_0|c(t)|^2$. For both equations, the laser linewidth is ignored, which is reasonable in our system as the laser linewidth (≤ 5 kHz) is much smaller than the natural linewidths of the excited states.

Fitting the loss lineshape and time evolution simultaneously with the numerical solution of Eq. 3.4, we extract $\Omega = 2\pi \times 0.099$ MHz and $\Gamma = 2\pi \times 0.67$ MHz, i.e. $\tau = 238$ ns, for Fig. 3.9. Together with the beam radius of 45 μm, we get the normalized Rabi frequency $\overline{\Omega}_P = 2\pi \times 1.01$ kHz$\times\sqrt{\mathrm{I}/(\mathrm{mW/cm^2})}$, corresponding to a TDM of 7.4×10^{-4} a.u.. Assuming the same lifetime for the hyperfine levels of a certain rovibrational state, we can extract the TDMs of the other hyperfine levels solely from the loss lineshapes once the lifetime is obtained. Thus, the time decay is only measured with several hyperfine levels to get the lifetime, which is fixed as a constant in the fitting of other levels. The extracted TDMs of the $v' = 60, 55$ hyperfine levels are demonstrated in Fig. 3.4 and Fig. 3.8 and compared with the theoretical values. As shown in Fig. 3.8, the hyperfine level

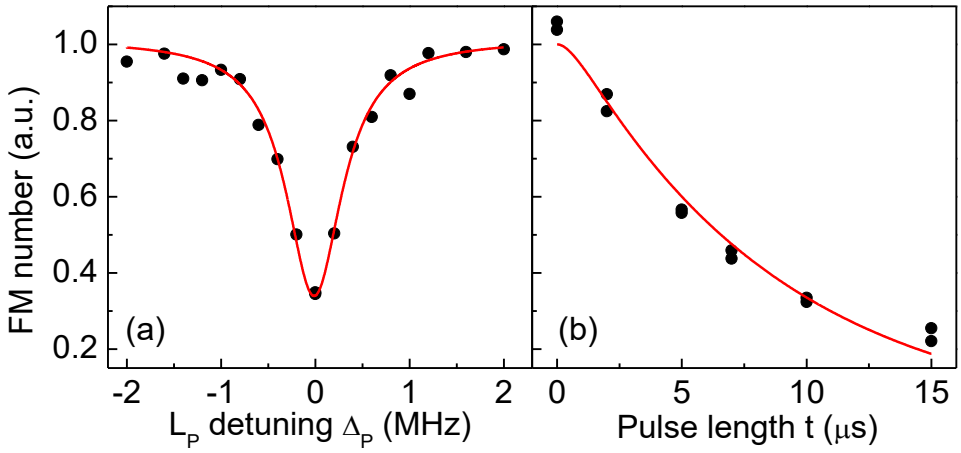

Figure 3.9: Pump transition strength calibration from the Feshbach state to the marked hyperfine level of $|v' = 55, J' = 1\rangle$ state in Fig. 3.6. (a) transition lineshape by tuning pump laser frequency with pulse length of 10 μs. (b) time evolution of the FM number with L_P on resonance. The red curves are simultaneous fittings to the two sets of data. The beam power for both graphs are the same of 0.456 mW with a beam size of 45 μm.

selected for STIRAP has the largest TDM among the HFS. With such a coupling strength, it is easy to achieve an $2\pi \times 1$ MHz Rabi frequency with available laser power. Actually, with the hyperfine level as the intermediate state, we successfully transfer the molecules to a single hyperfine level of the singlet rovibrational ground state with efficiency up to 93%.

As shown in Fig. 3.4 and Fig. 3.8, the measured TDMs have reached remarkable agreement with the predictions of the theoretical model. However, on the other hand, it turns out that the extracted lifetimes, 404 ns for $v' = 60$ state and 238 ns for $v' = 55$ state, are much smaller than the calculated ones, 4372 ns and 535 ns respectively. This deviation could be attributed to the fast predissociation of the $b\,^3\Pi$ states to the $a\,^3\Sigma^+$ continuum due to rotational coupling at short internuclear distances [150], which is not included in our theoretical model. If we replace the triplet-triplet transitional Einstein coefficient, which is about 2.1×10^5 s^{-1}, by a predissociation rate of 2.5×10^6 s^{-1}, the theoretical lifetimes become 405 ns and 242 ns, which are consistent with the experimental values.

Anyway, this predissociation mechanism still needs further experiments to check.

Regarding the lifetimes of the $|v' = 55, J' = 1\rangle$ hyperfine levels, as they have different 0^+ and 0^- component fractions calculated by the theoretical model, the predicted lifetimes for these levels are different. The lifetimes are quite similar within each band while different between these bands. With the assumed predissociation taken into account, it gives the lifetimes of about 240 ns for the left band, 190 ns for the central band and 270 ns for the right band. Thus, the extracted TDMs shown in Fig 3.8 are not accurate as we assume the same lifetime 238 ns for all these hyperfine levels. However, our calculation estimates the shifts of the TDMs due to this lifetime issue are less than 10%.

3.4 Ground state spectroscopy

To precisely locate the singlet rovibrational ground state, two-photon spectrum was carried out. Although the first signal of the ground state was observed utilizing the $|v' = 59, J' = 1\rangle$ level as the intermediate state, all the two-photon spectroscopy demonstrated here are through the marked hyperfine level of the $|v' = 55, J' = 1\rangle$ state in Fig. 3.6. Due to its 5% of the $A\,^1\Sigma^+$ component and the favorable FCF, the $|v' = 55, J' = 1\rangle$ level can also strongly couple to the singlet rovibrational ground state. Figure 3.10 illustrates the two-photon spectrum obtained by scanning the frequency of dump laser L_D while keeping pump laser L_P on resonance. When L_D is tuned near the resonance between the intermediate state and a level of the $A\,^1\Sigma^+$ potential, the excited state will be shifted due to the AC stark effect. With strong L_D, the shift is so large that L_P becomes off resonance and recovery of the FMs should be observed. Thus, the ground states manifest themselves as peaks of the FM number in the two-photon spectrum, as shown in Fig. 3.10 the signals of the rotational ground state $J'' = 0$ and the second excited rotational state $J'' = 2$ of the vibrational ground state $v'' = 0$. From the spacing between the two peaks, corresponding to $6B_v$, the rotational constant

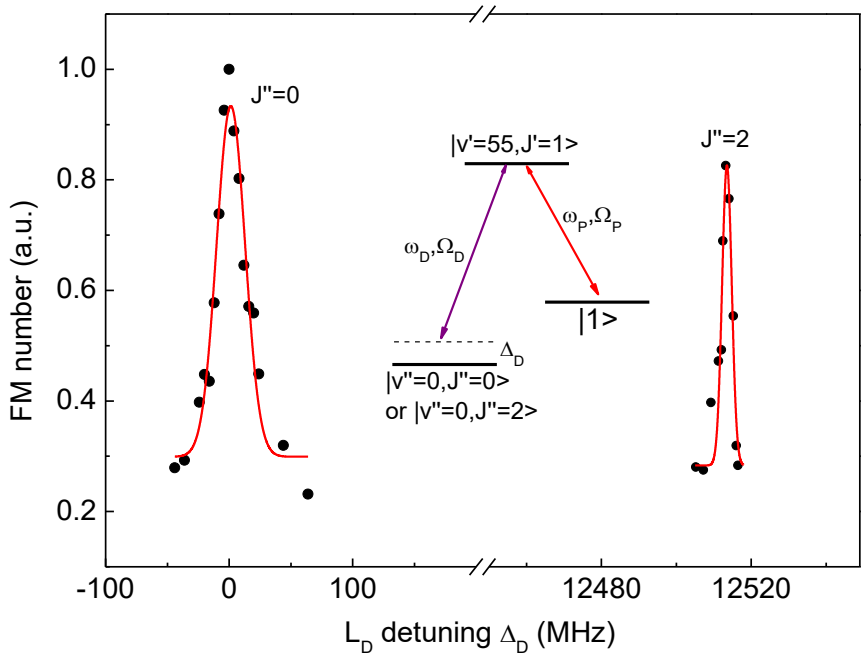

Figure 3.10: Two-photon spectroscopy to locate the singlet ground state through the $|v' = 55, J' = 1\rangle$ state with large dump Rabi frequency. The spectrum is obtained with L_P kept on resonance while the frequency of L_D scanned, as illustrated by the inset. Two rotational levels $J'' = 0, 2$ of the singlet vibrational ground state $v'' = 0$ are identified. Red curves are Gaussian fits to the experimental data.

B_v is extracted to be 0.0697 cm^{-1}, consistent with the theoretical value [151]. From the frequency difference of L_P and L_D, the binding energy of the ^{23}Na^{87}Rb rovibrational ground-state molecule with respect to the hyperfine center-of-mass of each constitute atoms at zero B-field is $D_0^X = 4977.308(3)$ cm^{-1}, which should be the most precise one ever achieved.

As Fig. 3.10 are measured with strong L_D, the HFSs of the rovibrational states are not resolved due to the power broadening effect. For the rotational ground state $J'' = 0$, there are $(2I_{\rm Na}+1)(2I_{\rm Rb}+1)$=16 hyperfine levels. Figure 3.11 illustrates the two-photon spectrum of the $|v'' = 0, J'' = 0\rangle$ HFS, which is obtained with low L_D power and both lasers locked to the ULE cavity. Due to the selection rules of the angular momentum, only 6 out of the total 16 hyperfine levels are observed with the combinations of the laser polarizations. Under a B-field

of 335.6 G, the dominant contribution to the hyperfine splitting of the singlet rovibrational ground state comes from the Zeeman effect of the nuclear spins. Thus, as shown in up panel of Fig. 3.11, the hyperfine energy monotonously depends on the projection of the total angular momentum M_F'', for $J'' = 0$ levels $M_F'' = m_I^{\mathrm{Na}} + m_I^{\mathrm{Rb}}$. The $M_F'' = 3$ hyperfine level with the lowest hyperfine energy is also the level with lowest total energy among all ^{23}Na^{87}Rb molecular states. Thus, it is also the absolute ground state of ^{23}Na^{87}Rb molecule. As shown in Fig. 3.11, with available polarization combinations the absolute ground state can be accessed directly, which means that we can prepare the molecules to the absolute ground state through a single STIRAP.

In order to calibrate the coupling strengths between the intermediate level and the rovibrational ground state, two-photon dark-state spectroscopy is performed with both lasers locked to the ULE cavity, narrowing their linewidths down to below 5 kHz. As illustrated in the inset of Fig. 3.12, L_D is kept on resonance between the intermediate level and the absolute ground state while the frequency of L_P is scanned. When two-photon resonance is achieved, a small recovery window of FMs emerges due to quantum interference even with rather small dump Rabi frequencies, as shown in Fig. 3.12. The most significant feature of the dark-state spectrum is that the spacing between the two dips (Fig. 3.12) directly represents the Rabi frequency of the dump transition [153]. From the spectrum and the beam profile, the TDM of the transition between the intermediate level and the absolute ground level is extracted to be 0.021 a.u. by fitting the data with Eq. 1.13. The transition strength is much larger than that of the pump transitions, even though the singlet component of the intermediate level is only 5%. This indicates a large FCF between the intermediate state and the singlet ground state.

To summarize, the $|v' = 55, J' = 1\rangle$ level satisfies all the requirements of the intermediate state for an efficient STIRAP, strongly coupled to both the Feshbach state and the singlet rovibrational ground state and possessing well resolvable

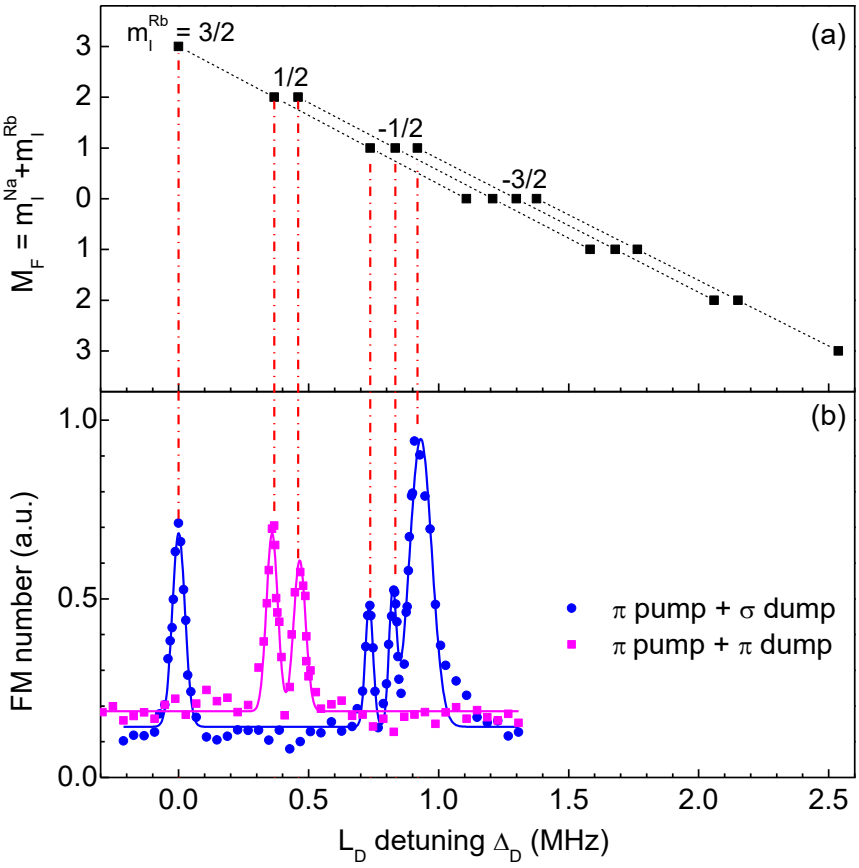

Figure 3.11: Two-photon spectroscopy of the rovibrational ground state obtained similar to Fig. 3.10 but with much smaller dump Rabi frequency and finer scanning step of L_D frequency. Up panel: theoretically predicted positions of the total 16 hyperfine levels, which is modeled with the constants of the hyperfine interactions provided in Ref. [152]. Bottom panel: experimentally resolved hyperfine levels with different polarization combinations. One $M_F'' = +3$, two $M_F'' = +2$ and three $M_F'' = +1$ hyperfine levels are observed with the light polarization combinations, while the $M_F'' = +3$ state with the lowest hyperfine energy is the absolute ground state.

HFS. The high resolution as well as high efficiency STIRAP transfer to the absolute ground state utilizing the $|v' = 55, J' = 1\rangle$ level as the intermediate state will be demonstrated in the next chapter.

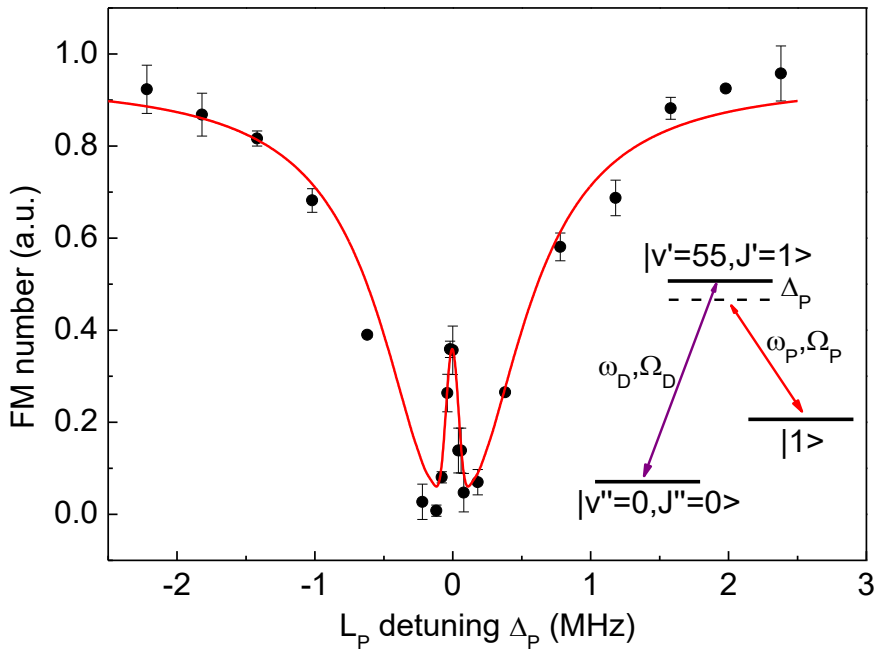

Figure 3.12: Two-photon dark-state spectrum for calibrating the dump transition strength. As shown in the inset, L_D is kept on resonance while the frequency of L_P is scanned. To avoid the influence of nearby ground-state hyperfine levels, the dump Rabi frequency is rather small and non-perfect FM recovery is observed. The pump Rabi frequency is $2\pi \times 0.169$ MHz from above calibration. The red curve is fitting to the data with the three-level master equation Eq. 1.13 with the laser linewidths also taken into account. From the fitting, we get the dump Rabi frequency of $2\pi \times 0.225$ MHz. Together with the beam power and beam profile, we extract the normalize Rabi frequency to be $\overline{\Omega}_D = 2\pi \times 23.2\ \mathrm{kHz} \times \sqrt{\mathrm{I}/(\mathrm{mW/cm^2})}$, corresponding to a TDM of 0.021 a.u..

3.5 The $B\,^1\Pi - c\,^3\Sigma^+$ coupled states

As discussed above, the SOCs in the coupled potentials of $A\,^1\Sigma^+ - b\,^3\Pi$ and $B\,^1\Pi - c\,^3\Sigma^+$ can both induce significant singlet-triplet mixing, which is a prerequisite for the intermediate states. Previously, we have successfully identified a prefect intermediate state with strong $A\,^1\Sigma^+ - b\,^3\Pi$ mixing. The other $B\,^1\Pi - c\,^3\Sigma^+$ coupled scheme is also promising to support suitable excited states, which is applied to create ground-state KRb [69, 99] and NaK molecules [79, 146].

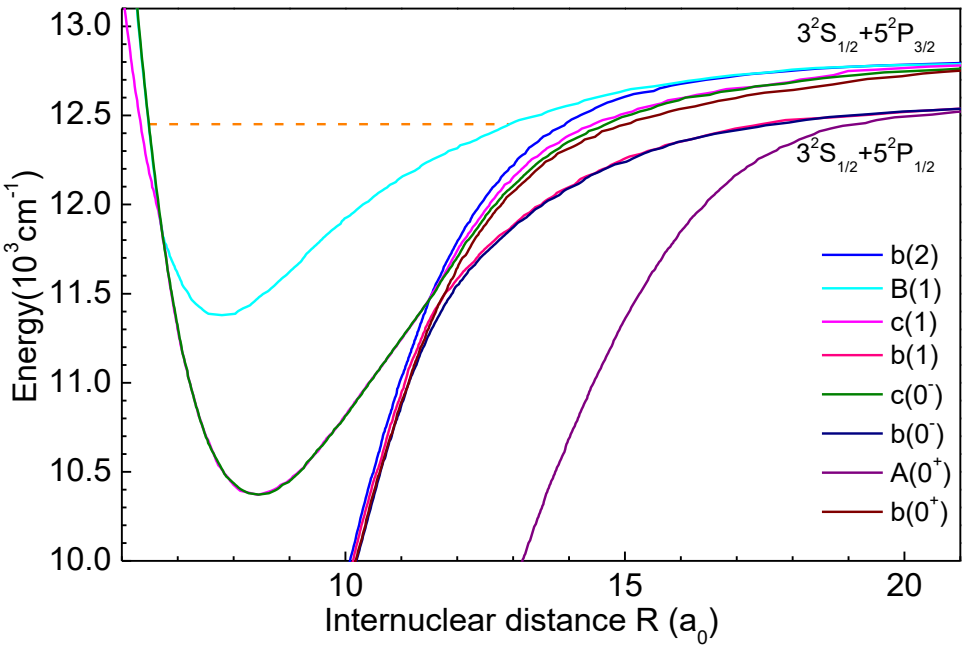

Figure 3.13: The eight excited SOC potentials near the energy region, where the $B\,^1\Pi - c\,^3\Sigma^+$ mixing is strong. The horizontal dashed line indicate the identified intermediates states of the $B\,^1\Pi$ potential.

In this section, I will illustrate several $B\,^1\Pi - c\,^3\Sigma^+$ mixed vibrational states that are identified to be also suitable for efficient STIRAPs.

Due to the lack of experimental data on the $c\,^3\Sigma^+$ potential and the SOC interaction between the $B\,^1\Pi$ and $c\,^3\Sigma^+$ potentials, it is hard to accurately predict the positions and properties of the mixed vibrational states. However, the searching criteria for the mixed states are much simpler and more straightforward than the $A\,^1\Sigma^+ - b\,^3\Pi$ ones. This makes the identification realizable even with the coupled potential unknown. The coupling between the $B\,^1\Pi$ and the $c\,^3\Sigma^+$ potentials are mainly through the SOC potentials with $\Omega = 1$, $B(1)$ for the $B\,^1\Pi$ potential and $c(1)$ for the $c\,^3\Sigma^+$ potential. Due to the non-zero Ω, the hyperfine interactions are typically strong enough to result in resolvable HFSs. Thus, for the $B(1)$ dominated vibrational states, which are mainly singlet, once they can strongly couple to the triplet dominated Feshbach state, they should satisfy all the re-

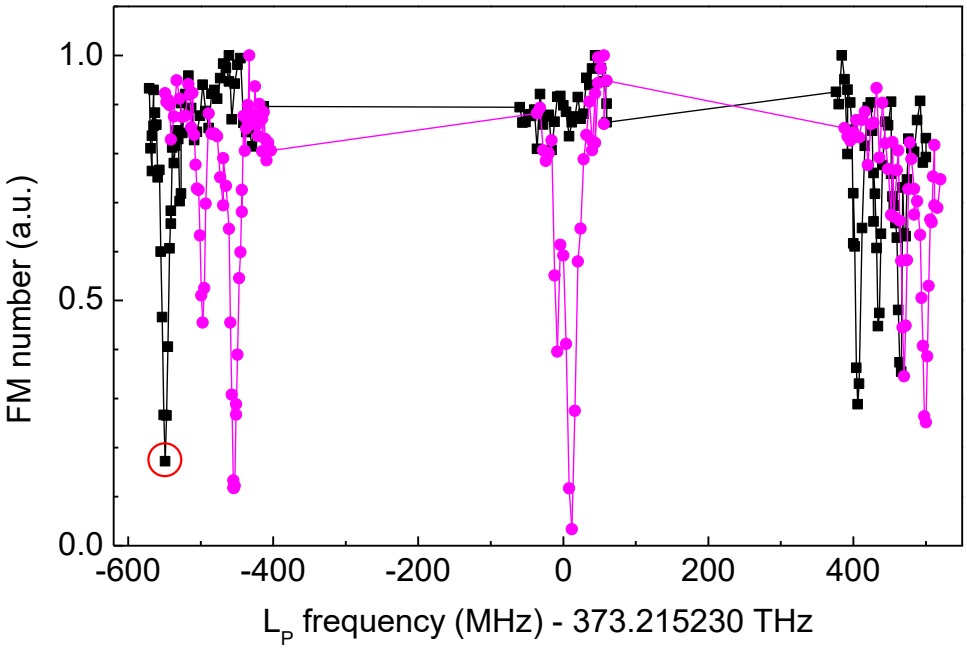

Figure 3.14: HFS of the 12449 cm^{-1} vibrational state of the $B\,^1\Pi$ potential. The marked level (red open circle) is well isolated from the other hyperfine levels and is used as the intermediate state for the two-photon spectrum in Fig. 3.15. The notations are the same as in Fig. 3.4.

quirements for the intermediate states. Thanks to the previous experiment on the $B\,^1\Pi$ potential [138] and our spectroscopy work on long-range states near the excited asymptote [154], the vibrational states of the $B\,^1\Pi$ potential below the dissociation limit without considering its SOC to the $c\,^3\Sigma^+$ potential can be calculated using Level 8.0 [155]. Thus, our idea to search the $B\,^1\Pi - c\,^3\Sigma^+$ mixed states is just implementing the one-photon loss spectroscopy on the FMs near the calculated $B\,^1\Pi$ vibrational states. The observed $B\,^1\Pi$ states already illustrate their strong singlet-triplet mixed character, if they can couple to the triplet dominated Feshbach state. The explored region is about 12000 cm^{-1} above the dissociation limit of two ground-state atoms, as shown in Fig. 3.13, where the $B\,^1\Pi - c\,^3\Sigma^+$ coupling is predicted to be strong.

Actually, several suitable vibrational states are identified, including those with wavenumber of 12548.7 cm^{-1}, 12499.2 cm^{-1} and 12449.1 cm^{-1}. More vibrational

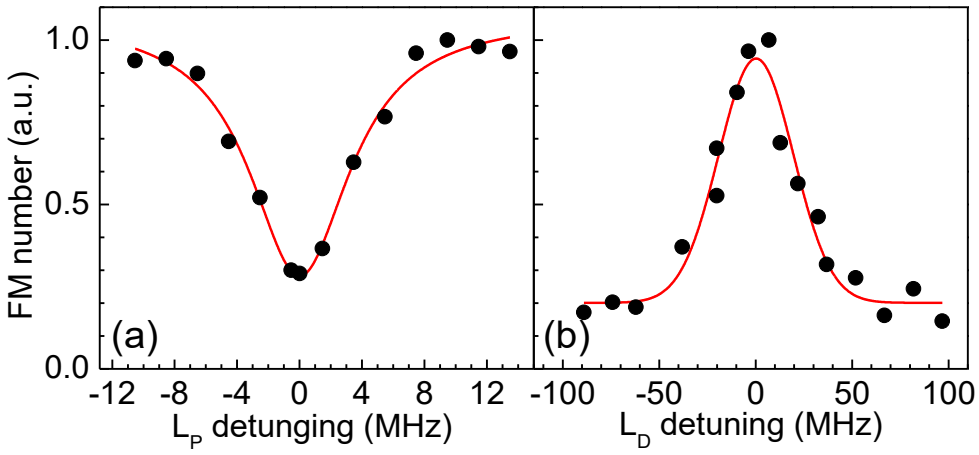

Figure 3.15: (a) One-photon lineshape of the marked hyperfine level of the 12449 cm^{-1} state. (b) Two-photon spectrum coupling to the singlet rovibrational ground state $|v'' = 0, J'' = 0\rangle$. The two-photon spectrum was measured with L_P frequency of 373.2146 THz and 522.4248 THz for L_D.

states can also be identified but not searched in our present experiment. Here, I will take the 12449.1 cm^{-1} one as a typical example. Figure 3.14 shows the HFS of the $J' = 1$ rotational state. The other rotational level $J'' = 2$ is also observed but not shown here. This is consistent with the rotational selection rule for $\Omega = 1$ states as discussed above. The hyperfine levels are almost fully resolved as expected, especially the one marked with red open circle. The marked level is well isolated from the other hyperfine levels that can be accessed with the same light polarization.

Following the same process, we calibration the coupling strength between the marked hyperfine level and the Feshbach state, with the typical loss lineshape demonstrated in Fig. 3.15(a). The TDM is extracted to be 0.0031 a.u. and a lifetime of 26.69 ns. The coupling strength is about ten times stronger than that of the $|v' = 55, J' = 1\rangle$ level, while the lifetime is ten times shorter, similar to the lifetime of Rb atoms in the $5\,^2P_{3/2}$ excited state. The two-photon spectrum to calibrate the dump transition strength is shown in Fig. 3.15(b). The dump beam used here have a frequency of 522.4248 THz (573.8 nm), which is generated

from a dye laser (DYE-SF-077, previously used for cooling ^{23}Na atoms) [156]. As there was no available frequency reference (say ULE cavity) to stabilize the laser and reduce its linewidth, high L_D power was used and HFS of the rovibrational ground state was not observed. With the ground state HFS unresolved, it is hard to accurately calibrate the transition strength to each hyperfine level, while the order of the TDM is extracted to be 0.09 a.u.. Thus, the 12449 cm^{-1} level is also suitable as an intermediate state for efficient STIRAP transfers with peak Rabi frequencies over $2\pi \times 10$ MHz.

In this chapter, high-resolution spectroscopy on the weakly-bound FMs to search suitable intermediate level for STIRAP is demonstrated. Two types of excited states are successfully identified, one with $A\,^1\Sigma^+ - b\,^3\Pi$ mixed character and the other one of $B\,^1\Pi - c\,^3\Sigma^+$ coupling. For the $A\,^1\Sigma^+ - b\,^3\Pi$ coupled excited level, it has relatively long lifetime but the maximum achievable Rabi frequency is limited by the pump transition strength to be about $2\pi \times 2$ MHz. While, for the $B\,^1\Pi - c\,^3\Sigma^+$ mixed state, the lifetime is short but high Rabi frequencies larger than $2\pi \times 10$ MHz can be achieved. In principle, transfer efficiencies up to 90% can both be accomplished though these two types of intermediate levels. However, due to the lack of the suitable ULE cavity for the dump laser of the $B\,^1\Pi - c\,^3\Sigma^+$ coupled scheme, we have not tried the STIRAP through the $B\,^1\Pi - c\,^3\Sigma^+$ mixed states. In the next chapter, I will illustrate the realized high-efficiency STIRAP transfer to a single hyperfine level of the singlet rovibrational ground state through the $|v' = 55, J' = 1\rangle$ $A\,^1\Sigma^+ - b\,^3\Pi$ mixed state.

□ End of chapter.

Chapter 4

Creation of the Ground-state $^{23}Na^{87}Rb$ Molecules

After identifying suitable intermediate states and precisely locating the singlet rovibrational ground state, we performed a STIRAP to transfer the Feshbach molecules to the singlet ground state with high efficiency. By carefully choosing the Rabi frequencies of the two laser beams and the pulse length, high-resolution STIRAP transfers are accomplished with molecules prepared to a single hyperfine level with high purity. The properties of the ground-state molecules, including their lifetime (will be discussed in details in the next chapter), the permanent electric dipole moment and dynamic response (polarizability) to the 1064.4 nm ODT, are then investigated. By combining the two-photon Raman process with extra microwave fields, we have achieved full internal states control over the molecules, including their vibrational, rotational and hyperfine degrees of freedom. The results on the creation and characterization of the absolute ground-state $^{23}Na^{87}Rb$ molecules have been published in Ref. [82], while the accomplishment of the full internal states control is still under preparation [90].

4.1 STIRAP to the absolute ground state

To transfer the FMs to the singlet ground state through a STIRAP, counter-intuitive Raman pulses are implemented, as discussed in Sec. 1.3. In our experiment, the sine-shaped pulses of the Raman beams are controlled by modulating the amplitude of the RF signals that drive the AOMs on the optical paths to the molecular sample. Figure 4.1(b) illustrates the implemented Raman pulses for a round-trip STIRAP between the Feshbach state and the absolute ground state. Time evolution of the FM number during the round-trip STIRAP is shown in Fig. 4.1(a). Within the first STIRAP process, FMs are transferred to the absolute ground state indicated by the decreasing of FM number. Then, the second (reverse) STIRAP populates the molecules back to the Feshbach state, manifested as revival of the FM signal. As demonstrated in Fig. 4.1(a), the dynamical evolution agrees well with our simulation result using the master equation (Eq. 1.13) without any free parameter. Assuming the same efficiency for the two processes, a single-trip STIRAP efficiency of about 80% is extracted (the STIRAP efficiency stands for a single-trip efficiency unless specified hereafter).

The STIRAP process illustrated in Fig. 4.1 was implemented using the old Raman laser system. The largest Rabi frequency of the pump transition is only $2\pi \times 0.7$ MHz limited by the available laser power. On the other hand, the 5 kHz laser linewidths result in short Raman pulse duration of only 15 μs, as indicated by the dashed vertical lines. After upgrading the laser system, STIRAP efficiency up to 93% can be routinely achieved with the narrower laser linewidths of about 1 kHz and higher pump laser power. All the results demonstrated below are accomplished with our new Raman laser system.

As discussed in Sec. 3.4, the singlet rovibrational ground state has certain HFS and the splittings between adjacent levels are only on the order of 100 kHz even at a B-field of 335.2 G. To prepare the molecules in a single quantum state (hyperfine level), the STIRAP linewidth should be smaller than the spacings to

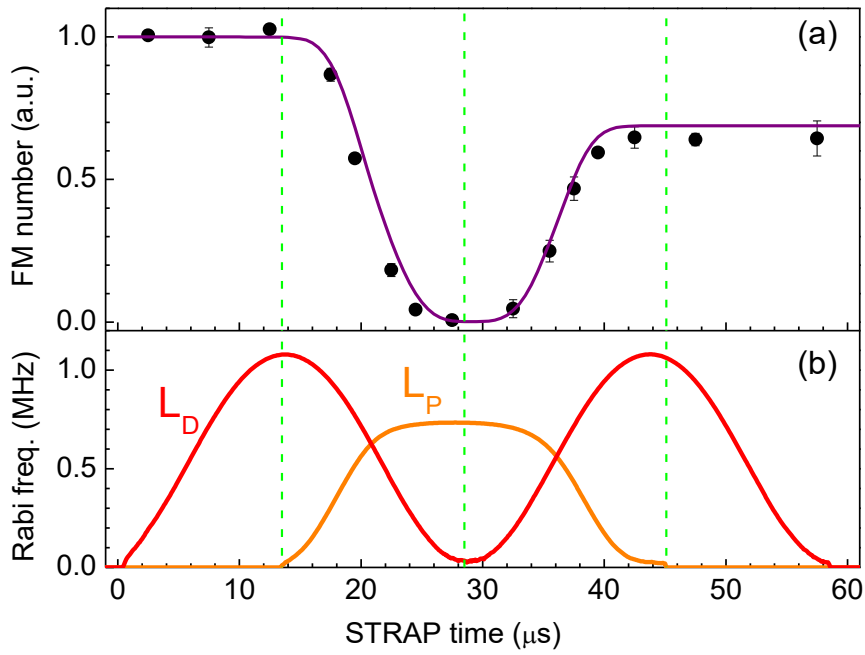

Figure 4.1: (a) Time evolution of the FM number during the transfer process. Here, a round-trip STIRAP is implemented, indicated by the dashed vertical lines the region of the STIRAP and the reverse-STIRAP process. The solid curve is the simulation result using the master equation (Eq. 1.13) with all parameters determined experimentally. (b) The measured pulses of the Raman beams that lead to the round-trip STIRAP. The pulse duration for a single STIRAP is about 15 μs. The peak Rabi frequencies are extracted to be $2\pi \times 0.7$ MHz for the pump transition and $2\pi \times 1.1$ MHz for the dump transition.

nearby levels. Figure 4.2(a) shows the STIRAP spectrum, which is the observed FM signal after a round-trip STIRAP with respect to the two-photon detuning, acquired with 50 μs Raman pulses overlap. As the absolute ground state (the $\delta = 0$ peak in Fig. 4.2) is more than 300 kHz away from the nearest hyperfine level, the molecules can be transferred to the absolute ground state with high purity and high efficiency. However, for the other hyperfine levels with spacings less than 100 kHz, they are strongly mixed and cannot be prepared to a single level with the STIRAP parameters. This problem can be overcome by using longer Raman pulses and lower Rabi frequencies while maintaining the adiabatic

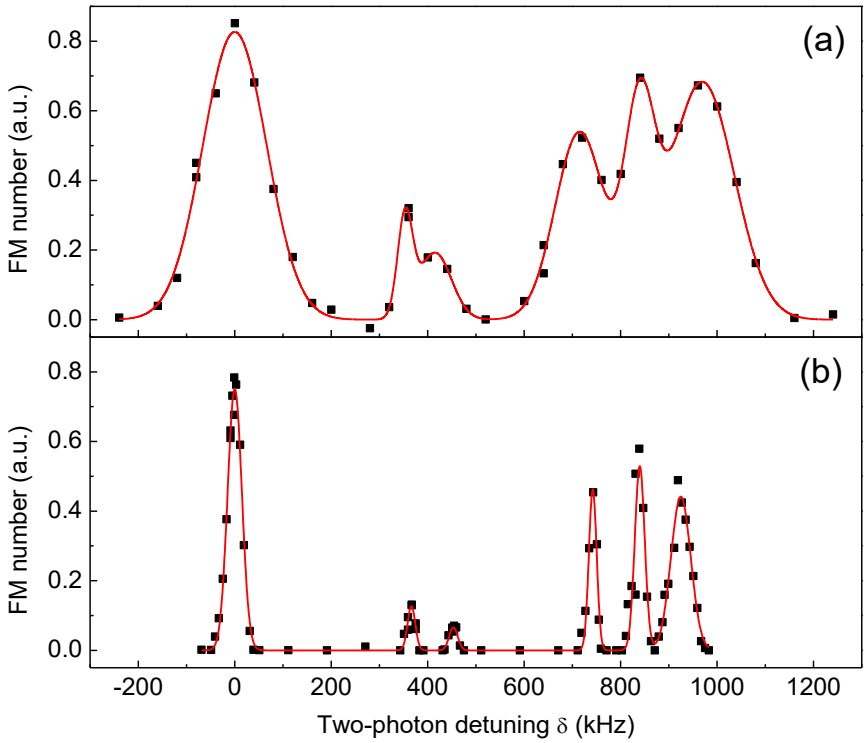

Figure 4.2: STIRAP spectrum (round-trip STIRAP) of the rovibrational ground state. (a) The spectrum obtained with a 50 μs single STIRAP duration and Rabi frequencies of $2\pi \times 1.5$ MHz for both transitions. (b) The spectrum with much narrower two-photon linewidth obtained using a 200 μs single STIRAP duration and laser powers about one fourth of that in (a). For both figures, the dump light has slight π polarization component, which results in small signals of $M_F = 2$ hyperfine levels. The y-axis values correspond to the round-trip efficiencies, i.e. square of the STIRAP efficiencies.

condition (Eq. 1.12) well fulfilled. Typically, lower Rabi frequencies reduce the power broadening effect and longer Raman pulse diminishes the broadening due to the finite pulse length. On the other hand, the length of the Raman pulse is limited by the decoherence effects, which is mainly from the laser frequency noise in our system. With laser linewidths reduced to about 1 kHz, it allows for Raman pulses as long as 400 μs while maintaining STIRAP efficiencies higher than 80%. Figure 4.2(b) shows the STIRAP spectrum with a 200 μs pulse length and $2\pi \times 0.8$ MHz Rabi frequencies. These parameters result in the two-photon

linewidths four times smaller than that in Fig. 4.2(a) and all the hyperfine levels well resolved. Thus, molecular samples of any desired hyperfine levels without occupying nearby states can be accomplished. Meanwhile, the transfer efficiency is still impressive especially the one of the absolute ground state. The efficiencies of other hyperfine levels are a bit smaller but can also reach 80% by optimizing the parameters individually for a certain level.

4.2 Properties of the ground-state molecules

After the ground-state molecules were created, we performed experiments to characterize their properties, including their lifetime (or more precise the loss rate), the permanent electric dipole moments and their response to the 1064 nm ODT. The investigations on the molecular loss rates will be discussed in details in the next chapter.

4.2.1 The permanent electric dipole moment

One distinction of the heteronuclear molecules from the atomic species is their possession of the permanent electric dipole moments in their rovibrational ground states. However, without the presence of external E-fields, the effective dipole moments are zero as they orient randomly in the lab frame. To characterize the dipolar nature of the ground-state ^{23}Na^{87}Rb molecules, we imposed a static E-field along the vertical direction, parallel to the quantization axis provided by the B-field, and measured the DC Stark shift of the ground state through the two-photon spectrum. Figure 4.3 illustrates the shifts of the one-photon (a) and two-photon (b) spectrum under different E-fields. As the FMs have nearly zero electric dipole moments, the E-fields barely change the energy of the Feshbach state. Thus, the shifts of the one-photon resonance are exactly the DC Stark shifts of the excited state. While, the shifts of the frequency differences between L_P and L_D, when two-photon resonance is fulfilled, solely result from the changes of the

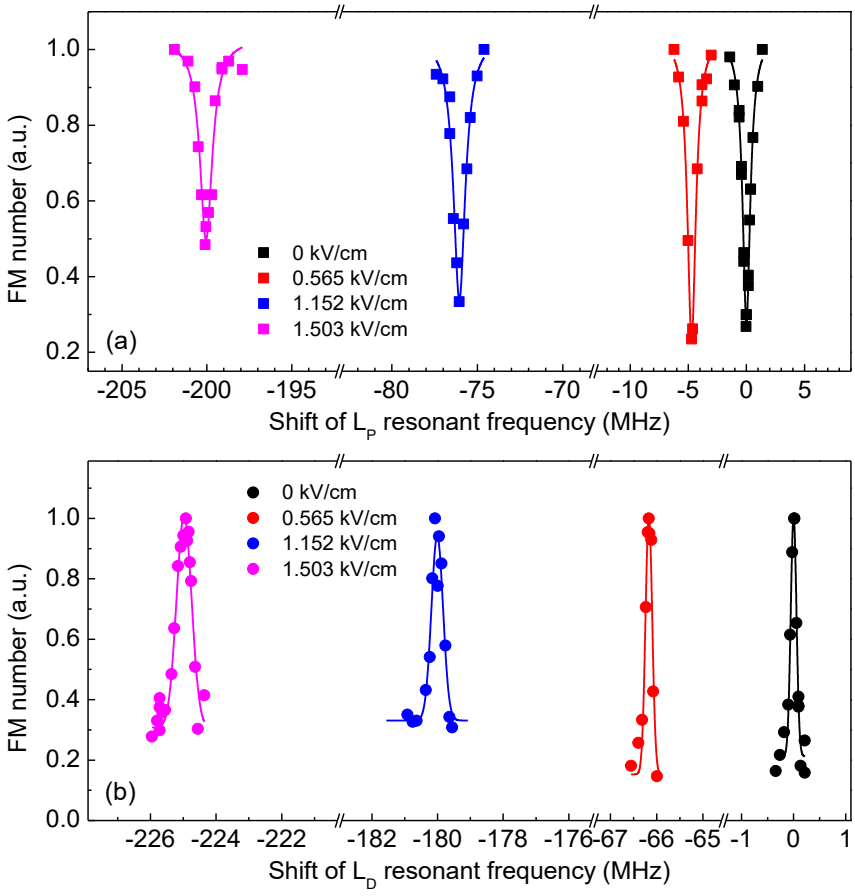

Figure 4.3: (a) One-photon spectrum at four external E-fields, from which the DC Stark shift of the intermediate state is extracted. (b) Two-photon spectrum with respect to the shift of L_D frequency with L_P on resonance, i.e. the x axis is the Stark shift of the ground state relative to the excited state.

ground state. The extracted DC Stark shifts of the intermediate state and the absolute ground state as a function of the applied E-fields are shown in Fig. 4.4.

In order to interpret the DC Stark shifts and obtain the permanent electric dipole moments of the absolute ground state, the single molecule Hamiltonian under an E-field is written [35, 157, 158, 159]

$$\hat{H} = \hat{H}_{rot} + \hat{\mathbf{d}} \cdot \hat{\mathbf{E}}. \tag{4.1}$$

Here, $\hat{H}_{rot}$ is the rotational energy and the second term represents the interaction between the electric dipole moment $\hat{d}$ and the E-field $\hat{\mathbf{E}}$. With the presence of an

E-field, rotational levels with different parity are coupled, inducing an effective dipole moment. In this model, the hyperfine structure of each rotational state is ignored due to the small hyperfine splittings relative to the rotational spacings. For an E-field parallel to the quantization axis, it only couples rotational levels with the same quantum number M_J, which is the projection of J to the quantization axis. In this case, the matrix elements of the Hamiltonian follows [159, 160]

$$\begin{aligned} &\langle J, M_J | \hat{H} | J', M'_J \rangle \\ &= B_v J(J+1)\delta_{JJ',M_J M'_J} \\ &- d_0 E_0 \sqrt{(2J+1)(2J'+1)}(-1)^{M_J} \begin{pmatrix} J & 1 & J' \\ -M_J & 0 & M'_J \end{pmatrix} \begin{pmatrix} J & 1 & J' \\ 0 & 0 & 0 \end{pmatrix}, \end{aligned} \tag{4.2}$$

where, B_v is the rotational constant, $\delta_{JJ',M_J M'_J}$ is the Kronecker symbol, d_0 is the permanent electric dipole moment and E_0 represents the strength of the E-field. As shown by the 3j-symbols, the diagonal terms of the interaction are nonzero only for rotational excited states. The off-diagonal terms depict the couplings between nearby rotational levels of different parity induced by the E-field. In principle, the E-field couples all the rotational levels and the Hamiltonian has infinite elements. However, for higher rotational levels, the splittings between adjacent levels are much larger and their effects on the lower lying levels become smaller. In our calculation, rotational levels with $J \leq 10$ are taken into account and higher ones have negligible effects within our accessible E-fields. By diagonalizing the Hamiltonian, the DC Starks shifts of each rotational level can be obtained.

Using the model to fit the experimental data and setting $B_v = 0.0697$ cm^{-1}, extracted from the two-photon spectrum (Fig. 3.10), the permanent electric dipole moment is determined to be 3.2(1) D [82] for the absolute ground state. The value is consistent with the theoretical predicted ones [95, 161, 162, 163]. On the other hand, for the intermediate state, no simple model is feasible to interpret the DC Stark shifts due to its complexity. As shown in Fig. 4.4, the shift of the intermediate state is flatter at low E-fields while steeper at high E-fields than

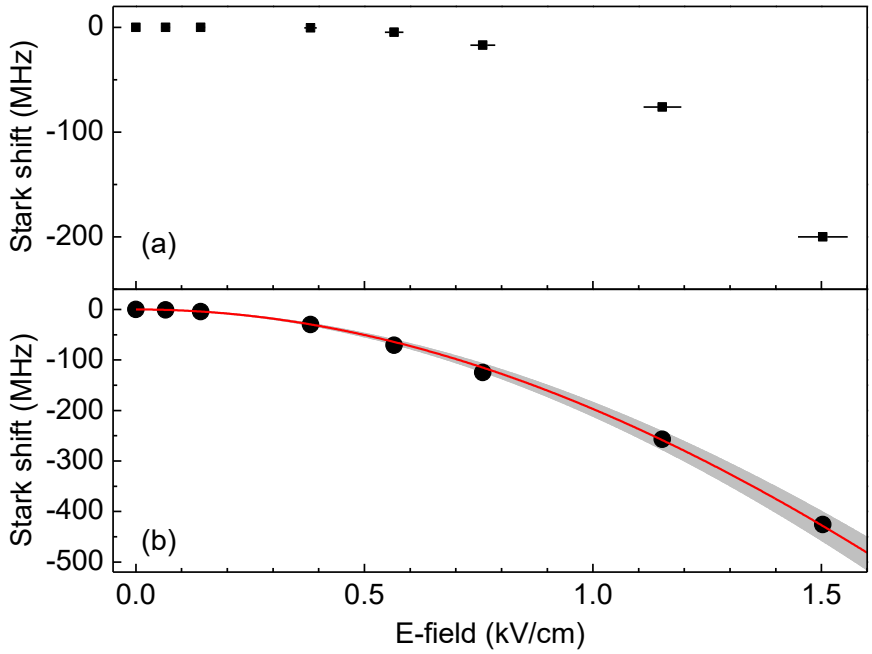

Figure 4.4: DC stark shifts of the intermediate state (a) and the absolute ground state (b). The E-field strengths are obtained from the simulation (Sec. 2.5) and the error bars are mainly from the uncertainties of the positions of the electrodes and nearby conductors. The red curve in (b) is the fitting result, from which the permanent electric dipole moment is extracted to be 3.2(1) D.

that of the ground state, which validate its distinct behaviors.

For the ground-state molecule at an E-field, the effective dipole moment of the molecule is defined as

$$d_{eff} \equiv -\frac{d\Delta E_{Stark}}{dE_0}, \tag{4.3}$$

with ΔE_{Stark} the DC Stark shift. In this case, the molecule can be regarded as a particle with an electric dipole moment of d_{eff}. Typically, the d_{eff} strongly depends on the applied E-field. Figure 4.5 plots the effective dipole moments of the first two rotational levels $J = 0, 1$ as a function of the applied E-field. At low fields, the effective dipole moments almost linearly depend on the external E-field while reach a saturated value at high E-fields.

The dependence of effective dipole moment of the $|J = 1, M_J = 0\rangle$ level on the E-field, which first decreases with the increasing E-fields while changes sign

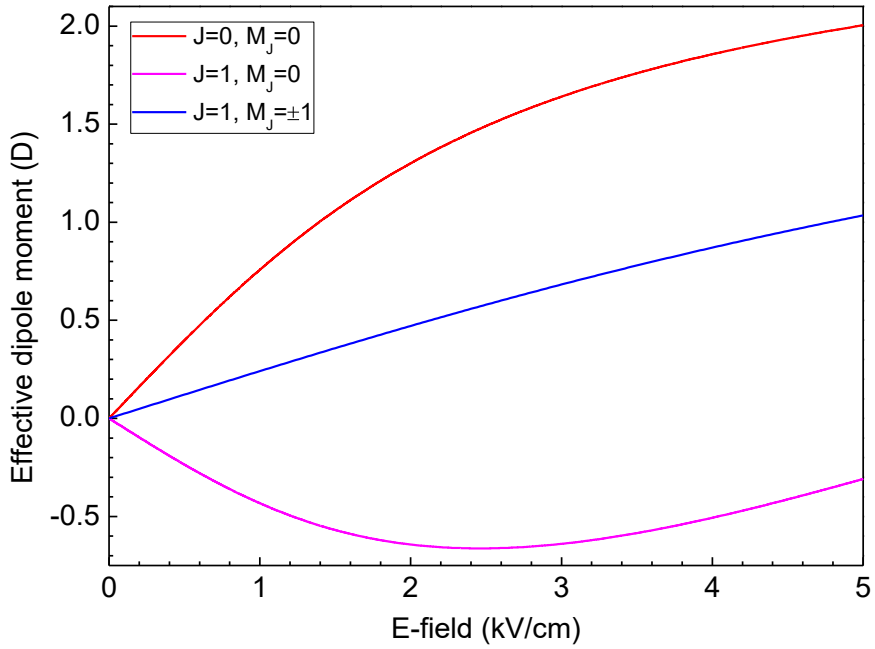

Figure 4.5: The effective dipole moments of the first two rotational states under different E-fields. For our largest E-field of 1.5 kV/cm, the effective dipole moment of the rovibrational ground state can already reach to 1.06 D [82], the largest one ever achieved in ultracold molecules.

of the slope at about 2.5 kV/cm, is of great interest. The behavior indicates that the coupling to $J = 2$ level starts to dominate over the effect of coupling to $J = 0$ state at 2.5 kV/cm E-field. Furthermore, another important feature of the $|J = 1, M_J = 0\rangle$ level is its negative sign of the effective dipole moment (at least within the scope of Fig. 4.5), which means that the molecules in $|J = 1, M_J = 0\rangle$ state are low E-field seeking, distinct from the other two levels shown in Fig. 4.5. Thus, the molecules can be trapped by a static electric gradient field [164, 165, 166], similar to a magnetic quadrupole trap for atomic species. The electric gradient trap is perfectly harmonic, as the trap potential is purely quadratic, with an almost infinite trap volume compared to the sample size. Moreover, it can totally remove the effects of the lights on the samples, which is unavoidable for an optical dipole trap.

4.2.2 The polarizability

Before any further investigations on the ground-state molecules, the dynamic response of the molecules to the 1064.4 nm optical dipole trap, i.e. the molecular polarizability, needs to be determined. Only with the polarizability known can we establish the density distribution of the molecules in the trap, which is essential in measuring the molecular loss coefficients (discussed in details in the next chapter).

Theoretically, the polarizability can be calculated by accounting all the possible electric dipole transitions from the singlet vibrational ground state to the excited states, i.e. including the entire energy spectrum. Following this method, Ref. [167] has calculated the polarizability of the ground-state molecule with respect to the light wavelength, as shown in Fig. 4.6. For comparison, the sum of the atomic polarizability of ^{23}Na and ^{87}Rb atoms, which is approximately the value for the weakly-bound FMs, is also demonstrated. At the wavelength of our trap beams, the polarizability of the singlet rovibration ground state is about 674 a.u. and 909 a.u. for the Feshbach state.

To experimentally measure the polarizability of the ground-state molecule, we monitor the dipole-oscillation mode of the molecules in the optical dipole trap. Figure 4.7 illustrates the center-of-mass motions of the ground-state molecules and the FMs along the vertical direction and the horizontal (weakly-confined) direction after artificial excitations. The trap frequencies are extracted to be $2\pi \times \{26.6(4), 128.9(1.4)\}$ Hz for the absolute ground-state molecule and $2\pi \times \{32.0(3), 161.3(5)\}$ Hz for the FM, which are consistent with the theoretically predicted values of $2\pi \times \{27.0, 129.4\}$ Hz and $2\pi \times \{31.5, 160.2\}$ Hz respectively. Thus, the theoretical polarizabilities should be accurate and reliable.

At 1064.4 nm, the polarizability for ground-state molecule is about one third smaller than that for the FM. What's more, within the entire off-resonance region as shown in Fig. 4.6, there do not exist a wavelength at which the polarizabilities of them are the same [167]. Due to their different polarizabilities, the ground-

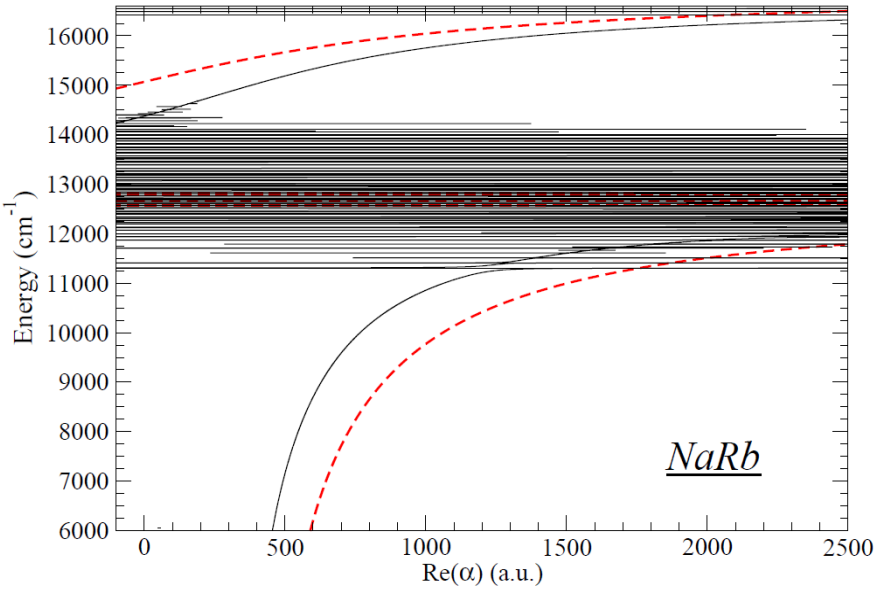

Figure 4.6: Real part of the theoretical polarizability of a singlet vibrational ground-state molecule (black solid curve) and the sum of the atomic polarizabilities of ^{23}Na and ^{87}Rb atoms (red dashed curve). Reproduced from Ref. [167].

state molecules and the FMs see different trap potentials, which can induce dephasing effect in the STIRAP process [168, 169, 170]. Another problem induced by the different polarizabilities is the undesired breathing motion after the STIRAP transfer [82]. As the spatial distribution of equilibrium for the ground-state molecules is different from that for the FMs and the STIRAP process (~ 100 μs) is much faster compared to the trap frequencies (> 5 ms), the obtained ground-state molecules are out of equilibrium starting from an equilibrated sample of FMs. To compensate the polarizability difference, we increase the power of the trap beams by about one third in 100 μs immediately after the transfer. In this way, the undesired breathing motion is greatly suppressed. The ideal method to deal with the problem is to tune the trap power synchronously during the STIRAP process, i.e. controlling the lights power according to the polarizability of the dark state. However, this technique has not been achieved at present.

For rotational ground states as discussed above, a single polarizability parameter is enough to describe the dynamic response of the molecules to the lights.

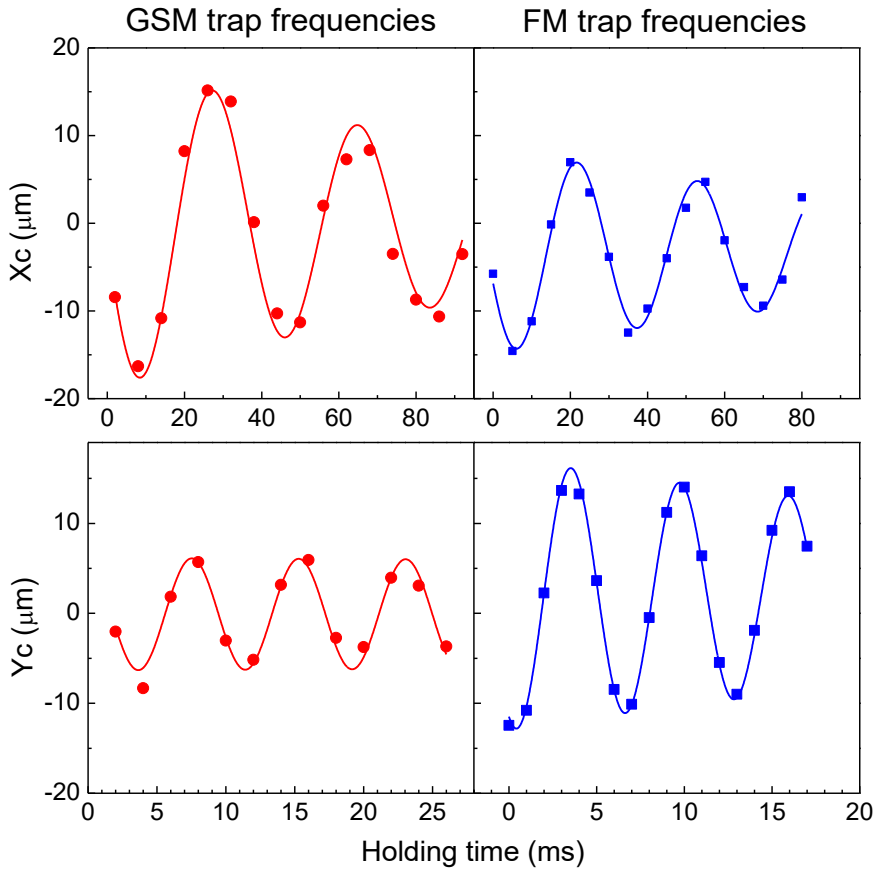

Figure 4.7: Center-of-mass motion of the Feshbach molecules and the absolute ground-state molecules along the horizontally weakly-confined direction (Xc) and the vertical direction (Yc) in the optical dipole trap. The trap frequencies are extracted to be $2\pi \times \{26.6(4), 128.9(1.4)\}$ Hz for the ground-state molecule and $2\pi \times \{32.0(3), 161.3(5)\}$ Hz for the FM respectively.

As a consequence of the isotropic wavefunction of the rotational ground states, the polarizability, which is called the isotropic polarizability, is independent from the light polarization. However, for rotational excited states with anisotropic wavefunctions, an extra parameter called the anisotropic polarizability should be introduced to fully describe their dynamic response. These two parameters follow [167, 171, 172]

$$\tilde{\alpha}(\omega) = \frac{1}{3}\alpha_{\parallel}(\omega) + \frac{2}{3}\alpha_{\perp}(\omega), \tag{4.4}$$

$$\gamma(\omega) = \alpha_{\parallel}(\omega) - \alpha_{\perp}(\omega). \tag{4.5}$$

Here, $\tilde{\alpha}$ and γ are the isotropic and anisotropic polarizability. $\alpha_{\parallel}$ and $\alpha_{\perp}$ are the polarizability contributions from parallel and perpendicular (with respect to the internuclear axis) transitions. Thus, the effective polarizability with respect to a polarized light with an angle θ to the quantization axis is [173]

$$\begin{aligned} \alpha(\theta) &= \alpha_{\parallel}\cos^2(\theta) + \alpha_{\perp}\sin^2(\theta) \\ &= \tilde{\alpha} + \gamma P(cos\theta), \end{aligned} \tag{4.6}$$

which depends on the light polarization. The anisotropic response to the ODT lights has already been observed in the first excited rotational state of the KRb molecule [170] and the RbCs molecule [173]. Magic angles, at which the rotational excited state has the same polarizability as the ground state, are also determined for the KRb molecule [170].

4.3 Full internal state control

In the last section, I demonstrated our capability to induce large effective dipole moments within the ultracold ^{23}Na^{87}Rb molecules. Besides the potential for realizing the strong DDI, another distinct property of the molecules from atomic species is their rich internal states, including electronic, vibrational, rotational and hyperfine degrees of freedom. On one hand, the rich internal degrees of freedom make ultracold molecules prospective platform to investigate ultracold chemistry [74, 75, 174] and to realize quantum information processing [37]. On the other hand, all the proposed applications require well controlled molecular states. Using microwave transitions to control the rotational and hyperfine degrees of freedom has been successfully demonstrated in the ultracold molecules of ^{40}K^{87}Rb [87], ^{87}Rb^{133}Cs [88] and ^{23}Na^{40}K [89]. Moreover, long coherence time up to 1 s was observed between two hyperfine levels of ^{23}Na^{40}K molecules [73]. In this section, I will illustrate the achieved full internal states control over the obtained ^{23}Na^{87}Rb molecules by combining the STIRAP process with extra microwave pulses [90]. Enabled by this, we have studied the molecular losses with

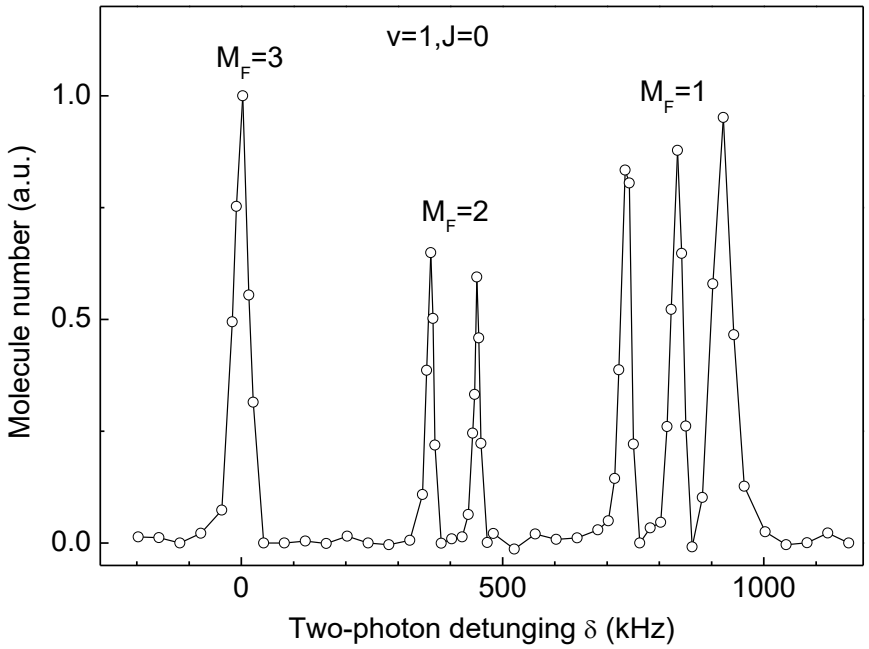

Figure 4.8: STIRAP spectrum of the first excited vibrational state $|v = 1, J = 0\rangle$ obtained with 200 μs STIRAP processes and Rabi frequencies less than $2\pi \times$ 0.8 MHz. The transfer efficiency to $M_F = 3$ level corresponds to about 88%. The zero two-photon detuning ($\delta = 0$) corresponds to a binding energy of 146.03718(6) THz. The spectrum is obtained with external trap potential, i.e. ODT, turned off.

and without the presence of the chemical reaction [175].

In Sec. 4.2, STIRAP transfer from the Feshbach state to the singlet rovibrational ground state has been illustrated. Thanks to the favorable Franck-Condon overlap between the intermediate level and the vibrational states near the bottom of the $X\,^1\Sigma^+$ potential, direct transfer to the first excited vibrational state $v = 1$, lying 105.8 cm^{-1} above the ground state, can be achieved by simply tuning the frequency of the dump laser L_D. Figure 4.8 demonstrates the STIRAP spectrum of the $|v = 1, J = 0\rangle$ state. The hyperfine structure is almost the same as that of the rovibrational ground state $|v = 0, J = 0\rangle$ due to their similar hyperfine interaction strengths. In principle, higher excited vibrational levels can also be populated similarly.

As illustrated in Fig. 3.10, the intermediate level can also directly couple to the second excited rotational state $|v = 0, J = 2\rangle$, which enables direct population transfer to the $|v = 0, J = 2\rangle$ state feasible through a single STIRAP. For a $J = 2$ state, there are totally $(2J+1)(2I_{\rm Na}+1)(2I_{\rm Rb}+1) = 80$ hyperfine levels. However, starting from the Feshbach state with $M_F = 2$, only 29 hyperfine levels can be accessed due to the selection rules of angular momentum. Figure 4.9 shows the obtained STIRAP spectrum of the $|v = 0, J = 2\rangle$ state with 22 hyperfine levels resolved. Even at a relatively high B-field of 335.2 G, the span of the spectrum is only about 2.5 MHz and the hyperfine levels are closely distributed. Furthermore, the hyperfine structure is much more complex and there is no monotonous dependence on M_F as that in the $J = 0$ case.

However, the first excited rotational state $|v = 0, J = 1\rangle$ can not be directly accessed through a STIRAP due to the parity selection rule. Thus, a microwave field, operated at a frequency of about $2B_v \approx 4.179$ GHz, is applied to drive a $J = 0 \rightarrow J = 1$ transition after transferring the molecules to the absolute ground state. Thanks to the large permanent electric dipole moments, the microwave driving transitions are typically very strong. Even with the microwave horn antenna (OCEAN MICROWAVE OLB-159-10) placed more than 20 cm away from the sample, we can achieve more than $2\pi \times 100$ kHz Rabi frequency with the microwave power of 1 W. Although the generated microwave is linear polarized, controlling of its polarization has not been accomplished yet and both $\sigma^{\pm}$ and π transitions are driven by the field. To detect the $J = 1$ hyperfine levels, the residual $J = 0$ molecules are monitored as a function of the microwave frequency. Figure 4.10(b) demonstrates the 6 observed hyperfine levels out of the total 10 accessible ones, including one $M_F = 4$, three $M_F = 3$ and six $M_F = 2$ levels. The other four levels are not observed due to their small fractions of the absolute ground-state nuclear spin configuration $|m_I^{\rm Na} = 3/2, m_I^{\rm Rb} = 3/2\rangle$ (see Table 4.2).

To describe the observed hyperfine structure, we utilize the Hamiltonian [157,

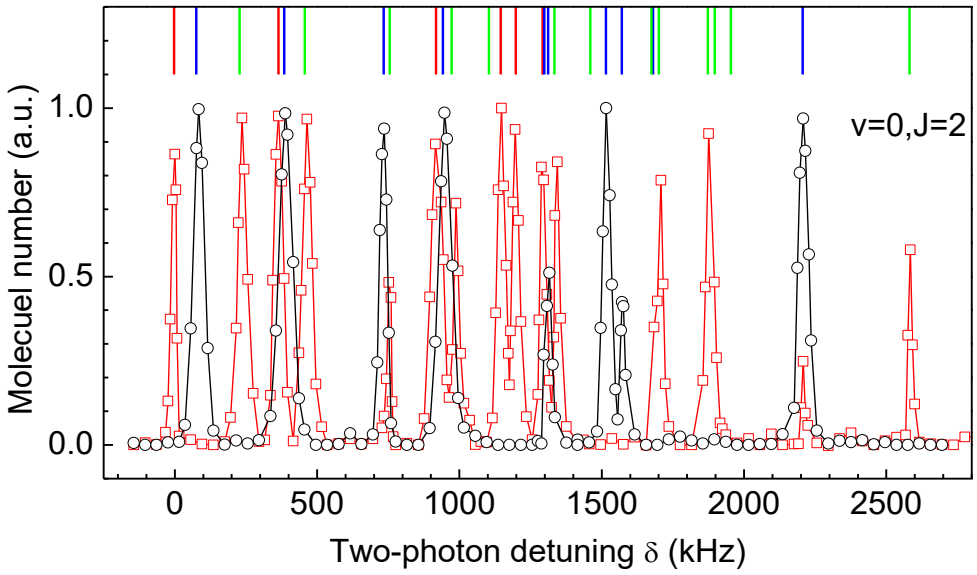

Figure 4.9: STIRAP spectrum of the second excited rotational state $|v = 0, J = 2\rangle$ obtained with 200 μs Raman pulse lengths. The zero two-photon detuning corresponds to a binding energy of 149.19747(6) THz. The black dots are obtained with π polarization of L_D while the red squares with $\sigma^{\pm}$ polarization. The color-coded vertical bars are the calculated positions of the hyperfine levels using the fitted coupling coefficients in Table 4.1. The spectrum is scanned with the optical dipole trap turned off. The two resonances at the same position of $\delta \approx 2200$ kHz, observed with different light polarizations, correspond to a same hyperfine level due to the imperfect $\sigma^{\pm}$ polarization.

158, 89, 176]

$$H = H_{rot} + H_{hf} + H_Z, \tag{4.7}$$

where $H_{rot} = B_v J(J+1)$ represents the rotational splitting.

$$H_Z = -g_r \mu_N \mathbf{J} \cdot \mathbf{B} - \sum_{i=1}^{2} g_i (1 - \sigma_i) \mu_N \mathbf{I}_i \cdot \mathbf{B} \tag{4.8}$$

is the Zeeman effects of the molecular rotation and the nuclear spins with μ_N the nuclear magneton, g_r the rotational g-factor, g_i the nuclear g-factors and σ_i the nuclear shielding tensors (i =Na,Rb).

$$H_{hf} = \sum_{i=1}^{2} \mathbf{V}_i \cdot \mathbf{Q}_i + \sum_{i=1}^{2} c_i \mathbf{J} \cdot \mathbf{I}_i + c_3 \mathbf{I}_1 \cdot \mathbf{T} \cdot \mathbf{I}_2 + c_4 \mathbf{I}_1 \cdot \mathbf{I}_2 \tag{4.9}$$

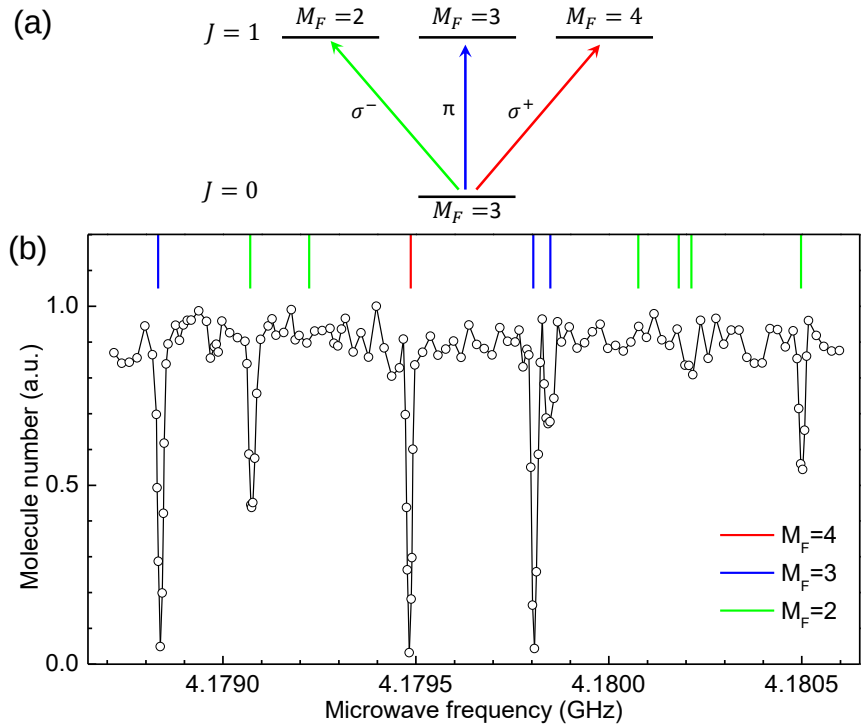

Figure 4.10: Microwave spectroscopy of the $J = 1$ hyperfine levels. (a) Schematic illustration of the microwave transitions from the absolute ground state $|J = 0, M_F = 3\rangle$. (b) The observed $J = 1$ hyperfine levels manifest as loss of the $J = 0$ molecules. The spectrum is obtained with microwave duration of 50 μs, which is shorter than a π pulse for the used power. The color-coded vertical bars are the calculated positions of the hyperfine levels using the fitted coupling coefficients in Table 4.1. The spectrum is implemented with optical dipole trap turned off to eliminate the AC Stark effect.

depicts the hyperfine interactions [157]. The first term

$$\mathbf{V}_i \cdot \mathbf{Q}_i = -\frac{(eqQ)_i}{2I_i(2I_i-1)(2J-1)(2J+3)}[3(\mathbf{I}_i \cdot \mathbf{J})^2 + \frac{3}{2}(\mathbf{I}_i \cdot \mathbf{J}) - \mathbf{I}_i^2\mathbf{J}^2] \quad (4.10)$$

is the electric quadrupole interaction associated with the coupling constants $(eqQ)_i$. While the second term, which is typically very small (Table 4.1), represents the direct couplings between the rotation and the nuclear spins. The term associated with

$$\mathbf{I}_{\mathrm{Na}} \cdot \mathbf{T} \cdot \mathbf{I}_{\mathrm{Rb}} = \frac{3(\mathbf{I}_{\mathrm{Na}} \cdot \mathbf{J})(\mathbf{I}_{\mathrm{Rb}} \cdot \mathbf{J}) + 3(\mathbf{I}_{\mathrm{Rb}} \cdot \mathbf{J})(\mathbf{I}_{\mathrm{Na}} \cdot \mathbf{J}) - 2(\mathbf{I}_{\mathrm{Na}} \cdot \mathbf{I}_{\mathrm{Rb}})\mathbf{J}^2}{(2J-1)(2J+3)}, \quad (4.11)$$

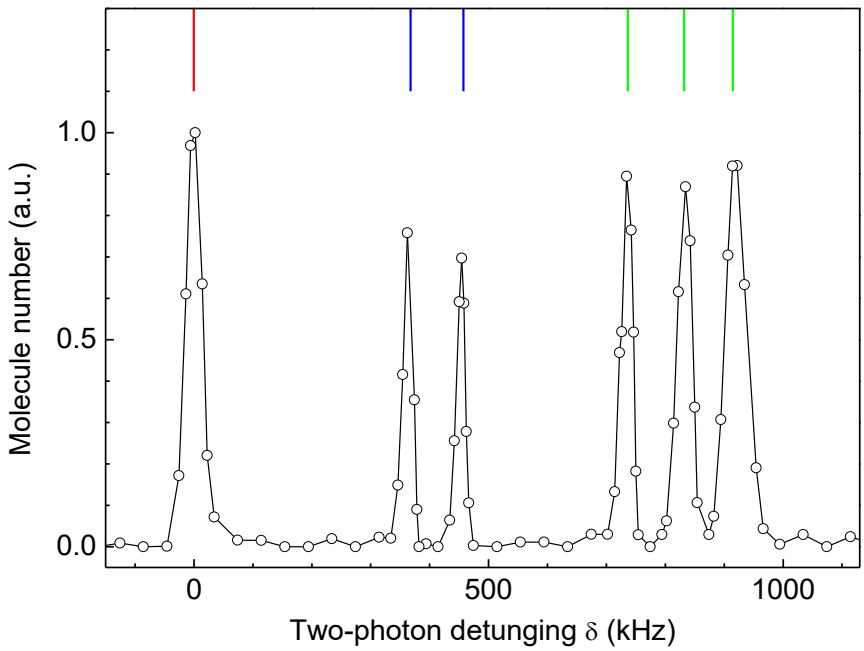

Figure 4.11: STIRAP spectrum of the rovibrational ground state $|v = 0, J = 0\rangle$. The spectrum has similar parameters as in Fig. 4.2(b) but is obtained with the ODT turned off. The color-coded vertical bars are also the calculated positions using the coefficients in Table 4.1.

describes the tensor interactions between the nuclear spins. The last term is the direct scaler coupling within the nuclear spins. For $J = 0$ states, the electric quadrupole interaction vanishes and the Zeeman effect dominates over the other interactions under a B-field of 335.2 G, resulting in monotonous dependence of the hyperfine energy on M_F. However, for excited rotational states, i.e. $J > 0$, the electric quadrupole interaction becomes comparable to the Zeeman effects. Thus, the hyperfine structures of these states are much more complicated.

In order to accurately extract the coupling constants, the positions of the hyperfine levels should be precisely determined and the other unrelated effects should be ruled out. To eliminate the AC stark effect induced by the trapping lights (polarizabilities of different rotational hyperfine levels are different, see Sec. 4.2), the spectra for the $|v = 0, J = 0\rangle$ state (Fig. 4.11), the $|v = 0, J = 1\rangle$ state (Fig. 4.10) and the $|v = 0, J = 2\rangle$ state (Fig. 4.9) are obtained with the

Table 4.1: Extracted coupling constants in the molecular Hamiltonian (Eq. 4.7) for the $v = 0$ state of ^{23}Na^{87}Rb molecules, obtained from the fit to the observed hyperfine levels. As c_{Na}, c_{Rb} and c_3 are very small and barely affect the fitting results, they are fixed to the values provided in Ref. [152] during the fitting process.

Constant	Value	Reference
B_v	2.0896628(4) GHz	This work
	2.09855 GHz	[151]
$(eqQ)_{Na}$	-0.139(40) MHz	This work
	-0.132 MHz	[152]
$(eqQ)_{Rb}$	-3.048(13) MHz	This work
	-2.984 MHz	[152]
c_{Na}	60.7 Hz	[152]
c_{Rb}	983.8 Hz	[152]
c_3	259.3 Hz	[152]
c_4	6.56(23) kHz	This work
	5.73 kHz	[152]
$g_{Na}(1-\sigma_{Na})$	1.484(1)	This work
	1.477	[177]
$g_{Rb}(1-\sigma_{Rb})$	1.832(1)	This work
	1.827	[177]
g_r	0.001(6)	This work

ODT turned off. Using the Hamiltonian (Eq. 4.7) to fit these observed levels, the coupling coefficients of the vibrational ground state are successfully extracted, as summarized in Table 4.1. As the coefficients c_{Na}, c_{Rb} and c_3 are too small to affect the fitting results, they are fixed to the theoretical values from Ref. [152]. The fitting results, represented by the color-coded vertical bars in Fig. 4.11, Fig. 4.10(b) and Fig. 4.9, agree well with the experiment. The differences between the observed positions and the fitting ones (vertical bars) for all these levels are within 10 kHz.

Due to the hyperfine coupling interactions, the bare states $|J, M_J, m_I^{\mathrm{Na}}, m_I^{\mathrm{Rb}}\rangle$ are no longer eigenstates of the system and each hyperfine level is a superposition

Table 4.2: Component fractions of several $J = 0$ hyperfine levels under a B-field of 335.2 G using the coupling constants in Table 4.1. $E_{\rm hf}$ is the hyperfine energy of corresponding level.

M_F	$E_{\rm hf}$ (kHz)	Main component		$2^{\rm nd}$ Main component	
		$\|J, M_J, m_I^{\rm Na}, m_I^{\rm Rb}\rangle$	Weight	$\|J, M_J, m_I^{\rm Na}, m_I^{\rm Rb}\rangle$	Weight
3	-1253	$\|0, 0, 3/2, 3/2\rangle$	100%	-	-
2	-885	$\|0, 0, 1/2, 3/2\rangle$	98.8%	$\|0, 0, 3/2, 1/2\rangle$	1.2%
2	-796	$\|0, 0, 3/2, 1/2\rangle$	98.8%	$\|0, 0, 1/2, 3/2\rangle$	1.2%
1	-516	$\|0, 0, -1/2, 3/2\rangle$	98.6%	$\|0, 0, 1/2, 1/2\rangle$	1.4%
1	-421	$\|0, 0, 1/2, 1/2\rangle$	96.7%	$\|0, 0, -1/2, 3/2\rangle$	1.9%
1	-338	$\|0, 0, 3/2, -1/2\rangle$	98.1%	$\|0, 0, 1/2, 1/2\rangle$	1.9%

of these bare states. Utilizing the coupling coefficients in Table 4.1, the bare-state fractions of the hyperfine levels can be determined. The components fractions of the relevant hyperfine levels of the $J = 0$ and $J = 1$ states at a B-field of 335.2 G are listed in Table 4.2 and Table 4.3. For $J = 0$ levels, due to the vanishing electric quadrupole interactions, the bare states are weakly coupled (Table 4.2). However, strong mixings in $J = 1$ hyperfine levels (Table 4.3) emerge due to the strong electric quadrupole interactions. As a result, a single hyperfine level can have significant components of several bare states, for example the first $M_F = 2$ level with $E_{\rm hf} = -1510$ kHz in Table 4.3 has 71% of $|1, -1, 3/2, 3/2\rangle$, 19% of $|1, 1, 3/2, -1/2\rangle$ and 10% of $|1, 0, 3/2, 1/2\rangle$ (not listed).

This strong mixing of the bare states in the $J = 1$ hyperfine levels is of great significance as it opens new possibility to coherently control the hyperfine degree of freedom (nuclear spins) of the $J = 0$ state by microwave couplings to $J = 1$ levels [87, 88, 89]. Typically, the microwave fields only couple rotational levels with the same nuclear spins configuration following $\Delta J = \pm 1$ and $\Delta M_J = 0, \pm 1$. Thus, if such couplings do no exist, microwave transitions will only change the molecular rotation while leaving the nuclear spins untouched. However, as a $J = 1$ hyperfine level has significant components of different nuclear spins, it can

Table 4.3: The components of several $J = 1$ hyperfine levels at a B-field of 335.2 G using the coupling constants in Table 4.1. $E_{\rm hf}$ is the hyperfine energy with respect to the rotational energy $2B_v = 4.179326$ GHz.

M_F	$E_{\rm hf}$ (kHz)	Main component		$2^{\rm nd}$ Main component	
		$\lvert J, M_J, m_I^{\rm Na}, m_I^{\rm Rb}\rangle$	Weight	$\lvert J, M_J, m_I^{\rm Na}, m_I^{\rm Rb}\rangle$	Weight
3	-1747	$\lvert 1, 0, 3/2, 3/2\rangle$	82.2%	$\lvert 1, 1, 3/2, 1/2\rangle$	17.8%
2	-1508	$\lvert 1, -1, 3/2, 3/2\rangle$	70.8%	$\lvert 1, 1, 3/2, -1/2\rangle$	18.9%
2	-1356	$\lvert 1, 0, 1/2, 3/2\rangle$	80.7 %	$\lvert 1, 1, 1/2, 1/2\rangle$	18.8%
4	-1092	$\lvert 1, 1, 3/2, 3/2\rangle$	100%	-	-
3	-774	$\lvert 1, 1, 3/2, 1/2\rangle$	69.3%	$\lvert 1, 1, 1/2, 3/2\rangle$	16.1%
3	-730	$\lvert 1, 1, 1/2, 3/2\rangle$	83.9%	$\lvert 1, 1, 3/2, 1/2\rangle$	12.9%
2	-503	$\lvert 1, 0, 3/2, 1/2\rangle$	65.3%	$\lvert 1, 1, 3/2, -1/2\rangle$	30.1%
2	-398	$\lvert 1, 1, 1/2, 1/2\rangle$	68.8%	$\lvert 1, 0, 1/2, 3/2\rangle$	16.1%
2	-365	$\lvert 1, 1, -1/2, 3/2\rangle$	89.1%	$\lvert 1, 1, 1/2, 1/2\rangle$	8.6%
2	-81	$\lvert 1, 1, 3/2, -1/2\rangle$	48.8%	$\lvert 1, -1, 3/2, 3/2\rangle$	28.9%

bridge different hyperfine levels of the $J = 0$ state simultaneously.

As an example, Figure 4.12 demonstrates the coherent population transfers between the $J = 0$ and $J = 1$ hyperfine levels, where the hyperfine degree of the $J = 0$ state can be coherently controlled via two-photon microwave transitions. The $|1, -1, 3/2, 3/2\rangle$ component of the $J = 1$ level allows it to strongly couple to the absolute ground state $|0, 0, 3/2, 3/2\rangle$ while the other two components of $|1, 0, 3/2, 1/2\rangle$ and $|1, 1, 3/2, -1/2\rangle$ make it possible to transfer to the other hyperfine levels of $J = 0$, as shown in Fig. 4.12(a). After transferring the molecules to the $J = 1$ hyperfine level from the absolute ground state through a microwave π pulse [Fig. 4.12(b)], a second microwave pulse can coherently populate the molecules to the $M_F = 2$ [Fig. 4.12(c)] level or the $M_F = 1$ level [Fig. 4.12(d)] of the $J = 0$ state. From the three Rabi oscillations, the Rabi frequencies are extracted to be $2\pi \times 18.1(1)$ kHz, $2\pi \times 21.8(1)$ kHz and $2\pi \times 10.2(1)$ kHz respectively. The ratio between the Rabi frequencies of the two σ transitions agrees with the calculated component fractions correspondingly, which in turn validates

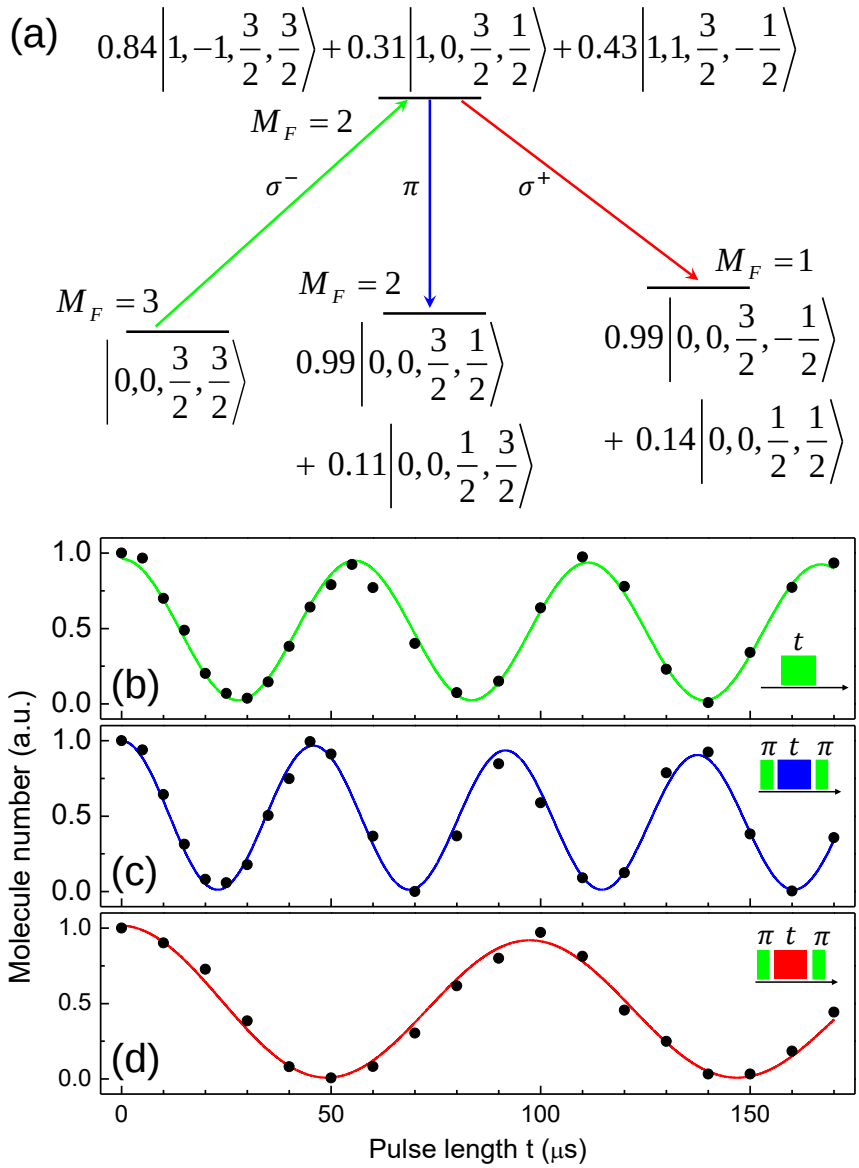

Figure 4.12: Coherent population transfers between the $J = 0$ and $J = 1$ hyperfine levels through microwave pulses. (a) Schematic illustration of an example for the coherent couplings within the presented hyperfine levels. (b), (c) and (d) are the resonant Rabi oscillations of the three microwave transitions in (a).

our theoretical results.

Besides realizing coherent control of the rotational and hyperfine degrees of freedom, microwave fields coupling $J = 0$ and $J = 1$ levels, which possess different parity, can also induce direct DDI within the molecules. Through the induced

dipolar interactions, direct spin exchange has already been observed in lattice-confined KRb molecules [54, 55]. What's more, microwave dressings, combined with static electric fields, make it possible to engineer the long-range interactions and the collisional properties of the molecules [178, 179, 180].

To summarized, I demonstrated successful transfer of the ultracold molecules from the Feshbach state to a single hyperfine level of the singlet ground state with efficiency up to 93%. By combining a STIRAP process with extra microwave fields, full control over the molecular internal states, including the vibrational, rotational and hyperfine degrees of freedom, is achieved. The properties of the absolute ground-state molecules, including the permanent electric dipole moments and their dynamic response to the ODT, are investigated. With precisely located hyperfine levels of the first three rotational states, the hyperfine coupling coefficients for the vibrational ground state are also accurately extracted.

□ End of chapter.

Chapter 5

State Controlled Molecular Collisions

In the last chapter, I have demonstrated our successful creation of ultracold $^{23}Na^{87}Rb$ molecules in their absolute ground state and the determinations of their permanent electric dipole moments and polarizability. Besides, the lifetime of the molecular sample, i.e. how long the molecules can stay in the ODT, is also of great importance. For the absolute ground-state $^{23}Na^{87}Rb$ molecules, the exchange chemical reaction $2NaRb \rightarrow Na_2 + Rb_2$ is energetically forbidden [86, 96, 97, 98] and inelastic collisions are also not allowed. Thus, long-lived molecular samples were expected. However, we found that the molecules suffered from severe loss within several tens of milliseconds [82]. This fast molecular loss do not uniquely emerge within $^{23}Na^{87}Rb$ molecules. In other chemically stable species, including bosonic $^{87}Rb^{133}Cs$ molecule [80] and fermionic $^{23}Na^{40}K$ molecule [79], the unexpected severe losses were also observed. For $^{23}Na^{40}K$ molecule, the loss is suppressed due to its quantum statistic, as two identical fermionic molecules must overcome centrifugal barriers (p-wave) in order to collide.

As for the chemical reactivity of the molecules, one may debate that other types of reactions may be possible even though the exchange reaction is energetically forbidden. However, it was claimed in Ref. [86] that the reactions between

two ground-state alkali-metal dimers to produce a trimer and a free atom, i.e.

$$2\mathrm{NaRb}(v=0,J=0) \rightarrow \mathrm{Na_2Rb}(v=0,J=0) + \mathrm{Rb},$$

and

$$2\mathrm{NaRb}(v=0,J=0) \rightarrow \mathrm{NaRb_2}(v=0,J=0) + \mathrm{Na},$$

are endothermic (with the relevant binding energies listed in Table 5.1). On the other hand, although there should exist many four-atom states, i.e. Na_2Rb_2 molecules, with energy below that of two NaRb molecules, the conservations of total energy and momentum prevent two NaRb dimers forming a Na_2Rb_2 molecule, unless the four-atom molecule has exactly the same energy of the two colliding dimers, i.e. a resonance similar to the Feshbach resonances but within molecules in this case. Thus, as long as the exchange chemical reaction is forbidden, the molecule is chemically stable regarding two-body collisions. For collisions involving three or more molecules, the effects cannot induce such severe loss observed due to the low density of the molecular samples, which is on the order of 10^{11} cm^{-3}. Actually, we have tried to interpret our data with the three-body loss model, but the extracted loss coefficient, which is more than hundred times larger than the unitary limit [181, 182], is unphysical.

At present, the actual loss mechanism of the chemically stable molecules is still not clear. Although a possibility called "sticky" collision forming four-atom complex was proposed [94], it has never been determined. Thus, it is important to investigate the characteristics of the molecular loss behaviors in order to check the "sticky" collision model and get more hints on the loss mechanism.

In this chapter, I will illustrate our investigations on the molecular loss with selectively introduced inelastic channels especially chemical reaction by preparing the molecules to different internal states. In the hyperfine, rotational and vibrational excited states, inelastic channels, including hyperfine relaxation, rotational relaxation, and vibrational decay, can be correspondingly introduced to molecular collisions. What's more, molecules in vibrational excited states can

Table 5.1: Binding energies of the relevant dimers and trimers with respect to the corresponding threshold energies of free atoms. These molecules are in their rotational ground states ($J = 0$) while their vibrational states are specified. $v = 0, 1$ indicate the vibrational ground state and the first excited vibrational state respectively. The numbers in the parentheses are the uncertainties of the measured values.

Species	Binding energy (cm^{-1})	Reference
$Na_2(v = 0)$	5942.688(5)	[98]
$Rb_2(v = 0)$	3965.8(4)	[183]
$NaRb(v = 0)$	4977.308(3)	[132]
$NaRb(v = 1)$	4871.475(3)	[132]
$Na_2Rb(v = 0)$	7649	[86]
$NaRb_2(v = 0)$	6783	[86]

also undergo the exchange chemical reaction. The results on the collisions of the molecules with controlled chemical reactivities can also be found in Ref. [175].

5.1 Collisions with controlled chemical reactivities

As illustrated in Table 5.1, for $^{23}Na^{87}Rb$ molecules in their singlet rovibrational ground state, the exchange chemical reaction:

$$2NaRb(v = 0, J = 0) \rightarrow Na_2(v = 0, J = 0) + Rb_2(v = 0, J = 0)$$

is endothermic by about 47 cm^{-1}. However, the situation is distinct with the molecules occupying the first excited vibrational state, as the reaction

$$2NaRb(v = 1, J = 0) \rightarrow Na_2(v = 0, J = 0) + Rb_2(v = 0, J = 0)$$

is already exothermic by 164 cm^{-1}. This stark difference make it possible to control the chemical reaction through vibrational excitation, which was well established more than 40 years ago [184, 185, 186, 187], but never been investigated in the ultracold regime. By preparing the molecules to the ground state $v = 0$

or the first excited vibrational state $v = 1$, we can investigate the molecular loss behavior without or with extra chemical reaction.

As demonstrated in Sec. 4.3, preparation of molecules in a single hyperfine level of the first excited vibrational state can be achieved by solely tuning the frequency of the dump laser. Furthermore, as the polarizabilities of the $|v = 0, J = 0\rangle$ molecules (674 a.u.) and the $|v = 1, J = 0\rangle$ molecules (690 a.u.) at 1064.4 nm are similar [167], the molecular collision with or without chemical reactivity can be initialized with almost the same condition. Direct comparison between the molecular evolutions can indicate whether the presence of chemical reactivity will make a difference or not.

5.1.1 Universal model for chemical reaction

For the case with chemical reaction, as each reactive collision releases enough energy for the products to escape from the trap directly, post-collision effects can be ignored and the simple two-body loss model is sufficient to interpret the dynamics. If one assume unity loss possibility when two colliding particles enter the short range, universal loss rate is expected. This universality in the ultracold regime has already been observed in a series of molecular species [118, 188, 189, 190], including the ground-state KRb molecules [84] and the LiNa molecules in their triplet ground state [83]. For the universal collisions, the loss coefficients only depend on the long-range interactions between the two colliding particles. For unpolarized molecules, the long-range interaction can be well described by the van der Waals interaction

$$U(R) = -\frac{C_6}{R^6} \tag{5.1}$$

with C_6 the van der Waals coefficient and R the inter-molecule separation. The length scale associated with the interaction is [191]

$$R_{\mathrm{vdW}} \equiv (\frac{2\mu C_6}{\hbar^2})^{1/4}, \tag{5.2}$$

and the characteristic van der Waals energy follows

$$E_{\mathrm{vdW}} \equiv \frac{\hbar^2}{2\mu}(\frac{1}{R_{\mathrm{vdW}}})^2, \tag{5.3}$$

where $\mu = m/2$ is the reduced mass and $\hbar$ is the Planck constant over 2π. Table 5.2 list the C_6 coefficients and the characteristic temperatures T_{vdW} corresponding to E_{vdW} for the relevant colliding particles in our system.

When the sample temperature satisfies $T \ll T_{\mathrm{vdW}}$, the involved collisions enter the Wigner regime [192, 193]. In this region, the universal two-body loss coefficient β is proportional to T^L, with L representing the collisional partial waves. For s-wave scattering ($L = 0$), the loss coefficient follows [194, 195]

$$\beta_U = g\frac{4\pi\hbar}{\mu}\bar{a}. \tag{5.4}$$

Here, $\bar{a} = 0.0761 \times 2\pi \times R_{\mathrm{vdW}}$ and g is a factor to account the distinguishability of the colliding particles, where $g = 2$ for identical particles and $g = 1$ for distinguishable ones. The universal loss rate for s-wave scattering in the Wigner regime is a constant and independent of the sample temperature. Table 5.2 also illustrates the universal loss coefficients for the relevant colliding particles in the Wigner regime (chemical reactions are not all allowed in those species, for non reactive case β is just for reference).

For atomic species, it is relatively easy to reach the Wigner regime due to small C_6 (for example, Na+Rb in Table 5.2), which is mainly from couplings to the electronic excited potentials. However, for molecules near the bottom of the singlet potential, the large permanent electric dipole moment induces strong couplings between rotational levels, resulting in large C_6 coefficients for those molecules. For the singlet ground-state ^{23}Na^{87}Rb molecules as well as the $v = 1$ molecules, they have a large $C_6 \approx 1.3 \times 10^6$ a.u., which is typically more than hundred times larger than that between two atomic species. Thus, the molecules have a low van der Waals temperature of only 3.0 μK. As a consequence, even our coldest sample of about 350 nK has not yet entered the Wigner regime and

Table 5.2: Dispersive C_6 coefficients (the atomic unit is $E_h \times a_0^6$ with E_h the Hartree energy), corresponding temperatures T_{vdW} of the van der Waals energies E_{vdW}, and the s-wave universal loss rates in the Wigner regime (Eq. 5.3). $v = 0, 1$ represent the vibrational ground state and the first excited vibrational state respectively, while "FM" stands for Feshbach molecule. The "Ref." column indicates the source of the C_6 coefficients. The C_6 values for the $v = 0$ and $v = 1$ molecules using our measured permanent dipole moment d_0 (assuming $v = 1$ molecules the same value as that of $v = 0$ molecules) and rotational constant B_v are also demonstrated. The values in the parentheses are the uncertainties mainly stemming from the measured d_0. The C_6 for FM is taken as the value of the last vibrational state of the $X\,^1\Sigma^+$ potential, which should be of the same order as the exact value for FM. Note that chemical reactions are not all allowed within these species, the non reactive β is for reference only.

Species	C_6 (a.u.)	Ref.	$T_{\mathrm{vdW}}(\mu\mathrm{K})$	$\beta(\mathrm{cm}^3/\mathrm{s})$
Na+Rb	2683	[196]	357.3	-
Na+NaRb($v = 0$)	3948	[197]	275.4	1.36×10^{-10}
Rb+NaRb($v = 0$)	6896	[197]	51.1	0.78×10^{-10}
NaRb($v = 0$)	1.525×10^6	[198]	2.8	5.46×10^{-10}
+NaRb($v = 0$)	$1.33(16) \times 10^6$	This work	3.0	5.27×10^{-10}
NaRb($v = 1$)	1.533×10^6	[198]	2.8	5.46×10^{-10}
+NaRb($v = 1$)	$1.33(16) \times 10^6$	This work	3.0	5.28×10^{-10}
NaRb(FM)+NaRb(FM)	1.145×10^4	[198]	32.9	1.6×10^{-10}

the molecular loss coefficient β strongly depends on the sample temperature [175, 199, 200, 201].

5.1.2 The sticky model

For chemically stable molecules, a so-called "sticky" model, i.e. the molecular collisions are in a highly resonant regime resulting in formation of four-atom complex, was proposed in Ref. [94] as a possible loss mechanism. It was claimed that due to the large density of state for the four-atom complex, which was estimated up to $10^4/(\mu\mathrm{K})$ for $^{23}\mathrm{Na}^{87}\mathrm{Rb}$ molecules [94, 202], the two colliding molecules always see a dense of resonances, which enable two dimers to form a

four-body complex once they are close to each other. The concept of complex is borrowed from the transition complex in chemical reactions, but here with distinct properties. As the formation of complex here do not release extra energy, the complex should not escape from the trap as long as it can be intrinsically trapped by the ODT. More importantly, due to the large density of state for the four-atom complex, the Rice-Ramsperger-Kassel-Marcus (RRKM) theory [203, 204, 205] predicts that the complex lifetime $\tau = 2\pi\hbar\rho/N_o$ can be longer than 0.1 s. Here, ρ is the complex density of state and N_o is the number of open channel, which satisfies $N_o = 1$ for the absolute ground-state molecule. However, for chemical reactive case, τ is smaller than 1 μs due to large N_o.

To check the sticky-collision model, the direct evidence is to detect the long-lived complex. However, due to the lack of knowledge about the complex and proper detection method, we can only monitor the ground-state molecule at present. As has been proved in Ref. [94], the ground-state molecule loss rate due to complex forming, which also assumes unity loss possibility in short range, is exactly the same as that for chemical reactions. However, due to the long lifetime of the complex, if it can be trapped, the post complex-forming dynamics should have certain effects, distinct from the simple two-body loss model for the chemically reactive case. For the post complex-forming collisions, if there are, the complex can relax to lower states by colliding with another ground-state molecule or complex, which can release enough energy for the colliding particles to escape. Besides, a complex can also dissociate back to two ground-state molecules at a time scale of τ, inducing revival of the molecules. Although we cannot detect the complex directly at present, any signature of the post complex-forming dynamics will strongly support the sticky-collision model.

5.1.3 Temperature dependent loss coefficient

In order to figure out whether there are any differences between the dynamics with and without the chemical reactivity, the losses of the molecules prepared

to the lowest hyperfine level ($M_F = 3$) of the absolute ground state and the first excited vibrational state (hereafter, labeled as $v = 0$ and $v = 1$ unless specified) are measured. The experiments start from cigar-shaped (the weak confinement along a horizontal direction) pure samples of FMs at a B-field of 335.2 G along the vertical direction. Population transfers to the $v = 0$ and the $v = 1$ state are achieved via STIRAPs with efficiencies higher than 90%. To compensate the different polarizabilities of the FM and the $v = 0$ ($v = 1$) molecule, the beam powers for the ODT are ramped up directly after the STIRAP within 100 μs. With this method, the undesired breathing motion after the population transfer is greatly suppressed. Then, the molecules are held in the ODT for various of time before detection. As direct detection of the ground-state molecule is not available at present, we need another STIRAP to transfer the molecules back to the Feshbach state and then measure the molecule number and temperature as described in Sec. 2.2, assuming the STIRAP processes do not change the temperature of the molecular sample. For obtaining higher signal-to-noise ratio, the absorption imaging was carried out along the weak confining axis with higher column density. To get accurate molecule number, the calibration of the absorption imaging to account the finite intensity of the probing light and its imperfect polarization was achieved following Ref. [206, 207].

Figure 5.1 illustrates the typical number N and temperature T evolutions of the molecules prepared to the $v = 0$ state and the $v = 1$ state. Accompanying with the molecular loss, increasing of the sample temperature was also observed. One contribution to the heating is the preferred occurrence of the loss collisions at the bottom of the trap with higher density and smaller potential energy. On the other hand, out of the Wigner regime, collisions with lower collision energy are more likely to happen. Thus, the collisions are more favorable to remove molecules that have smaller total energies. In order to figure out any difference between the dynamics of $v = 0$ and $v = 1$ molecules, the holding time reaches up to 3 s with the variation of the molecule number of more than 40 times, as shown

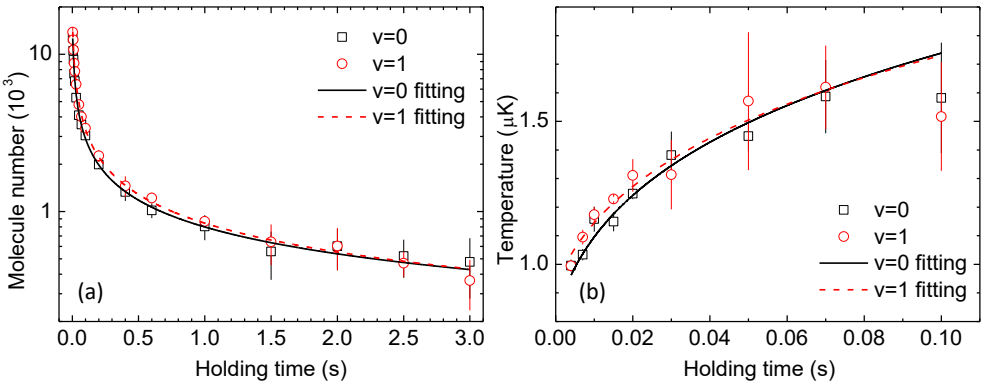

Figure 5.1: Typical number evolution (a) and temperature evolution (b) of the $v = 0$ and $v = 1$ molecules. The error bars represent the statistical uncertainties for more than three shots. The black solid and red dashed curves are fittings to the $v = 0$ and $v = 1$ cases with temperature dependent loss rate (see text). The measured trap frequencies are $\{\omega_x, \omega_y, \omega_z\} = 2\pi \times \{38(2), 208(3), 217(3)\}$ Hz for $v = 0$ molecules and $2\pi \times \{40(2), 205(2), 219(3)\}$ Hz for $v = 1$ molecules.

in Fig. 5.1. Limited by the signal-to-noise ratio, the temperature evolutions are only measured to 100 ms holding time. Noticeably, the dynamics for $v = 0$ and $v = 1$ molecules of different chemical reactivities are almost the same relative to the detection uncertainties within the range of measurement, which should be large enough to observe any difference if there is.

For the chemically reactive case, it is sufficient to interpret the dynamics with simple two-body loss model:

$$\frac{dN(t)}{dt} = -\beta A \frac{N(t)^2}{T(t)^{3/2}}, \tag{5.5}$$

$$\frac{dT(t)}{dt} = (\frac{1}{4} + h_0)\beta A \frac{N(t)}{T(t)^{1/2}}. \tag{5.6}$$

Here, $A = (m\bar{\omega}^2/4\pi k_B)^{3/2}$ is a constant related to the mass m and the geometric mean trap frequency $\bar{\omega} = (\omega_x\omega_y\omega_z)^{1/3}$ of the molecules. The trap frequencies of the molecules are obtained by measuring the center-of-mass motion of the molecules in the trap (Sec. 4.2.2). The second equation accounts the anti-evaporation effects accompanying the two-body loss with the quarter in the bracket induced by the potential energy [181] and h_0 due to the kinetic energy.

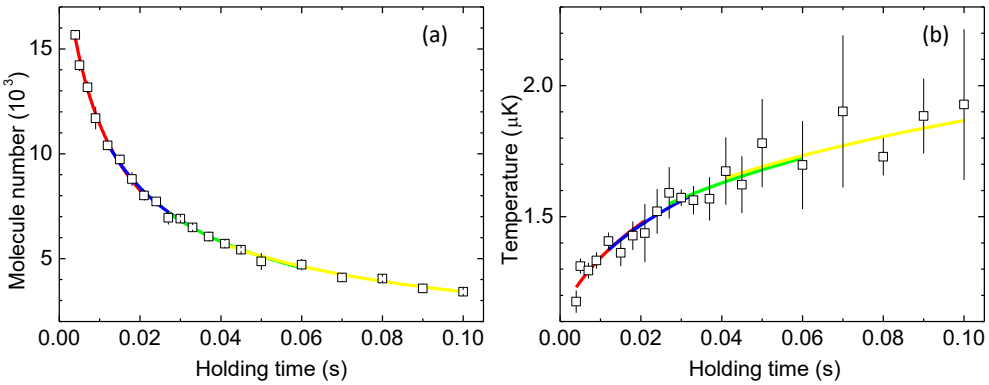

Figure 5.2: Fitting to the molecule number and temperature evolutions using two-body loss model (see text). Due to the temperature dependence of the loss rate, the whole loss curve are separated into four sections. Within each section, the temperature rise is less than 20%. Thus, we assume constant loss rates in the four sections, which are individually fitted as indicated by the colored curves. The error bars are the statistic uncertainties for three repeated measurements.

As we are in the non-Wigner regime, the loss rates depend on the sample temperature. Thus, β is not a constant during the whole dynamics, which makes the fitting process complicated. To simplify this, we separate the dynamics into four sections, with the temperature rise less than 20% within each section [208]. In this case, each section is fitted individually with a constant β, as indicated by the four colored curves in Fig. 5.2. For the fitting, we assume the thermal equilibrium is always fulfilled and the evaporation effect during the dynamics can be ignored as the trap depth is always more than 3 times higher than the sample temperature. To extract the temperature dependence of β, we obtained a series of dynamical data with different initial sample temperatures by tuning the final stage of the ODT evaporation for the atomic mixtures. Figure 5.3 illustrates the measured β as a function of the average temperature for each fit.

For the chemically stable ($v = 0$) case, the two-body loss model is in principle not enough to interpret the dynamics due to the possible presence of the post complex-forming collisions. However, the almost the same dynamics for the reactive case and the stable case (Fig. 5.1) seems to indicate ignorable effects of

the post complex-forming collisions on the $v = 0$ molecules, which means that complexes escape from the trap directly once formed. This can result from the untrappable character of the complex by the ODT as well as the excitation of the complex by the 1064.4 nm trap light. Thus, for simplicity, we also use the two-body model to obtain the $v = 0$ loss rates, while the full model fitting will be discussed in the next section. The extracted loss coefficients as a function of the average sample temperature are shown in Fig. 5.3 (blue squares). Note that although the number evolution for the two cases in Fig. 5.1 are almost the same, the density of $v = 1$ molecules is a bit higher than that of $v = 0$ case due to the larger polarizability for $v = 1$ molecules. Thus, $v = 1$ loss rates are typically smaller than that of $v = 0$ molecules, as shown in Fig. 5.3.

Figure 5.3 illustrates the comparison between β of the two cases as a function of the sample temperature. It is quite unexpected and counterintuitive that the $v = 1$ loss coefficients are smaller within the temperature range from 500 nK to 1.85 μK. As the molecules in the $v = 0$ and $v = 1$ states have quite similar long-range interaction coefficients C_6, the difference on their loss rates should result from their different short-range loss possibilities, if the post complex-forming collisions can be ignored for the $v = 0$ case. For non-unity loss possibilities, the temperature dependent loss coefficients should features several oscillations. However, due to the relatively large fluctuation of the measured β, the oscillations of the loss coefficients cannot be claimed or ruled out. On the other hand, both loss rates decrease with increasing temperature within the measured range, which is a signature of the non-Wigner-regime collisions. Figure 5.3 also shows the theoretical results with the close-coupling method [209, 210, 211] by our cooperators, which assumes unity short-range loss possibilities for both cases. There is no any free parameter in the calculation and it is consistent with the results obtained by the multi-channel quantum defect theory [199]. The theoretical curves for the $v = 0$ and $v = 1$ cases overlap almost exactly and already reach reasonable agreement with the experimental measurements. At higher temperature as indicated

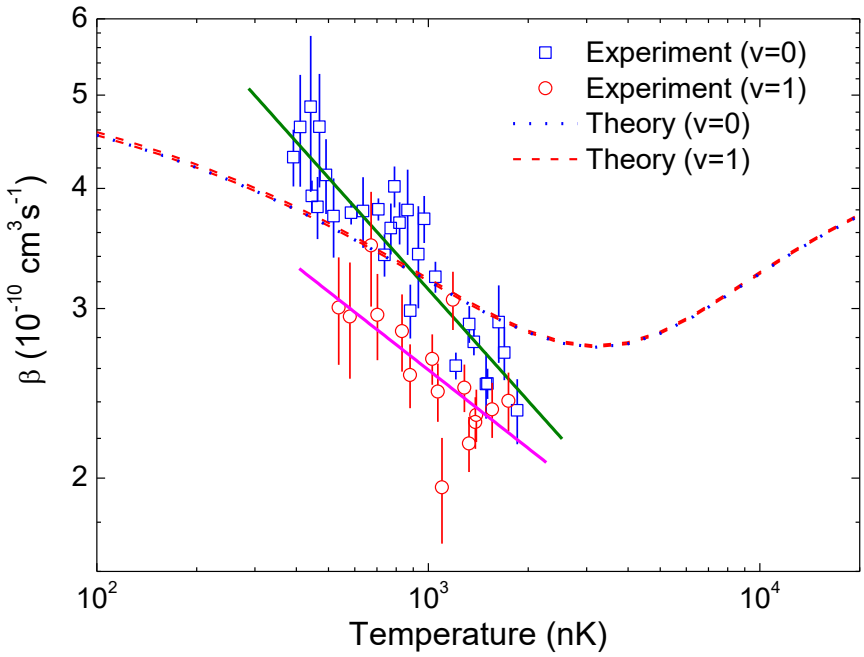

Figure 5.3: Temperature dependent β for $v = 0$ and $v = 1$ molecules plotted in the log-log scale. Each experimental data together with a fitting error bar was obtained through a segment fitting with the two-body loss model (see text). The solid lines are fits of β to power-law functions of sample temperature T. The theoretical curves are based on the CC calculation. For the $v = 0$ case, the theoretical curve demonstrates the "loss rate" of the molecules due to complex forming only.

by the theoretical curves, the loss coefficients increase in accompany with the temperature due to the non ignorable effects of higher scattering partial waves. The turning point, which exactly corresponds to $T_{\rm vdW}$, provides a novel way to measure the van der Waals interaction between two molecules.

To extract the temperature dependence of β, we fit the measured loss rates with a power-law function of the sample temperature, i.e. $\beta(T) = \beta_0(T/T_0)^b$ with β_0 the loss rate at a temperature of T_0. The fitting results are the straight lines shown in Fig. 5.3. The fitted slopes are $b = -0.38(4)$ for the $v = 0$ case and $b = -0.27(8)$ for the $v = 1$ case. These slopes are in turn used as known temperature dependence of β to fit the whole-range dynamics in Fig. 5.1 without

separating it into sections. The fitted curves are shown in Fig. 5.1, which give $\beta_0 = 3.5(1)\times10^{-10}$ cm^3/s for the $v = 0$ molecules and $\beta_0 = 3.0(1)\times10^{-10}$ cm^3/s for the $v = 1$ molecules with T_0 fixed to 1 μK. These values are consistent with those in Fig. 5.3 around 1 μK within the uncertainties. This self-consistent agreement validate the β extracted through segmental fittings.

5.1.4 Full model for the chemically stable collisions

Although the similar dynamics for the $v = 0$ and $v = 1$ molecules seems to indicate ignorable post complex-forming collisions, it is not definite. In order to figure out whether the presence of post complex-forming dynamics can also result in similar loss behaviors, we developed a full model accounting all the possible collision channels. For complex involved collisions, the evolutions of the molecule density n_m and the complex density n_c follow [94]

$$\frac{dn_m}{dt} = -\beta_{mm}n_m^2 + 2\gamma n_c - \beta_{mc}n_m n_c, \tag{5.7}$$

$$\frac{dn_c}{dt} = \frac{1}{2}\beta_{mm}n_m^2 - \gamma n_c - \beta_{mc}n_m n_c - \beta_{cc}n_c^2. \tag{5.8}$$

Where, β_{mm}, β_{mc} and β_{cc} correspond to the collision coefficients between molecules, molecule and complex, and within complexes respectively. $\gamma = 1/\tau$ is the rate that a complex dissociates back to two molecules (for the $v = 0$ molecules, complex can only dissociate back to the absolute ground-state molecules as it is the sole open channel). As the complex lifetime τ only relates to the complex density of state, it should be independent to the sample temperature. In this model, the molecule-complex collisions can induce extra loss of the molecules while the dissociation of the complex results in revival of the molecules. Intuitively, there should be certain possibilities that these two effects just cancel each other. On the other hand, if β_{cc} is much larger than the other rate coefficients, i.e. a complex, once formed, directly losses through collision with another complex before colliding with a molecule or dissociating back to a pair of molecules. In both

situations, dynamics for the $v = 0$ molecules could be quite similar as the $v = 1$ case.

However, it is really challenging to quantitatively take the post complex-forming collisions into account, i.e. fitting the dynamics with the full model, due to the unknown complex properties and the temperature dependence of the loss coefficient β. For simplicity, we take several assumptions: 1) The polarizability of the complex is just the sum of two ground-state molecules, i.e. $\bar{\omega}_c = \bar{\omega}_m \equiv \bar{\omega}$. 2) The temperature dependent molecule-molecule loss coefficient follows $\beta_{mm}(T) = \beta 0_{mm}(T/T_0)^b$ with $b = -0.38$ taken from Sec. 5.1.3. 3) β_{mc} and β_{cc} are temperature independent. 4) Molecule-complex and complex-complex collisions induce direct loss of colliding particles. 5) The formed complexes always get thermalized with the molecules. Then, the full model for the number and temperature evolution of the molecules should follow:

$$\frac{dN_m}{dt} = -\beta_{mm}(T)\frac{A_{mm}N_m^2}{T^{3/2}} + 2\gamma N_c - \beta_{mc}\frac{A_{mc}N_mN_c}{T^{3/2}}, \tag{5.9}$$

$$\frac{dN_c}{dt} = \frac{1}{2}\beta_{mm}(T)\frac{A_{mm}N_m^2}{T^{3/2}} - \gamma N_c - \beta_{mc}\frac{A_{mc}N_mN_c}{T^{3/2}} - \beta_{cc}\frac{A_{cc}N_c^2}{T^{3/2}}, \tag{5.10}$$

$$\begin{aligned}\frac{dT}{dt} =&(\frac{1}{4} + h_0)\beta_{mm}(T)\frac{A_{mm}N_m^2}{(N_m+N_c)T^{1/2}} + \frac{1}{2}\beta_{mc}\frac{A_{mc}N_mN_c}{(N_m+N_c)T^{1/2}} \\ &+ \frac{1}{4}\beta_{cc}\frac{A_{cc}N_c^2}{(N_m+N_c)T^{1/2}} - \frac{1}{2}\gamma\frac{N_cT}{N_m+N_c},\end{aligned} \tag{5.11}$$

with $A_{mm} = (m\bar{\omega}^2/4\pi k_B)^{3/2}$, $A_{mc} = (m\bar{\omega}^2/3\pi k_B)^{3/2}$, and $A_{cc} = (m\bar{\omega}^2/2\pi k_B)^{3/2}$. Here, the parameter m is the molecular mass and h_0 in Eq. 5.11 accounts the anti-evaporation effect induced by the collision energy (temperature) dependent β_{mm}, the same as in Eq. 5.6.

As discussed above, there are intuitively two cases in which the molecular dynamics could behave similarly to the two-body loss. According to the two situations, the full model is simplified: β_{cc} is fixed to zero in case 1 while we set $\beta_{mc} = 0$ for case 2. To quantify the qualities of the fits, the normalized chi-square

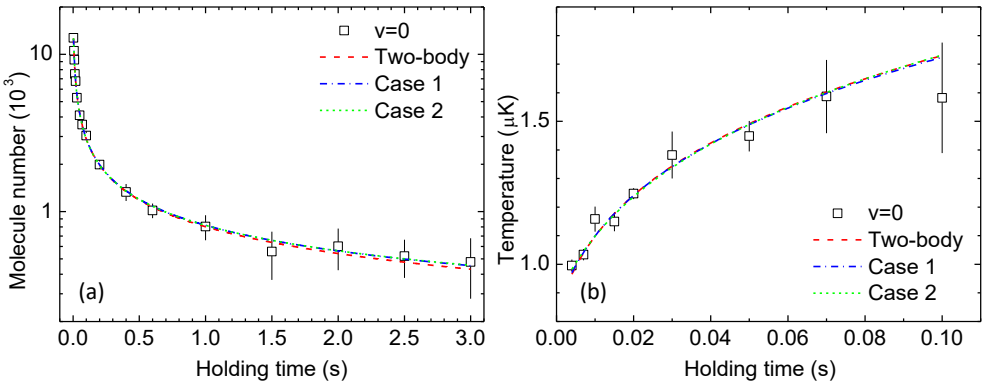

Figure 5.4: Fits to the dynamics of the $v = 0$ molecules with simple two-body loss model and the two cases of the full model. The experimental data and the two-body fitting results are the same as in Fig. 5.1, respectively. For the full model, β_{cc} is fixed to zero in case 1 while β_{mc} is set to zero for case 2. All the three fits have achieved remarkable agreement with the experimental data. Besides, within the experiment fluctuations, the three curves can be hardly distinguished. The temperature dependence of β_{mm} is taken as $\beta_{mm} = \beta 0_{mm}(T/T_0)^{-0.38}$ for all the three fittings.

is also calculated

$$\chi^2 = \sum_{N,T,i} \frac{(y_i - \bar{y}_i)^2}{\Delta y_i^2}. \tag{5.12}$$

Here, y_i is the fitted value, $\bar{y}_i$ and Δy_i are the average and standard deviation of experimental measurements. The fitting results and parameters are shown in Fig. 5.4 and Table 5.3, in comparison to the simple two-body loss model. Although the three sets of parameters are different, the fitted curves almost overlap with each other and the χ^2 are quite the same. Furthermore, the obtained parameters also seem to be reasonable, i.e. all the three cases could be possible. Note that the extracted $\beta 0_{mm}$ for the two-body model and case 2 are quite close while remarkably smaller for case 1. It can be easily understood as the molecule-complex collision in case 1 induces extra loss of molecules. While in case 2, the molecule-complex collision is ignored and the complex has long lifetime relative to the complex-complex collisions rate, which suppresses the revival signal.

One thing need to be emphasized is that many series of the parameters, whose

Table 5.3: Parameters for the three fits in Fig. 5.4. $\beta 0_{mm}$ is the fitted molecule-molecule collision rate corresponding to $T_0 = 1$ μK. $N0$ and $T0$ (different from T_0) are the fitted initial molecule number and temperature with holding time $t = 0$. χ^2 is the normalized chi-square to monitor the fit quality, which are quite similar for all the three fits. The values in parentheses are the fitted uncertainties of the corresponding parameters.

Parameters	Two-body model	Case 1	Case 2
$\beta 0_{mm}$ (10^{-10} cm^3/s)	3.5(1)	2.26(6)	3.55(6)
β_{mc} (10^{-10} cm^3/s)	-	19(11)	0
β_{cc} (10^{-10} cm^3/s)	-	0	10.8(3.5)
τ (s)	-	1.1(6)	18(13)
h_0	0.14(1)	0.09(3)	0.06(1)
$N0$ (10^4)	1.72(7)	1.65(9)	1.72(9)
$T0$ (nK)	860(18)	882(14)	898(12)
χ^2	9.1	9.0	9.1

values can be quite different, can reach reasonable fitting results, i.e. comparable χ^2. It turns out that the limitation of the fitting χ^2 should be the data quality instead of the fitting parameters. Figure 5.4 only shows two typical cases while many other possibilities are not demonstrated. Thus, we cannot get deterministic parameters from the full model fittings. However, combining the results of dipolar collisions in the next chapter, which demonstrates impressive consistence between the saturated values of β_{mm} using the two-body model and the correspondingly theoretical s-wave unitary limit, case 1 in Fig. 5.4 and Table 5.3 that has much smaller β_{mm} should be less likely to happen.

As the full model fitting do not get a definite convergence of the fitted parameters, it is hard to claim whether there are post complex-forming collisions or not. However, together with the results of the dipolar collisions (next chapter), the actual molecule-molecule collision rates should be close to the extracted values using the two-body model. In this case, molecule-complex collision should happen with relatively slow rates. Thus, it is more likely that the complex losses from

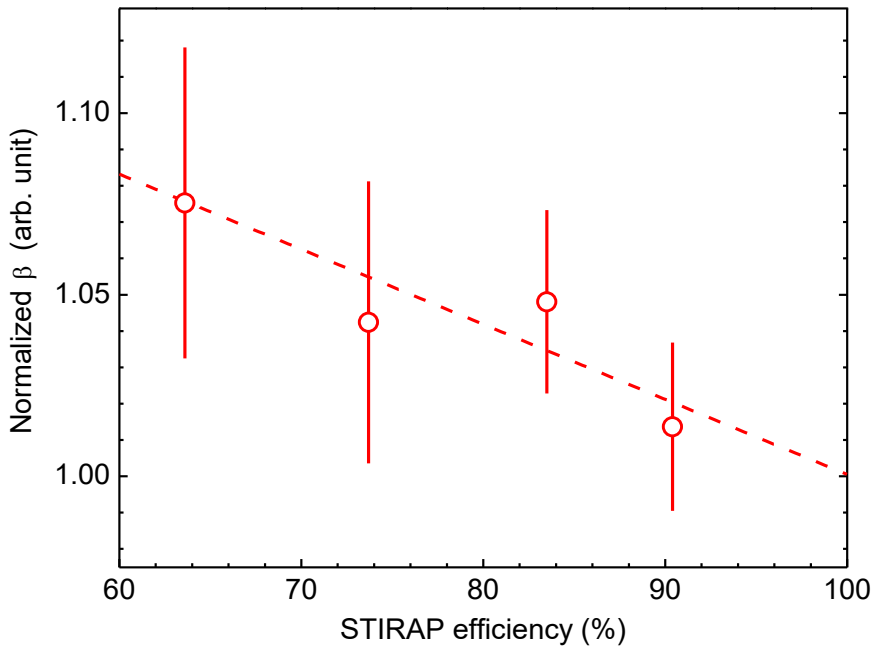

Figure 5.5: The extracted β, which are normalized to the loss coefficient with unity transfer efficiency, using the two-body loss model. The STIRAP efficiency is tuned from 65% to 90%. The dashed line is linear fit to the data, which gives about 1.8% increase on the extracted β accompanying 10% decrease of the STIRAP efficiency.

the trap upon forming through directly escape or fast complex-complex collision before colliding with another molecule.

5.2 Effect of STIRAP efficiency

In the above discussion, we assume the start point of the dynamics is a pure sample of molecules in the desired internal state. However, due to the imperfect 100% STIRAP transfer efficiency, the other molecules not transferred to the desired state can populate other rovibrational states through spontaneous decay from the intermediate state. Although the molecules in some rovibrational states could be excited or repelled by the ODT beams, there should still be certain populations being trapped. Thus, besides the desired molecules, some "impure"

molecules may also be contained in the samples. The undesired molecules could collide with the target molecules and affect the dynamics. For our typical transfer efficiency of 93%, the number of the "impure" molecules is at most 7%. These small amount of impurities should have ignorable effect on the dynamics.

In order to measure the effect of these impure molecules, we tune the STIRAP efficiency on purpose from 65% to 90%, i.e. changing the ratio of the impurity in the sample, by adjusting the power of the Raman beams. For each case, the molecular loss coefficient is extracted using the two-body model. As expected, with higher impurity ratios, i.e. lower transfer efficiency, the extracted β is larger. However, the increasing amount of the β with 10% decreasing of the efficiency is only about 1.8%, as shown by the linear fit in Fig. 5.5. Thus, with our typical efficiency larger than 90%, the impurity effect is rather small and can be ignored in our analysis.

5.3 Molecular loss in different internal states

In Sec. 5.1, we have investigated the dynamics of the molecules with and without the chemical reactivity. Besides, by preparing the molecules to the other internal states, the inelastic channels, including hyperfine relaxation and rotation relaxation, could be selectively introduced to the molecular samples. Figure 5.6 illustrates the extracted loss coefficients using two-body model with the molecules prepared in different hyperfine and rotational states, including two hyperfine excited states $|0, 0, 3/2, -1/2\rangle$ and $|0, 0, -1/2, 3/2\rangle$, two first excited rotational states $|1, 0, 3/2, 3/2\rangle$ and $|1, 1, 3/2, 3/2\rangle$, and a second excited rotational state $|2, 2, 3/2, -3/2\rangle$. Here, $|J, M_J, m_I^{Na}, m_I^{Rb}\rangle$ is the main component of each state in the bare-state basis. For the $J = 0$ and $J = 2$ molecules, they are prepared directly through a single STIRAP. While, $J = 1$ molecules are populated by imposing a microwave π pulse after transferred to the absolute ground state. To avoid the temperature effect, the dynamics for each internal state is

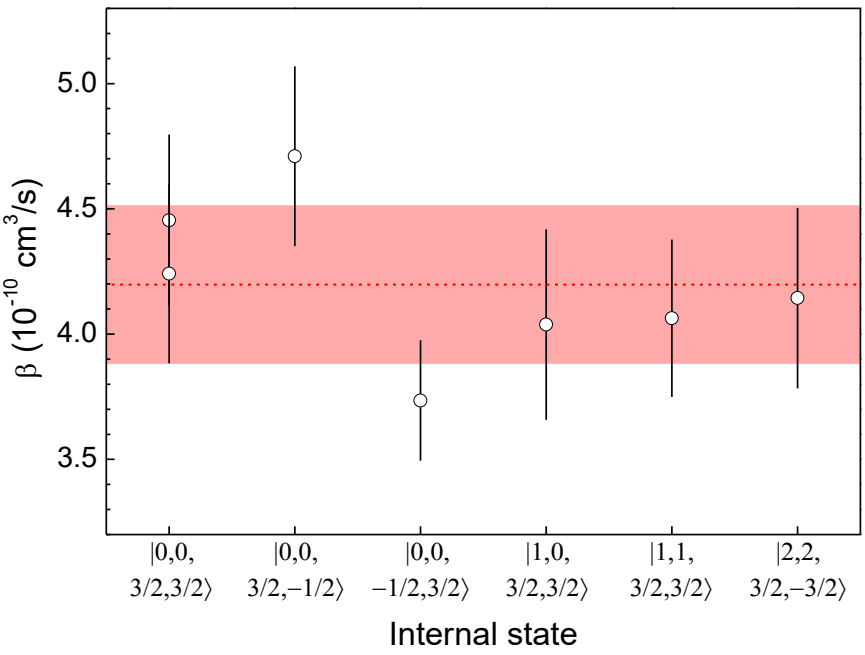

Figure 5.6: Molecular loss coefficients of different hyperfine and rotational levels of the vibrational ground state. The loss rates are extracted using two-body model. Each internal state is labeled by its main component in the bare-state basis $|J, M_J, m_I^{Na}, m_I^{Rb}\rangle$. To avoid the temperature effect, all the data are measured at an average temperature of about 500 nK. The red line and the shadowed region indicate the mean value and standard deviation of the seven data points. The extracted loss coefficients are quite the same for these internal states.

tried to be initialized with the same condition. All sets of the dynamics have almost the same mean temperature of about 500 nK. The results are shown in Fig. 5.6, where no obvious state dependence of the loss coefficient β is observed.

In conclusion, we have investigated the dynamics of molecules prepared in different internal states, i.e. with different loss channels, especially these in the $v = 0$ and $v = 1$ levels with controlled chemical reactivities. One striking and unexpected feature is the severe loss of the absolute ground-state molecules even though all inelastic and reactive collisions are forbidden. Furthermore, the loss rate for the chemically stable case is even larger than that of the reactive case. Out of the Wigner regime, we have observed similar temperature dependence of

the loss coefficients for both collisions. The experimental values are also compared with the prediction of the full "sticky" model, which is a proposed mechanism to explain the unexpected loss. Without any free parameters, the theoretical result already reaches reasonable agreement with the experiment, assuming directly escape of the complex once formed. If unity possibility is assumed at short-range for both the "sticky" model and the chemical reaction, the loss rate of the $v = 0$ molecules due to complex formation should be the same as that for $v = 1$ ones, as a consequence of the quite similar long-range interaction (C_6). Thus, the difference between the loss coefficients of the two cases should results from their different short-range physics.

In order to figure out whether there exist complex-mediated collisions in the v=0 samples, we tried to fit our data with the full model. However, due to the temperature dependence and the complicate collisional processes, we do not get a definitive fitting result even though the number variation already reaches 40 times in our experiments. On the other hand, the results of dipolar collisions (next chapter) seem to support the dynamics with directly loss of the complex. This directly loss could be due to the untrappable property of the complex by the ODT, photon excitation by the trap lights, and the fast complex-complex collisions. Although, our results do not violate the "sticky" model, it is still insufficient to claim that it is the formation of the complex that induce the unexpected loss of the absolute ground-state molecules. Anyway, it is of great significance to gain more knowledge on the complex both theoretically and experimentally, and even to directly detect the complex.

□ End of chapter.

Chapter 6

Ultracold Dipolar Collisions

After successfully preparing the molecules to the absolute ground state, we measured the lifetime of the chemically stable $^{23}Na^{87}Rb$ molecules, where unexpected severe loss was observed. To figure out the loss mechanism, the state dependence and temperature dependence of the loss behavior were studied. In this chapter, I will illustrate our investigations on the molecular collisions with the presence of the tunable long-range dipole-dipole interaction, which will demonstrate how the dipolar interaction affects the molecular dynamics. Besides, it can provide us extra information on the molecular loss mechanism. The paper on the dipolar collisions within the ground-state $^{23}Na^{87}Rb$ molecules is still in preparation [212].

6.1 Stability and inhomogeneity of the E-field

To induce the dipolar interaction, static E-fields are applied through a pair of parallel electric plates (Fig. 2.11). In our experiments, the applied E-field is limited to 0.93 kV/cm, corresponding to an effective dipole moment $d = 0.71$ D, to avoid polarization of the glass vacuum cell. Thanks to the large permanent dipole moments of the ground-state $^{23}Na^{87}Rb$ molecules, the E-field is enough to induce strong dipole-dipole interactions. However, on the other hand, the molecules are also quite sensitive to the fluctuation and inhomogeneity of the E-field. Thus, it is important to characterize the stability and the homogeneity

of the generated E-fields.

6.1.1 The E-field stability

As the effective dipole moment strongly depends on the external E-field, slight instability of the E-field could alter the strength of the dipole-dipole interaction. What's more, fluctuations of certain frequencies, say corresponding to the trap frequencies, may excite and perturb the molecules. In order to check the stability of the applied E-field, we implement the Stark spectroscopy (Fig. 4.3), from which the E-field strength can be extracted, at different delay time after turning on the E-field. Figure 6.1 shows the measured stability of the E-field with two types control of turning on the E-field: one is slowly charging the electrodes in 4 ms, where the delay time is defined after finishing the ramping; the other is stepped on and the position of the step represents the zero delay time. For the step on method, limited by the slew rate the high voltage amplifier and the electrodes dynamic response, it needs some time to reach the desired E-field while overhead and oscillations are also observed during the turning on period. As shown in Fig. 6.1, the E-field fluctuations for both cases after being stabilized (0.5 ms delay time for the second case) are within 0.02%, which is stable enough for our experiments. Moreover, no obvious oscillation of the stabilized E-field at certain frequencies is observed. Experimentally, the E-field is ramped up within 15 to 40 μs.

6.1.2 The E-field inhomogeneity

The inhomogeneity of the E-field including its gradient and curvature could also cause problems. For example, a gradient of 0.07 kV/cm^2 is enough to push the molecules out of the trap with an applied E-field of 0.93 kV/cm. In principle, the E-field gradient and curvature have different effects on the trapped molecules. The gradient could induce shift of the equilibrium position, i.e. excite the center-of-mass oscillation of the samples in the trap or even result in leakage of the

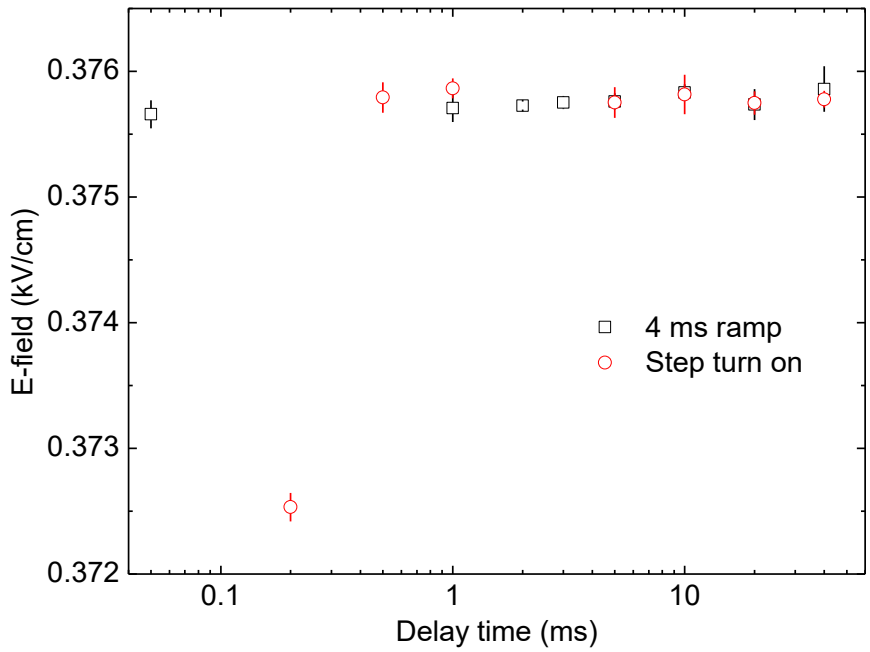

Figure 6.1: The stability of the generated E-field with two types of turning on: slow ramp on in 4 ms (black squares) and turn on with a step function (red circles). The zero delay time (x-axis) corresponds to the end of the ramp and to the starting point of the step function, respectively. The E-field stabilize after a delay time of 0.5 ms for the step-on case. The relative fluctuations of the E-fields for both cases are within 0.02%.

molecules. While the E-field curvature can change the shape of the effective trap, i.e. alter the trap frequencies. Typically, the change of the equilibrium position can also induce shifts of the trap frequencies. For simplicity, we assume the gradient only shifts the equilibrium position while the curvature solely changes the trap frequencies. In this case, these two kinds of inhomogeneities can be evaluated separately.

Figure 6.2 shows the center-of-mass oscillation of an sample of the absolute ground-state molecules along the three axes of the trap without E-field and with an E-field of 0.67 kV/cm. From the shift of the equilibrium position of $\{5.0, 0.6, 2.1\}$ μm and together with the configuration of the ODT, the gradient of the applied E-field is estimated to be $\{0.001, 0.004, 0.011\}$ kV/cm^2 along the

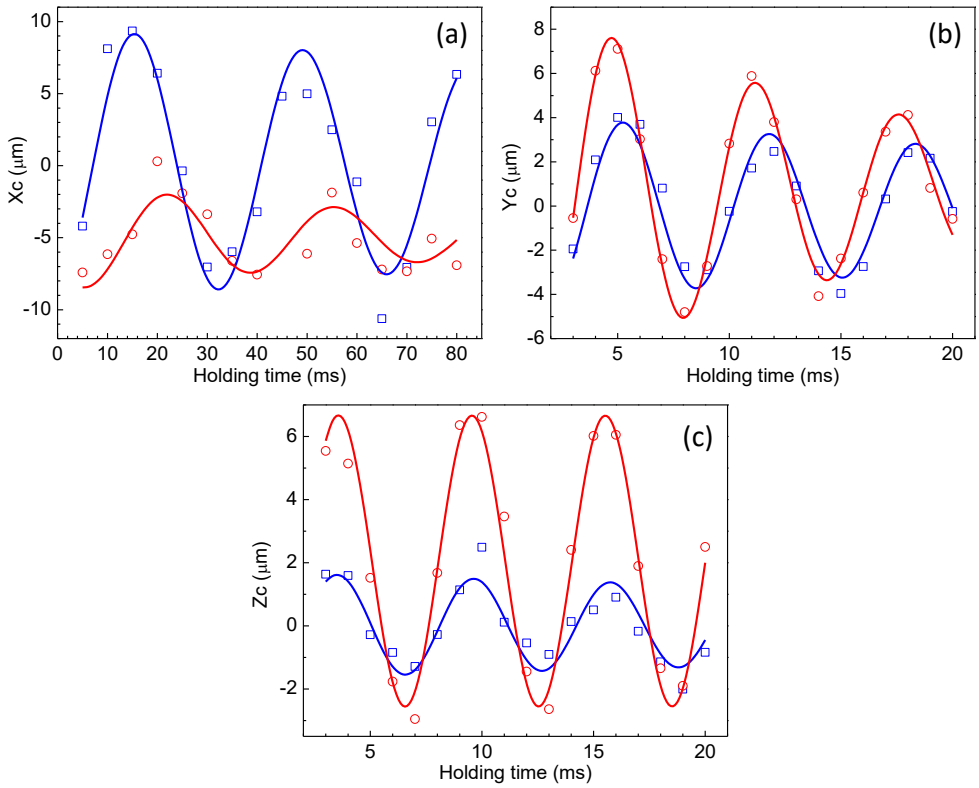

Figure 6.2: Characterizing the E-field inhomogeneity by measuring the molecular oscillations in the ODT with an E-field of 0.67 kV/cm (red) and without E-field (blue). The trap frequencies $\{w_x, w_y, w_z\}$ are extracted to be $2\pi\times\{30(1), 153(2), 163(4)\}$ Hz without E-field and $2\pi\times\{30(2), 156(1), 167(2)\}$ Hz for the 0.67 kV/cm E-field. From the change of trap frequencies, the curvature of the E-field, assuming aligned to the vertical direction, is $\{0.04, 2.0, 2.6\}$ kV/cm^3. From the shift of the equilibrium position of $\{5.0, 0.6, 2.1\}$ μm, the gradient of the E-field is $\{0.001, 0.004, 0.011\}$ kV/cm^2.

three directions respectively. We assume the generated E-field is perfectly aligned along the vertical direction (y axis). On the other hand, the E-field curvature is extracted to be $\{0.04, 2.0, 2.6\}$ kV/cm^3 from the corresponding variation of the trap frequencies. Based on these estimations, the inhomogeneity will only have little influence on our experiment within the range of the applied E-fields.

6.2 Molecular collisions with dipole-dipole interactions

With the presence of the dipole-dipole interaction, the properties of the molecular collisions are greatly modified. On one hand, the interaction strongly couples different scattering partial waves, inducing non-ignorable $L > 0$ collisions even in the ultracold (sub-microkelvin) regime. The p-wave scatterings enhanced by the dipolar interaction have already been observed in the ^{40}K^{87}Rb molecules [50]. On the other hand, the anisotropic characteristic also induces angular dependence of the collisional processes. These distinct properties from the well studied contact interactions make dipolar molecules promising candidates to realize novel Hamiltonians and novel quantum phases in ultracold systems.

To understand how the dipolar interaction affect the collisions within the ^{23}Na^{87}Rb molecules, the Hamiltonian is written as [213, 214]

$$H = T + V_{\rm abs} + V_{\rm vdW} + V_{\rm dd}, \tag{6.1}$$

where $T = -\hbar^2\nabla^2_{\vec{r}}/(2\mu)$ is the kinetic energy with $\vec{r}$ and μ the inter-molecule vector and the reduced mass. $V_{\rm abs}$ absorbs the short-range physics that induces loss of pairs of the colliding molecules. $V_{\rm vdW}$ represents the van der Waals interaction and

$$V_{\rm dd} = \frac{d^2(1-3\sin^2\theta)}{4\pi\epsilon_0 r^3} \tag{6.2}$$

is the dipole-dipole interaction between two molecules with effective dipole moments of d. Here, θ is the angle between $\vec{r}$ and the direction of $\vec{d}$, which is along the applied E-field. By expanding the total wavefunction on the partial-wave basis

$$\Psi(r,\theta,\phi) = \frac{1}{r}\sum_{L,M_L} Y_L^{M_L}(\theta,\phi)F_L^{M_L}(r), \tag{6.3}$$

we obtain a series of coupled radial functions $F_L^{M_L}(r)$ satisfying [213, 214, 215, 216]

$$\{-\frac{\hbar^2}{2\mu}\frac{d^2}{dr^2} + V_{\rm eff} + V_{\rm abs} - E\}F_{LL}^{M_L}(r) + \sum_{L'\neq L} -\frac{2C_3(L,L';M_L)}{r^3}F_{LL'}^{M_L}(r) = 0. \tag{6.4}$$

Here, $Y_L^{M_L}$ is the spherical harmonic functions associated with collisional quantum number L and its projection to the quantization axis M_L. E is the collision energy. The term V_{eff} can be expressed as

$$V_{\text{eff}} = \frac{\hbar^2 L(L+1)}{2\mu r^2} - \frac{C_6}{r^6} - \frac{C_3(L, L; M_L)}{r^3}, \tag{6.5}$$

which represents the effective long-range potential for each partial wave. For the van der Waals interaction, we use the C_6 determined in our experiment, as listed in Table 5.2. The explicit form of the coupling C_3 term is

$$\begin{aligned} C_3(L, L'; M_L) =& \frac{d^2}{4\pi\epsilon_0}(-1)^{M_L}\sqrt{(2L+1)(2L'+1)} \\ & \times \begin{pmatrix} L & 2 & L' \\ 0 & 0 & 0 \end{pmatrix} \begin{pmatrix} L & 2 & L' \\ -M_L & 0 & M_L \end{pmatrix}. \end{aligned} \tag{6.6}$$

For collisions without the dipolar interactions, the scattering partial waves are decoupled and L is a good quantum number. However, these partial waves are coupled by the dipole-dipole interaction. As shown by Eq. 6.6, the dipolar interaction only couples partial waves with the same parity and the same projections M_L, i.e. odd (even) partial waves only directly couple to nearby odd (even) partial waves with the same M_L. Thus, although L is no longer a good quantum number, M_L still is. For ^{23}Na^{87}Rb molecules, which are bosons, prepared to the absolute ground state, only even partial wave scatterings are allowed, including the barrier-less s-wave and barriered d-wave collisions. Note that the diagonal term of C_3 for s-wave vanishes, which means that the modification of the s-wave scattering is purely from couplings to higher partial waves.

To get a decoupled basis, we diagonalize the Hamiltonian in Eq. 6.4 at each r for a certain d, where we account the coupled partial waves up to $L = 10$. Within the accessible E-fields, higher partial waves have little influence on the low partial waves considered here. For convenience, we still denote these eigen bases as s-, d-, g- and ... waves, i.e. $|L, M_L\rangle$, as they asymptotically approach the bare partial waves with $r \to \infty$. Each of these new decoupled bases is associated with

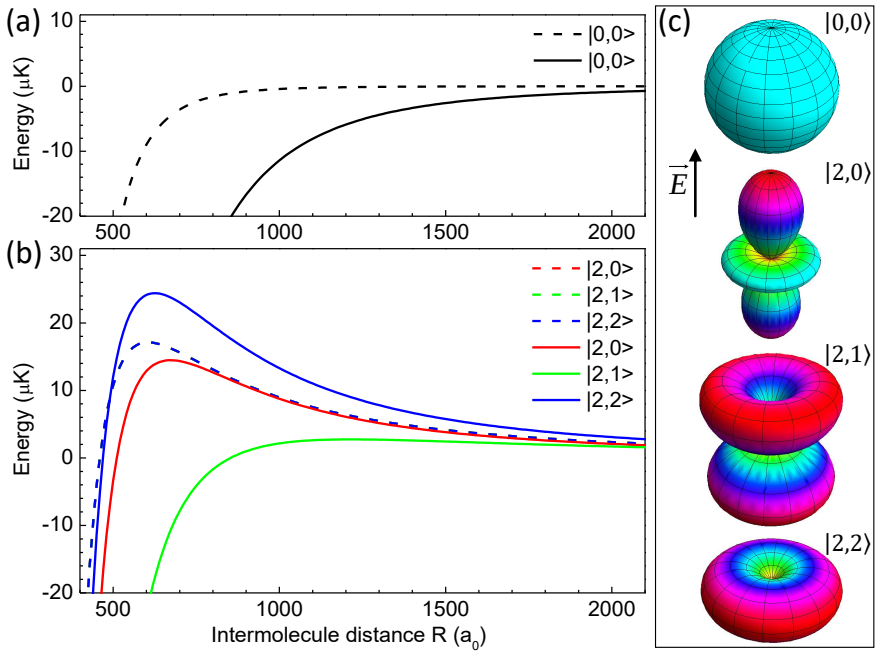

Figure 6.3: The adiabatic potentials for s-wave (a) and d-wave (b) channels with $d = 0$ D (dashed) and 0.5 D (solid). Each decoupled scattering channels are labeled as $|L, |M_L|\rangle$. (c) Polar plots of the spherical harmonic functions to demonstrate the asymptotically ($r \to \infty$) angular dependence of the s-wave and d-wave scattering channels with color indicated amplitude. For s-wave scattering, it is isotropic. However, for d-wave, the main contribution of the $|M_L| = 0$ channel is head-to-tail ($\theta = 0°$) collisions, side-by-side ($\theta = 90°$) collisions for the $|M_L| = 2$ channels, and collisions with $\theta = 45°$ for the $|M_L| = 1$ channels.

an effective adiabatic potential. Figure 6.3 illustrates the adiabatic potentials for s-wave and d-wave with $d = 0$ D and 0.5 D. Without the presence of the dipolar interaction, the five channels for d-wave with different M_L are degenerate. However, the degeneracy between different $|M_L|$ is lifted by the dipolar interaction while maintained within the channels of the same $|M_L|$. Furthermore, the induced couplings of s-wave to higher partial waves by the dipolar interaction down shift the barrier-less potential. However, for d-wave, the barrier is raised for some channels while lowered for the other channels.

To characterize the barrier-less s-wave potential, we utilize a power-law function $-C_\alpha/r^\alpha$ to fit the long-range part ($r > 400$ a$_0$) of the adiabatic potential.

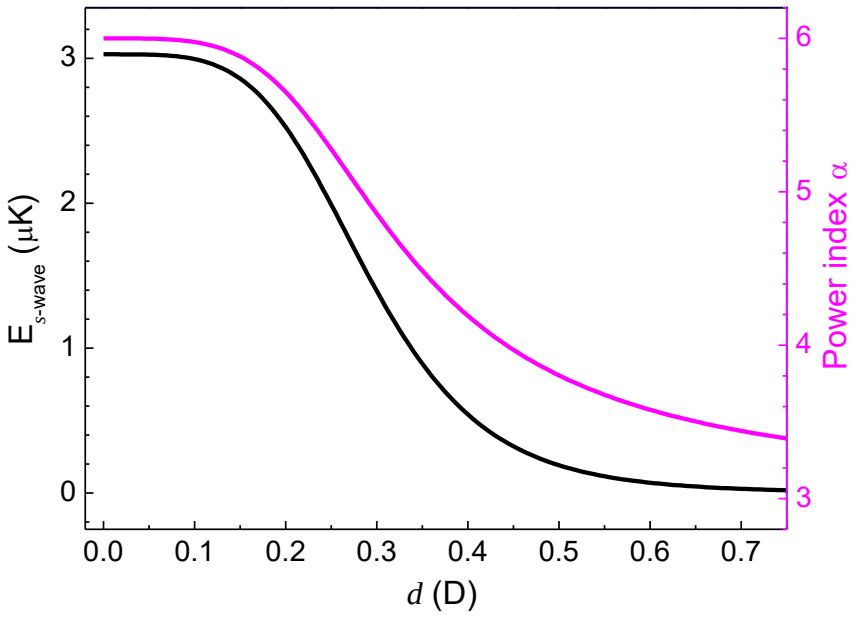

Figure 6.4: Characteristic energy of the barrier-less s-wave potential using power-law function to fit the long-range part of the potential. The fitted power index changes all the way from 6 to approach 3 with increasing effective dipole moment d, indicating the potential transforming from the van der Waals regime to the dipolar interaction dominant region.

Following Ref. [191], the characteristic length and energy of the potential are taken as $r_{s-wave} = (mC_\alpha/\hbar^2)^{1/(\alpha-2)}$ and $E_{s-wave} = \hbar^2/mr_{s-wave}^2$ respectively. Figure 6.4 shows the extracted energy scale E_{s-wave} as well as the fitted power index α as a function of d. The E_{s-wave} decreases monotonously with increasing d. Meanwhile, the fitted power index α changes from 6, the index for the van der Waals interaction, to approach 3, the index of the dipolar interaction, indicating transforming of the effective interaction from the van der Waals region to the dipolar interaction dominant regime. At small $d < 0.2$ D, E_{s-wave} is almost a constant, as the dipole-dipole interaction is much weaker than the van der Waals interaction. With further increasing of d, the E_{s-wave} starts to decrease as the dipolar interaction become comparable with the van der Waals interaction. At high $d > 0.5$ D, the dipolar interaction dominates.

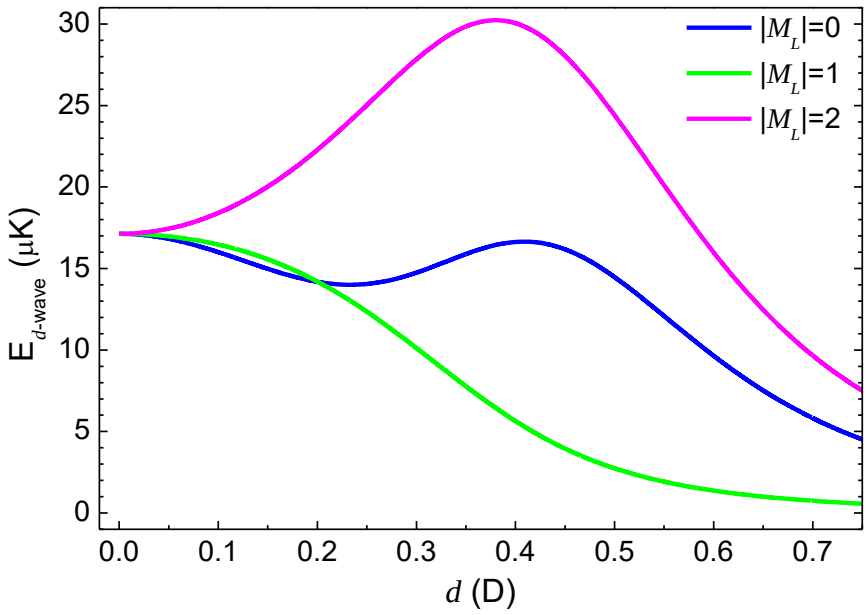

Figure 6.5: Barrier heights of the d-wave scattering channels $|M_L|$ as a function of d.

For the d-wave potentials, the intrinsic energy scales are their barrier heights. Scatterings through d-wave channels should overcome the corresponding barrier in order to enter short range. Figure 6.5 illustrates the barrier heights of the adiabatic potentials for the d-wave channels. The behaviors of the three curves with increasing d are quite different. For $|M_L| = 0$ channel, the first decrease at small d is due to the diagonal term of the dipolar interaction, while the coupling to s-wave results in the subsequent raise, followed by a further decrease at higher d as a consequence of the couplings to higher partial waves. While, both the diagonal interaction and the couplings to higher partial waves lower the barrier for $|M_L| = 1$ channels, inducing monotonous reducing of the barrier height. On the other hand, the competition between the positive diagonal term and the down-pushing couplings results in the first rise of the barrier heights followed by a decreasing behavior for the $|M_L| = 2$ channels.

At $d < 0.3$ D, all the three barriers larger than 10 μK are too high for the colliding molecules with temperature of ~ 1 μK to overcome. When the barrier

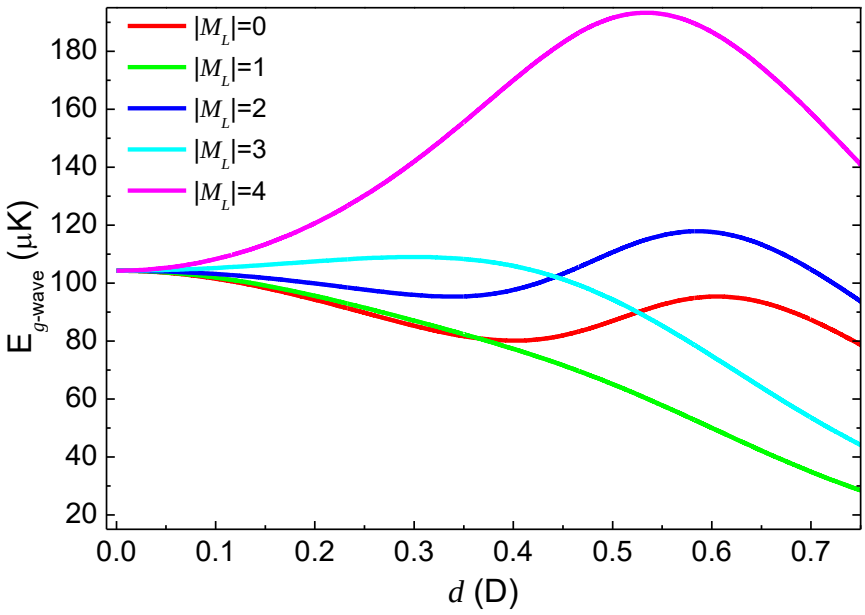

Figure 6.6: Barrier heights of the g-wave scattering channels $|M_L|$ as a function of d. All the barrier heights are too high for the molecules within our accessed E-fields. Thus, collisions through the g-wave can be neglected.

heights of the $|M_L| = 1$ channels are reduced to be comparable to the sample temperature, scatterings through the $|L = 2, |M_L| = 1\rangle$ partial waves starts to play a role. Within the accessible d, the barrier heights for the $|M_L| = 0, 2$ channels are always too high, inducing ignorable contributions from these channels to the collisions. On the other hand, the much lower barrier for $|M_L| = 1$ makes scattering through the channels favorable. Thus, in our experiment, the main contribution of the d-wave scattering should be attributed to the $|M_L| = 1$ channels.

In order to check whether higher order scatterings can happen or not, we also calculate the barrier heights for the g-wave channels, as shown in Fig. 6.6. Within the achievable E-fields, all the g-wave channels have barrier heights larger than 20 μK. Thus, in our current experimental conditions, higher partial waves will play ignorable roles in the collisional processes.

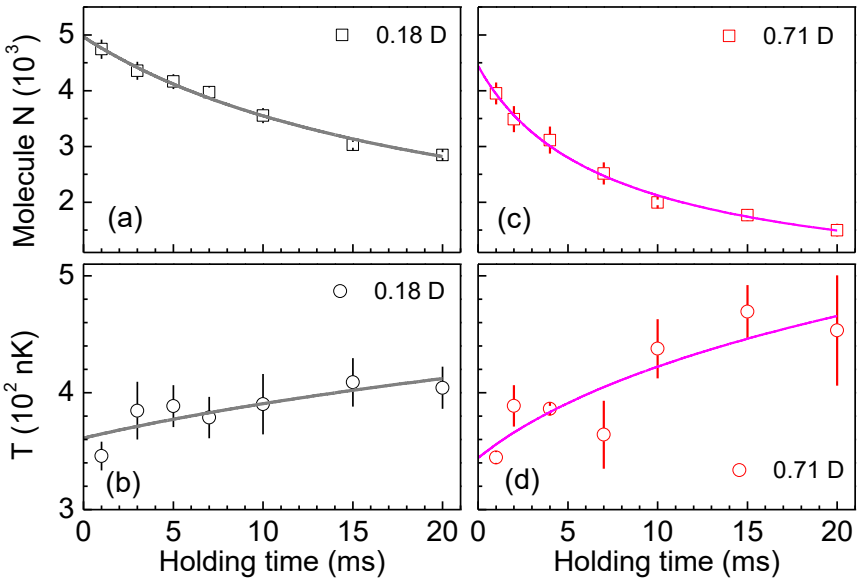

Figure 6.7: Molecule evolutions with effective dipole moments of 0.18 D [(a) & (b)] and 0.71 D [(c) & (d)]. Obviously, more severe molecular loss and heating effect happen at higher E-fields. Solid curves are two-body model fits to the number and temperature evolutions simultaneously to extract the loss coefficient β for each d.

6.3 The dipolar collisions

To measure the effects of the dipolar interaction on the molecular loss, we follow the same sequence, as depicted in the last chapter, to prepare the molecules to the absolute ground state. During holding, the E-field is ramped to desired values in 15 to 40 μs, polarizing the molecules. Figure 6.7 shows the typical evolutions of the molecules with the presence of an E-field. With the molecular samples prepared at $\sim$ 350 nK, the initial molecule number is about 5×10^3 with density of $3 \times 10^{11}\text{cm}^{-3}$. To reduce the temperature effect as discussed in the last chapter, we limit the longest holding time to 20 ms, where the temperature increasing is not so severe and we regard β as a constant during the measurements.

As discussed above, d-wave scatterings should also contribute to the collisional processes. With distinct dependence on collision energy, the anti-evaporation effect through d-wave scatterings should be distinct from that of s-wave. What's

more, due to the anisotropic property of d-wave scattering, the temperature evolution with the dipolar interaction should be angular dependent, similar to that observed in Ref. [50]. These influences make the temperature evolutions with the presence of an E-field much more complicated. However, in our experiments, no obvious anisotropic temperature evolution was observed within our temperature resolution. This may probably due to the cross-dimensional thermalization and our limited temperature sensitivity. Thus, for simplicity, we still assume thermal equilibrium is always reached within the three dimensions and use the two-body loss model (Eq. 5.5 and Eq. 5.6) to extract the loss coefficient β for each d, only replacing the $(1/4 + h_0)$ term in Eq. 5.6 by solely h_0 to account the overall anti-evolution effect.

The extracted β, as well as the corresponding average temperature during holding, with respect to d is shown in Fig. 6.8. The unitary loss limit for s-wave scattering, assuming unity loss possibility in the short range, following [195]

$$\beta_{0u}(T) = \frac{4\pi\hbar}{m}\langle\frac{1}{k}\rangle_T, \tag{6.7}$$

is also illustrated by the shadowed band. Here, $\langle 1/k\rangle_T$ is the thermal average of $1/k$ with k the collisional wave vector. As shown in Fig. 6.8, the loss coefficient β has already been greatly modified by the dipolar interaction within the accessible d and a step-wise dependence feature is observed. For $d < 0.2$ D, β is almost a constant as that without an E-field. Further increasing of d induces enhancement of the loss, followed by a flat plateau near the unitary limit for the s-wave scattering. Within the plateau, β changes little from 0.4 D to 0.5 D. Finally, the plateau is ended by another rapid raise.

In order to understand the step-wise feature of the dependence, we refer to the characteristic energies of s-wave and d-wave scatterings in Fig. 6.4 and Fig. 6.5. For $d < 0.5$ D, the d-wave barriers are too high for the 400 nK molecules to overcome. Thus, d-wave scatterings can be ignored and we attribute the loss in this range to solely s-wave scattering. As shown in Fig. 6.4, E_{s-wave} begins to

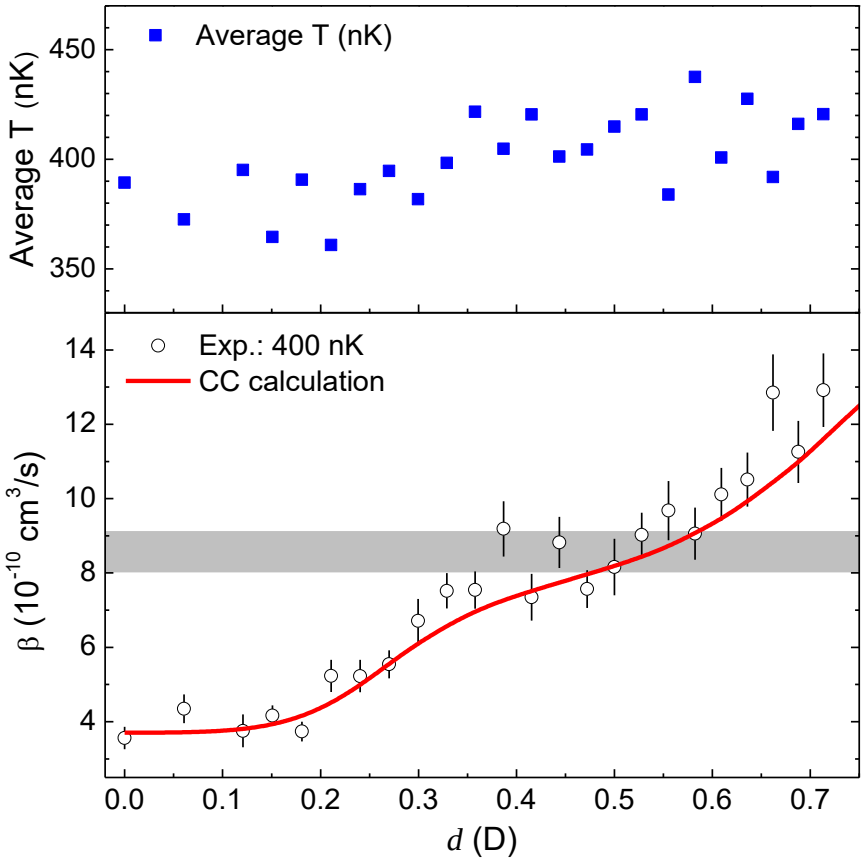

Figure 6.8: d dependence of the loss coefficient β with sample temperature of about 400 nK. Up-panel: the average sample temperature during the holding period. Despite the fluctuation, the average temperature increases with higher d, indicating more severe anti-evaporation. Lower-panel: the extracted β with different d, where step-wise feature is observed (see text). The solid curve is the CC calculation result for sample temperature of 400 nK based on the full "sticky" model without any free parameter. The shadowed region exhibits the unitary loss limit for s-wave scattering within the temperature range of 400 ± 50 nK (see text).

decrease at $\sim$ 0.2 D which is exactly the place where the first increasing of β happens. At the start point of the plateau with $d \approx 0.4$ D, E_{s-wave} reaches the value of the sample temperature, i.e. the s-wave unitary limit corresponds to E_{s-wave} being comparable and even lower to the temperature. At about 0.55 D, the barrier heights of the $|L = 2, |M_L| = 1\rangle$ channels become comparable to the sample temperature and the second raise of β emerges. Thus, we attribute the

molecular loss at $d > 0.5$ D to a unitarity limited s-wave scattering in addition to the d-wave scatterings. In this case, the contributions of s-wave and d-wave scatterings can be individually separated, i.e. solely attributing the loss to s-wave for $d < 0.5$ D and extracting d-wave collisions by subtracting s-wave unitary limit from the measured β for $d > 0.5$ D, as demonstrated in Fig. 6.9.

For a more quantitative understanding, Goulven has carried out the CC calculation for the dipolar collisions with partial waves up to $L = 8$. In the calculation, experimentally measured permanent electric dipole moment of 3.2 D and the rotational constant $B_v = 0.0697$ cm^{-1} are used. The calculated results are shown as solid curves in Fig. 6.8 the total contributions as well as the separated contributions of the partial waves in Fig. 6.9. Without any fitting parameter, the theoretical predictions already reach impressive agreement with the experimental data for both the total values and the separated ones. As illustrated in the inset of Fig. 6.9, the main contribution of the d-wave scatterings comes from the $|M_L| = 1$ channels while the other channels can be ignored, which is consistent with our qualitative analysis based on the adiabatic potentials for the d-wave channels.

6.4 Temperature dependence of the dipolar collisions

In the Wigner regime, the dependence of the loss coefficient β on the effective dipole moment d should follow the universal relation $\beta \propto d^{4(L+1/2)}$ [195, 214, 216], which has been observed for the p-wave collisions in the ^{40}K^{87}Rb system [50]. However, as discussed in the last chapter, our samples have not yet enter the Wigner regime although we have the comparable temperature as that in the ^{40}K^{87}Rb experiment. Indeed, fitting to the experimental data in Fig. 6.9(a) and Fig. 6.9(b) with power-law function gives $\beta \propto d^{1.3(0.6)}$ for s-wave and $\beta \propto d^{5.4(2.1)}$ for d-wave, where the numbers in the parentheses are the fits errors. These power

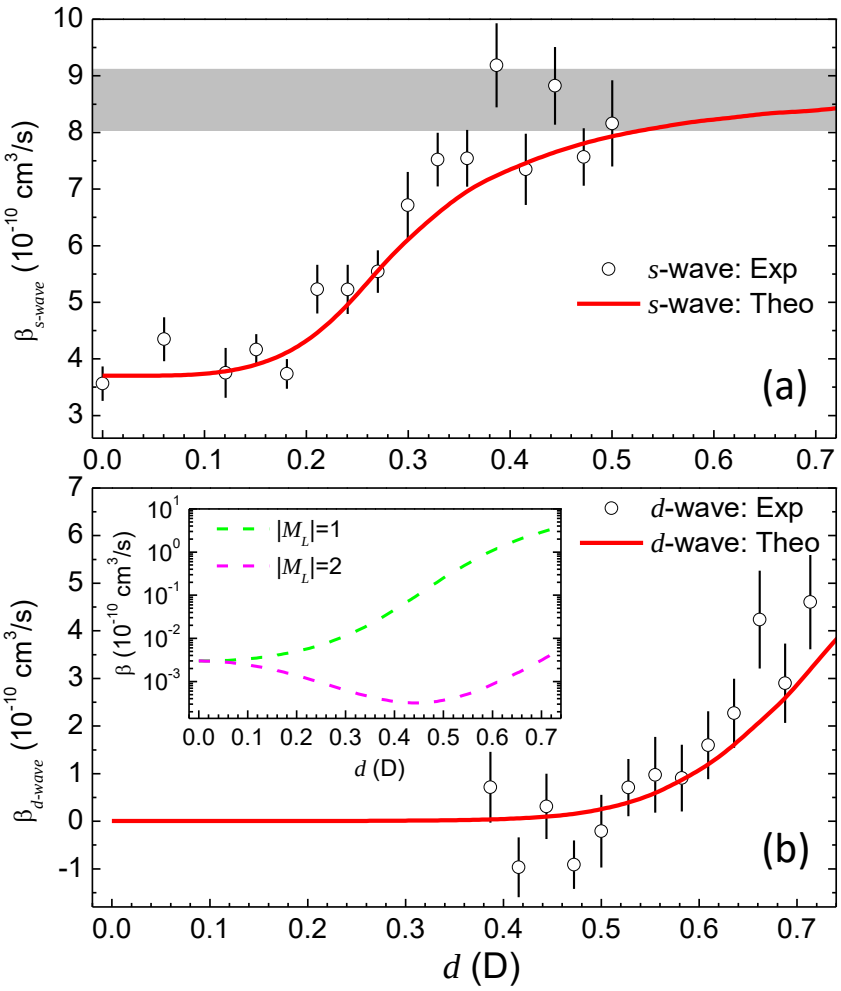

Figure 6.9: The separated contributions of s-wave and d-wave scatterings to the molecular loss. Black circles are extracted from experimental data (see text) while the solid curves are the theoretical results. The inset shows the calculated values of the two d-wave channels in the log scale. It validates that the $|M_L| = 2$ scatterings can be neglected. As the contributions of the $|L = 0, |M_L| = 0\rangle$ and the $|2, 0\rangle$ channels are not separated in the theoretical calculation, the red curve in (a) actually includes both channels while the one in (b) is the sum of all the d-wave channels except for the $|2, 0\rangle$ one. However, by mapping to the loss rate of the $|2, 1\rangle$ channel with the same barrier height, the contribution of the $|2, 0\rangle$ collision with the largest d is only $\sim 7 \times 10^{-12}$ cm^3/s. Thus, it has ignorable effect within our experimental range and we can approximately regard the red curves in (a) and (b) as s-wave and d-wave contributions respectively.

indexes greatly deviate from the Wigner law predicted values of 2 and 10 respectively, which indicates non universal behaviors with our present experimental condition.

In order to figure out the effects of sample temperature on the dipolar collisions, we measured the d dependence of β at three different sets of temperatures, as shown in Fig. 6.10. For the three cases, the dependences on d are all stepwise featured, but the plateau is less obvious for higher temperatures. Although at small $d < 0.2$ D, β for the three temperatures are quite different, the start points of the first rise are almost the same near 0.2 D. It is consistent with the argument of the competing between the van der Waals interaction and the dipolar interaction, and thus independent from the sample temperature. However, for higher sample temperature, the unitary limit is lower and s-wave scattering saturates at smaller d, which is also agree with the qualitative discussion that the unitary limit is reached near the point where E_{s-wave} starts to be smaller than the temperature. On the other hand, higher temperature enables colliding molecules to overcome the d-wave barriers easier, resulting in more significant d-wave collisions. For the case of 1400 nK temperature, with the largest achieved d, the loss rate through d-wave scattering is even larger than that via the s-wave channel.

For all the three temperature cases, the calculation results with the CC method have reached significant consistence with the experimental data. This excellent agreement together with the non-obvious oscillation of the d dependent loss rates [217] validates the assumption of near unity, if not unity, loss possibility in short range. It also supports that using the simple two-body model to extract the loss coefficients β is effective although the complex-mediated collisions are ignored. Thus, if it is the "sticky" mechanism causing the molecular loss, the post complex-forming collisions should have little effect on the molecular dynamics, i.e. the complex almost escape directly upon its formation. However, on the other hand, although both the non-dipolar and dipolar collisions do not deviate

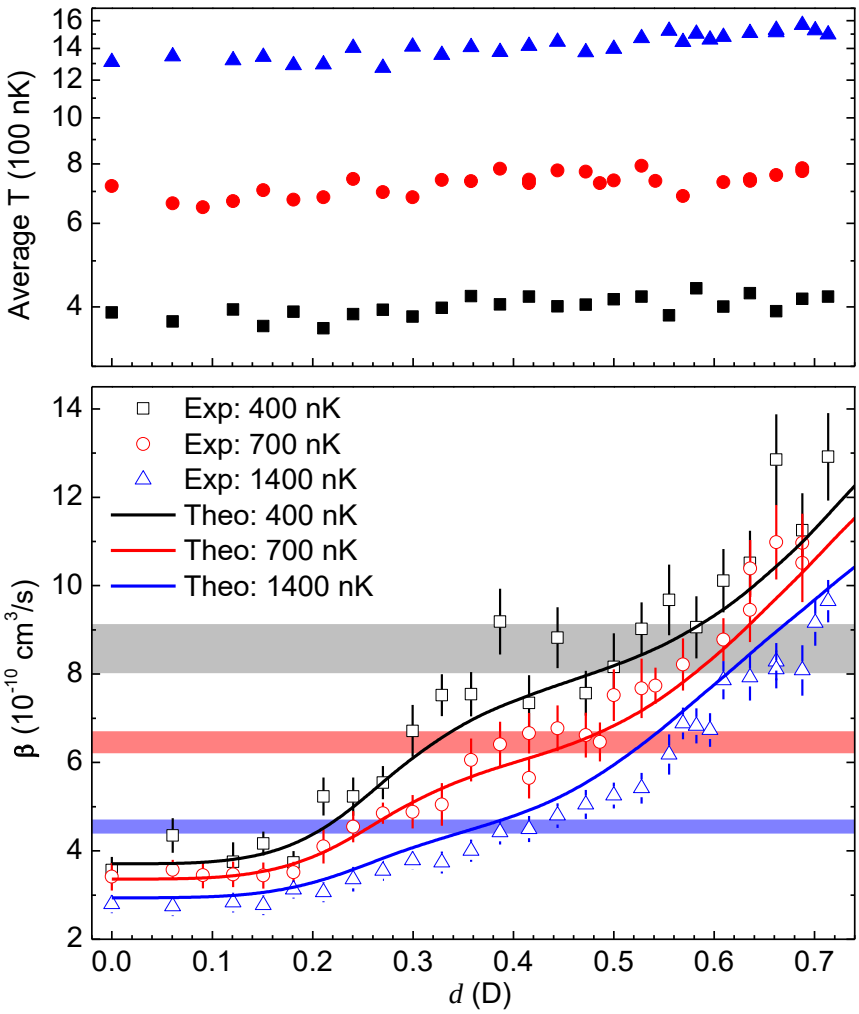

Figure 6.10: Temperature dependence of the loss coefficients for the dipolar collisions. Lower panel: β as a function of d with three sets of average temperatures of 400 nK, 700 nK and 1400 nK. The solid curves are the CC calculation results for the corresponding sample temperatures. The colored bands indicate the s-wave unitary loss rates with temperature ranges of 400 ± 50 nK, 700 ± 50 nK and 1400 ± 100 nK. Up panel illustrates the average sample temperatures for the three sets of data respectively.

from the "sticky" model with this or that assumptions, it is still not decisive to claim its responsibility to the loss. Any mechanism that induces unity loss in short range could results in similar behaviors. Thus, more investigations on the molecular collisions, the complex properties, and even the direct detection of the

complex are still indispensable.

In this chapter, I have demonstrated our investigations on the ultracold molecular collisions with the presence of the dipole-dipole interaction. With moderate E-fields, the molecular loss is greatly modified and step-wise feature is observed. The couplings between the even partial waves, induced by the dipolar interaction, lowered the s-wave potential and d-wave barriers, resulting in the increasing of the s-wave collisional rate until reaching the unitary limit and the non ignorable d-wave scatterings. What's more, the investigations on the temperature dependence of the dipolar collisions also indicate the effects of the collision energy on the barrier-less s-wave scattering and the d-wave collisions in the non Wigner regime. More quantitatively, the excellent agreement between the theoretical calculation based on the full "sticky" model and our experimental result validates the assumption of near unity loss possibility of the colliding molecules in short range.

□ End of chapter.

Chapter 7

Conclusion and Outlook

7.1 Conclusion

In this thesis, I have demonstrated our successful creation of ultracold samples of the dipolar $^{23}Na^{87}Rb$ molecules in their singlet ground state and investigations on the properties of these molecules especially their collisional dynamics. After identifying a suitable intermediate state bridging the Feshbach state and the singlet rovibrational ground state, the weakly-bound Feshbach molecules are successfully transferred to the absolute ground state with efficiency up to 93% through a STIRAP. Combining the two-photon Raman process with extra microwave fields, full control over the molecular internal states, including their vibrational, rotational and hyperfine degrees of freedom, are achieved. Typically, the created molecular samples have about 1.5×10^4 molecules in a well defined internal state with a temperature of about 700 nK and peak density of $6 \times 10^{11} \mathrm{cm}^{-3}$. Once the ground state molecules are produced, basic properties including their polarizability to the ODT and the permanent electric dipole moment are characterized. In order to figure out the loss mechanism of the chemically stable molecules, we investigate the molecular dynamics with or without the chemical reactivity. It turns out that regardless of the chemical reactivity, the molecules undergo comparable loss and similar dependence on the sample temperature. Furthermore, the dipolar nature of the $^{23}Na^{87}Rb$ molecules are also studied by applying a static E-field.

The induced dipolar interaction greatly modifies the molecular loss and results in significance contributions from both s-wave and d-wave scatterings even in the ultracold regime.

7.2 Outlook

Since the first creation of the ultracold dipolar KRb molecules in 2008, the research area has been developing rapidly and more molecular species have become available. However, many properties of the molecules are still unknown, especially the loss mechanism of the chemically stable molecules. This thesis focuses on the generation and characterization of a new bosonic species of ^{23}Na^{87}Rb molecules with the largest static effective dipole moment ever achieved. With the well controlled internal state and the strong dipolar interaction, I am sure the further investigations on the dipolar ^{23}Na^{87}Rb molecules will shine new lights on the fundamental properties of ultracold molecules as well as novel applications of achieving degenerate molecular samples and realizing strongly correlated many-body systems.

7.2.1 Figuring out the loss mechanism

At present, the loss mechanism of the chemically stable molecules is still not determined. Although our investigations on the molecular collisions with controlled chemical reactivities and the dipolar collisions do not deviate from the proposed "sticky" model, these results are not decisive. The strongest support to the loss mechanism is the direct observation of the products, i.e. the four-atom complex.

Due to the barely known properties of the products, it is a great challenge to directly detect them. In this case, the side-proved evidences are also of great importance. The full "sticky" model is based on the assumptions of the large density of states and the ergodicity that the four-body complex goes over all these states. However, the indistinguishability, or the no observation of the resonances

prevents us to verify the assumptions. While, on the other hand, the density of states of the ^{87}Rb +^{23}Na^{87}Rb system, which is also chemically stable, is estimated to have only several resonances per microkelvin [202], which is about thousand times lower than that between two ^{23}Na^{87}Rb molecules. Thus, the resonances in the ^{87}Rb +^{23}Na^{87}Rb system should be resolvable according to the estimation. Moreover, the distribution of these resonances should also give information on the property of ergodicity, which should induce quantum chaotic collisions and the Wigner-Dyson distribution of the resonances [218, 219]. Thus, the collisions between the ^{87}Rb atom and the ground-state ^{23}Na^{87}Rb molecules are also of great interest.

In the discussion of the non observation of the post complex-forming collisions, we suspect direct complex loss once formed which may results from the non-trappable property of the complex by the ODT, photon excitation by the trap light, and the fast collision rate between the complexes. To check these suspicions, we can trap the molecules in the first excited rotational state, which is also chemically stable, by a static electric gradient trap, which is free from any laser irradiations. Besides, with the technique of optical tweezer, the number of the molecules proceed to collide can be controlled, i.e. we can manipulate only two molecules to collide in order to rule out the effects of the other molecules and complexes. With these techniques, we can obtain more insight understanding on the dynamics and investigate the molecular collisions in a better controlled manner.

7.2.2 Obtaining colder molecular samples

One direct ambition for future works is further cooling the dipolar molecules down to quantum degeneracy. However, the unexpected severe molecular loss prevents efficient evaporative cooling for the ground-state ^{23}Na^{87}Rb molecules. Thus, it is necessary to suppress the loss in order to achieve colder and degenerate molecular samples. As the loss happens when the colliding molecules enter the short range,

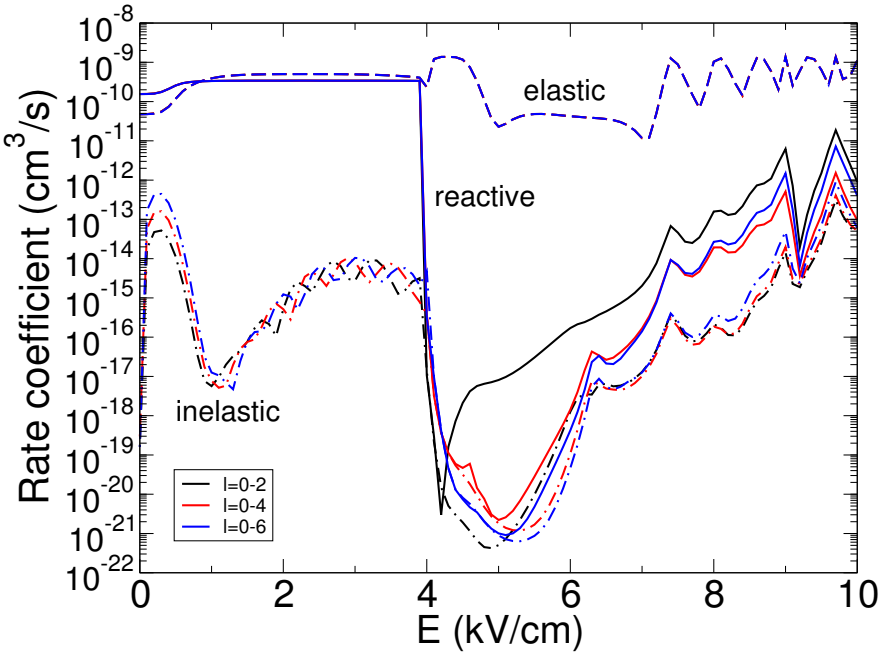

Figure 7.1: The ratio between the elastic and the inelastic collision rate of the $|J = 1, M_J = 0\rangle$ molecules as a function of the E-field. Here, the label "reactive" denotes the rate coefficients for complex forming. This figure is from Goulven (private communication).

the loss can be suppressed by engineering a long-range barrier while the elastic collisions are still favorable through the dipolar interaction.

Based on the full "sticky" model, Goulven et al. have proposed a scheme to achieve favorable ratio between the elastic and the inelastic collision rate by preparing the molecules to the first excited rotational state $|J = 1, M_J = 0\rangle$ [209, 220, 221, 222], as shown in Fig. 7.1 the case for ^{23}Na^{87}Rb molecules. At an E-field of about 4 kV/cm, there is a steep decreasing of the complex-forming rate, giving impressive ratio between the elastic and the inelastic collisions. The E-field, where the steep jump happens, just corresponds to the position where the energy of two $|J = 1, M_J = 0\rangle$ molecules equals to that of a molecular pair of one $|J = 0, M_J = 0\rangle$ and one $|J = 2, M_J = 0\rangle$ molecule. The anti-crossing between the two potentials induces an effective barrier on the potential between two $|J = 1, M_J = 0\rangle$ molecules, which results in the suppression of the complex-

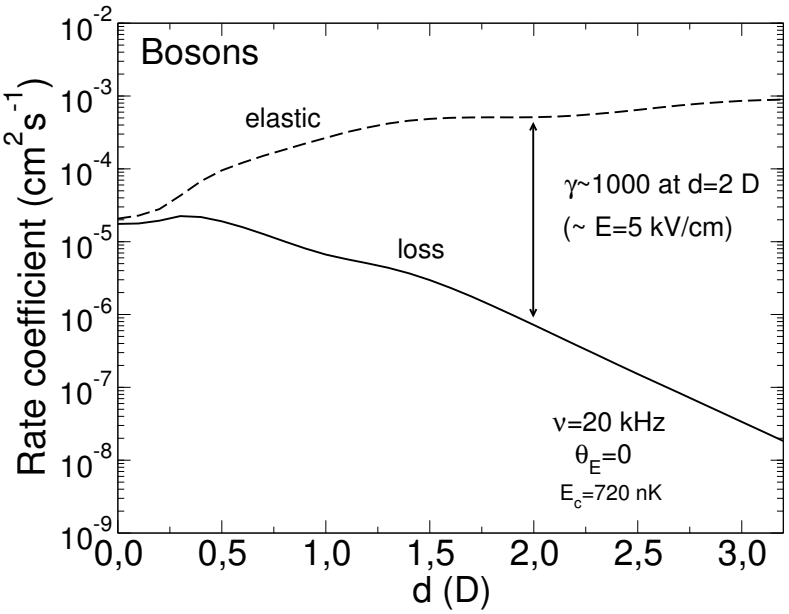

Figure 7.2: The rate coefficients for a 2D sample of the absolute ground-state ^{23}Na^{87}Rb molecules as a function of the effective dipole moment d. The calculation is done with a $2\pi \times 20$ kHz trap frequency along the tight confinement and a collision energy of 720 nK. The graph is provided by Goulven (private communication).

forming rate. Although a 4 kV/cm E-field is still not feasible with our present setup, the E-field can be easily achieved by placing the electrodes inside the vacuum chamber. At that time, the much faster elastic collisions than the inelastic scatterings should lead to efficient evaporative cooling of the molecules.

Moreover, the suppression of the molecular loss can also be accomplished by utilizing the anisotropic property of the dipolar interaction. As the dipolar interaction is purely repulsive with the side-by-side configuration, an effective barrier between the two molecules is induced within a 2D molecular sample with an E-field perpendicular to the 2D plane [223, 224, 225]. The suppression of the molecular loss in a 2D sample has already been observed in KRb molecules but with insufficient ratio between the elastic and the inelastic collisions [85]. Figure 7.2 illustrates the calculated rate coefficients for the elastic and the in-

elastic collisions of a 2D sample of ground-state $^{23}Na^{87}Rb$ molecules, which can be realized by imposing an 1D optical lattice along the direction of the E-field. With an effective dipole moment of 2 D, the ratio between the elastic and the inelastic collisions has reached to 1000, which should be enough to support efficient evaporative cooling. However, the required E-field is still out of our present accessibility.

On the other hand, the dipolar interaction induced by microwave dressing was also proposed to be an efficient method to engineer the interaction potential between two molecules [159, 179] as well as suppressing the inelastic collisions [180]. Thanks to the large permanent electric dipole moment of the ground-state $^{23}Na^{87}Rb$ molecules, it is easy to achieve strong couplings between the microwave field and the molecules. Even with our microwave source placed 20 cm away from the molecular sample, we can reach up to $2\pi \times 100$ kHz Rabi frequencies with 1 W microwave power. By combining the microwave fields and the E-field, it is possible to realize efficient evaporative cooling of the molecules even with our currently accessible E-fields [159].

7.2.3 Molecular samples in an optical lattice

Another promising direction is loading the molecules into an optical lattice. On one hand, with each lattice site occupied by only one molecule, each molecule is isolated from the other molecules, thus eliminating the molecular loss. On the other hand, the molecules can be effectively interacted through the long-range dipolar interaction, inducing strong correlations within the molecules in different sites. Although the quantum magnetism with the XX form (spin-exchange) Hamiltonian has already been observed in the KRb system [54, 55], other unstudied magnetism such as the XXZ Hamiltonian is also of great interest. The novel Hamiltonian can be realized by combining microwave dressings with a static E-field. By changing the E-field, the competing between the spin-exchange term and the Ising term can be mutually tuned, and the phase transition between the

two regime can be investigated in a controlled manner [70, 226]. Furthermore, as the dipolar interaction through microwave dressing can couple the molecular internal angular momentum and the external spatial angular momentum, spin-orbital coupling between the lattice-confined molecules can be intrinsically induced without coupling to an excited state as that in atomic systems [227]. Besides, there are also many other proposals to realizing novel quantum phases with lattice-confined dipolar molecules, such as the supersolid state [39, 40, 41] and the fractional Chern insulators [228].

Up to now, there are just two heteronuclear species of the ^{40}K^{87}Rb [91, 92] and ^{87}Rb^{133}Cs [93] molecules are successfully loaded into optical lattices, where the lattice loadings are realized at the stage of the atomic mixtures. For both cases, the filling factors are limited to about 30% due to the different statistics of ^{40}K and ^{87}Rb atoms and the unfavorable scattering length in ^{87}Rb^{133}Cs system. However, these problems are intrinsically avoided in our system. In principle, high lattice filling fraction with each site containing one ^{23}Na and ^{87}Rb atom can be achieved by loading from a well overlapped double BECs of the two atomic species. Furthermore, with two atoms possessing a single lattice site, the conversion efficiency from the atomic pairs to the Feshbach molecules can reach near unity [91], much larger than the 7% in our present bulk samples. Thus, with this method, we can obtain samples of low entropy with large number of molecules.

□ End of chapter.

Bibliography

[1] David J Wineland, Robert E Drullinger, and Fred L Walls. Radiation-pressure cooling of bound resonant absorbers. *Physical Review Letters*, 40(25):1639, 1978.

[2] Paul D Lett, Richard N Watts, Christoph I Westbrook, William D Phillips, Phillip L Gould, and Harold J Metcalf. Observation of atoms laser cooled below the Doppler limit. *Physical Review Letters*, 61(2):169, 1988.

[3] Wolfgang Ketterle and NJ Van Druten. Evaporative cooling of trapped atoms. *Advances in Atomic, Molecular, and Optical physics*, 37:181–236, 1996.

[4] Mike H Anderson, Jason R Ensher, Michael R Matthews, Carl E Wieman, and Eric A Cornell. Observation of Bose-Einstein condensation in a dilute atomic vapor. *Science*, 269(5221):198, 1995.

[5] Kendall B Davis, M-O Mewes, Michael R Andrews, NJ Van Druten, DS Durfee, DM Kurn, and Wolfgang Ketterle. Bose-Einstein condensation in a gas of Sodium atoms. *Physical Review Letters*, 75(22):3969, 1995.

[6] Cl C Bradley, CA Sackett, JJ Tollett, and Randall G Hulet. Evidence of Bose-Einstein condensation in an atomic gas with attractive interactions. *Physical Review Letters*, 75(9):1687, 1995.

[7] Brian DeMarco and Deborah S Jin. Onset of Fermi degeneracy in a trapped atomic gas. *Science*, 285(5434):1703–1706, 1999.

[8] Rana X Adhikari. Gravitational radiation detection with laser interferometry. *Reviews of Modern Physics*, 86(1):121, 2014.

[9] Andrew D Ludlow, Martin M Boyd, Jun Ye, Ekkehard Peik, and Piet O Schmidt. Optical atomic clocks. *Reviews of Modern Physics*, 87(2):637, 2015.

[10] Maciej Lewenstein, Anna Sanpera, Veronica Ahufinger, Bogdan Damski, Aditi Sen, and Ujjwal Sen. Ultracold atomic gases in optical lattices: mimicking condensed matter physics and beyond. *Advances in Physics*, 56(2):243–379, 2007.

[11] Immanuel Bloch, Jean Dalibard, and Sylvain Nascimbene. Quantum simulations with ultracold quantum gases. *Nature Physics*, 8(4):267–276, 2012.

[12] Dieter Jaksch and Peter Zoller. The cold atom Hubbard toolbox. *Annals of physics*, 315(1):52–79, 2005.

[13] S Inouye, MR Andrews, J Stenger, H-J Miesner, DM Stamper-Kurn, and W Ketterle. Observation of Feshbach resonances in a Bose–Einstein condensate. *Nature*, 392(6672):151–154, 1998.

[14] Cheng Chin, Rudolf Grimm, Paul Julienne, and Eite Tiesinga. Feshbach resonances in ultracold gases. *Reviews of Modern Physics*, 82(2):1225, 2010.

[15] Thomas Bourdel, Lev Khaykovich, Julien Cubizolles, Jun Zhang, Frédéric Chevy, M Teichmann, L Tarruell, SJJMF Kokkelmans, and Christophe Salomon. Experimental study of the BEC-BCS crossover region in lithium 6. *Physical Review Letters*, 93(5):050401, 2004.

[16] M Bartenstein, A Altmeyer, S Riedl, S Jochim, C Chin, J Hecker Denschlag, and R Grimm. Crossover from a molecular Bose-Einstein condensate to a degenerate Fermi gas. *Physical Review Letters*, 92(12):120401, 2004.

[17] T Kraemer, M Mark, P Waldburger, JG Danzl, C Chin, B Engeser, AD Lange, K Pilch, A Jaakkola, H-C Nägerl, et al. Evidence for Efimov quantum states in an ultracold gas of Caesium atoms. *Nature*, 440(7082):315–318, 2006.

[18] Scott E Pollack, Daniel Dries, and Randall G Hulet. Universality in three- and four-body bound states of ultracold atoms. *Science*, 326(5960):1683–1685, 2009.

[19] Matteo Zaccanti, Benjamin Deissler, Chiara DErrico, Marco Fattori, Mattia Jona-Lasinio, Stefan Müller, Giacomo Roati, Massimo Inguscio, and Giovanni Modugno. Observation of an Efimov spectrum in an atomic system. *Nature Physics*, 5(8):586–591, 2009.

[20] Elizabeth A Donley, Neil R Claussen, Sarah T Thompson, and Carl E Wieman. Atom–molecule coherence in a Bose–Einstein condensate. *Nature*, 417(6888):529–533, 2002.

[21] Selim Jochim, Markus Bartenstein, Alexander Altmeyer, Gerhard Hendl, Stefan Riedl, Cheng Chin, J Hecker Denschlag, and Rudolf Grimm. Bose-Einstein condensation of molecules. *Science*, 302(5653):2101–2103, 2003.

[22] Markus Greiner, Cindy A Regal, and Deborah S Jin. Emergence of a molecular Bose–Einstein condensate from a Fermi gas. *Nature*, 426(6966):537–540, 2003.

[23] Thorsten Köhler, Krzysztof Góral, and Paul S Julienne. Production of cold molecules via magnetically tunable Feshbach resonances. *Reviews of Modern Physics*, 78(4):1311, 2006.

[24] Markus Greiner, Olaf Mandel, Tilman Esslinger, Theodor W Hänsch, and Immanuel Bloch. Quantum phase transition from a superfluid to a Mott insulator in a gas of ultracold atoms. *Nature*, 415(6867):39–44, 2002.

[25] Thilo Stöferle, Henning Moritz, Christian Schori, Michael Köhl, and Tilman Esslinger. Transition from a strongly interacting 1D superfluid to a Mott insulator. *Physical Review Letters*, 92(13):130403, 2004.

[26] Waseem S Bakr, Jonathon I Gillen, Amy Peng, Simon Fölling, and Markus Greiner. A quantum gas microscope for detecting single atoms in a Hubbard-regime optical lattice. *Nature*, 462(7269):74–77, 2009.

[27] Jacob F Sherson, Christof Weitenberg, Manuel Endres, Marc Cheneau, Immanuel Bloch, and Stefan Kuhr. Single-atom-resolved fluorescence imaging of an atomic Mott insulator. *Nature*, 467(7311):68–72, 2010.

[28] Elmar Haller, James Hudson, Andrew Kelly, Dylan A Cotta, Bruno Peaudecerf, Graham D Bruce, and Stefan Kuhr. Single-atom imaging of fermions in a quantum-gas microscope. *Nature Physics*, 11(9):738–742, 2015.

[29] Lawrence W Cheuk, Matthew A Nichols, Melih Okan, Thomas Gersdorf, Vinay V Ramasesh, Waseem S Bakr, Thomas Lompe, and Martin W Zwierlein. Quantum-gas microscope for fermionic atoms. *Physical Review Letters*, 114(19):193001, 2015.

[30] Maxwell F Parsons, Florian Huber, Anton Mazurenko, Christie S Chiu, Widagdo Setiawan, Katherine Wooley-Brown, Sebastian Blatt, and Markus Greiner. Site-resolved imaging of fermionic ^{6}Li in an optical lattice. *Physical Review Letters*, 114(21):213002, 2015.

[31] Jonathan Simon, Waseem S Bakr, Ruichao Ma, M Eric Tai, Philipp M Preiss, and Markus Greiner. Quantum simulation of antiferromagnetic spin chains in an optical lattice. *Nature*, 472(7343):307–312, 2011.

[32] Daniel Greif, Thomas Uehlinger, Gregor Jotzu, Leticia Tarruell, and Tilman Esslinger. Short-range quantum magnetism of ultracold fermions in an optical lattice. *Science*, 340(6138):1307–1310, 2013.

[33] Anton Mazurenko, Christie S Chiu, Geoffrey Ji, Maxwell F Parsons, Márton Kanász-Nagy, Richard Schmidt, Fabian Grusdt, Eugene Demler, Daniel Greif, and Markus Greiner. A cold-atom Fermi–Hubbard antiferromagnet. *Nature*, 545(7655):462–466, 2017.

[34] Tsin D Lee, Kerson Huang, and Chen N Yang. Eigenvalues and eigenfunctions of a Bose system of hard spheres and its low-temperature properties. *Physical Review*, 106(6):1135, 1957.

[35] Thierry Lahaye, C Menotti, L Santos, M Lewenstein, and T Pfau. The physics of dipolar bosonic quantum gases. *Reports on Progress in Physics*, 72(12):126401, 2009.

[36] MA Baranov, M Dalmonte, G Pupillo, and Peter Zoller. Condensed matter theory of dipolar quantum gases. *Chemical Reviews*, 112(9):5012–5061, 2012.

[37] Lincoln D Carr, David DeMille, Roman V Krems, and Jun Ye. Cold and ultracold molecules: science, technology and applications. *New Journal of Physics*, 11(5):055049, 2009.

[38] Christian Trefzger, C Menotti, B Capogrosso-Sansone, and M Lewenstein. Ultracold dipolar gases in optical lattices. *Journal of Physics B: Atomic, Molecular and Optical Physics*, 44(19):193001, 2011.

[39] Krzysztof Góral, Luis Santos, and Maciej Lewenstein. Quantum phases of dipolar bosons in optical lattices. *Physical Review Letters*, 88(17):170406, 2002.

[40] S Yi, T Li, and CP Sun. Novel quantum phases of dipolar Bose gases in optical lattices. *Physical Review Letters*, 98(26):260405, 2007.

[41] B Capogrosso-Sansone, C Trefzger, M Lewenstein, P Zoller, and G Pupillo. Quantum phases of cold polar molecules in 2D optical lattices. *Physical Review Letters*, 104(12):125301, 2010.

[42] Tobias Koch, Thierry Lahaye, Jonas Metz, Bernd Fröhlich, Axel Griesmaier, and Tilman Pfau. Stabilization of a purely dipolar quantum gas against collapse. *Nature Physics*, 4(3):218–222, 2008.

[43] Thierry Lahaye, Jonas Metz, Bernd Froehlich, Tobias Koch, Maximilian Meister, Axel Griesmaier, Tilman Pfau, Hiroki Saito, Yuki Kawaguchi, and Masahito Ueda. D-wave collapse and explosion of a dipolar Bose-Einstein condensate. *Physical Review Letters*, 101(8):080401, 2008.

[44] K Aikawa, S Baier, A Frisch, M Mark, C Ravensbergen, and F Ferlaino. Observation of Fermi surface deformation in a dipolar quantum gas. *Science*, 345(6203):1484–1487, 2014.

[45] Thierry Lahaye, Tobias Koch, Bernd Fröhlich, Marco Fattori, Jonas Metz, Axel Griesmaier, Stefano Giovanazzi, and Tilman Pfau. Strong dipolar effects in a quantum ferrofluid. *Nature*, 448(7154):672–675, 2007.

[46] K Aikawa, A Frisch, M Mark, S Baier, R Grimm, JL Bohn, DS Jin, GM Bruun, and F Ferlaino. Anisotropic relaxation dynamics in a dipolar fermi gas driven out of equilibrium. *Physical Review Letters*, 113(26):263201, 2014.

[47] Nathaniel Q Burdick, Andrew G Sykes, Yijun Tang, and Benjamin L Lev. Anisotropic collisions of dipolar Bose–Einstein condensates in the universal regime. *New Journal of Physics*, 18(11):113004, 2016.

[48] Yijun Tang, Andrew G Sykes, Nathaniel Q Burdick, Jack M DiSciacca, Dmitry S Petrov, and Benjamin L Lev. Anisotropic expansion of a thermal dipolar Bose gas. *Physical Review Letters*, 117(15):155301, 2016.

[49] Yijun Tang, Wil Kao, Kuan-Yu Li, Sangwon Seo, Krishnanand Mallayya, Marcos Rigol, Sarang Gopalakrishnan, and Benjamin L Lev. Thermalization near integrability in a dipolar quantum Newton's cradle. *ArXiv:1707.07031*, 2017.

[50] KK Ni, S Ospelkaus, D Wang, G Quéméner, B Neyenhuis, MH de Miranda, JL Bohn, J Ye, and DS Jin. Dipolar collisions of polar molecules in the quantum regime. *Nature*, 464(7293):1324, 2010.

[51] Ryan Barnett, Dmitry Petrov, Mikhail Lukin, and Eugene Demler. Quantum magnetism with multicomponent dipolar molecules in an optical lattice. *Physical Review Letters*, 96(19):190401, 2006.

[52] Alexey V Gorshkov, Salvatore R Manmana, Gang Chen, Jun Ye, Eugene Demler, Mikhail D Lukin, and Ana Maria Rey. Tunable superfluidity and quantum magnetism with ultracold polar molecules. *Physical Review Letters*, 107(11):115301, 2011.

[53] Alexey V Gorshkov, Salvatore R Manmana, Gang Chen, Eugene Demler, Mikhail D Lukin, and Ana Maria Rey. Quantum magnetism with polar alkali-metal dimers. *Physical Review A*, 84(3):033619, 2011.

[54] Bo Yan, Steven A Moses, Bryce Gadway, Jacob P Covey, Kaden RA Hazzard, Ana Maria Rey, Deborah S Jin, and Jun Ye. Observation of dipolar spin-exchange interactions with lattice-confined polar molecules. *Nature*, 501(7468):521–525, 2013.

[55] Kaden RA Hazzard, Bryce Gadway, Michael Foss-Feig, Bo Yan, Steven A Moses, Jacob P Covey, Norman Y Yao, Mikhail D Lukin, Jun Ye, Deborah S Jin, et al. Many-body dynamics of dipolar molecules in an optical lattice. *Physical Review Letters*, 113(19):195302, 2014.

[56] Simon Baier, MJ Mark, Daniel Petter, Kiyotaka Aikawa, Lauriane Chomaz, Zi Cai, M Baranov, P Zoller, and F Ferlaino. Extended Bose-Hubbard models with ultracold magnetic atoms. *Science*, 352(6282):201–205, 2016.

[57] Holger Kadau, Matthias Schmitt, Matthias Wenzel, Clarissa Wink, Thomas Maier, Igor Ferrier-Barbut, and Tilman Pfau. Observing the Rosensweig instability of a quantum ferrofluid. *Nature*, 530(7589):194–197, 2016.

[58] Igor Ferrier-Barbut, Holger Kadau, Matthias Schmitt, Matthias Wenzel, and Tilman Pfau. Observation of quantum droplets in a strongly dipolar Bose gas. *Physical Review Letters*, 116(21):215301, 2016.

[59] L Chomaz, S Baier, D Petter, MJ Mark, F Wächtler, L Santos, and F Ferlaino. Quantum-Fluctuation-Driven Crossover from a Dilute Bose-Einstein Condensate to a Macrodroplet in a Dipolar Quantum Fluid. *Physical Review X*, 6(4):041039, 2016.

[60] Matthias Schmitt, Matthias Wenzel, Fabian Böttcher, Igor Ferrier-Barbut, and Tilman Pfau. Self-bound droplets of a dilute magnetic quantum liquid. *Nature*, 539(7628):259–262, 2016.

[61] Albert Frisch, Michael Mark, Kiyotaka Aikawa, Francesca Ferlaino, John L Bohn, Constantinos Makrides, Alexander Petrov, and Svetlana Kotochigova. Quantum chaos in ultracold collisions of gas-phase erbium atoms. *Nature*, 507(7493):475–479, 2014.

[62] Kristian Baumann, Nathaniel Q Burdick, Mingwu Lu, and Benjamin L Lev. Observation of low-field Fano-Feshbach resonances in ultracold gases of dysprosium. *Physical Review A*, 89(2):020701, 2014.

[63] T Maier, H Kadau, M Schmitt, M Wenzel, I Ferrier-Barbut, T Pfau, Albert Frisch, Simon Baier, Kiyotaka Aikawa, Lauriane Chomaz, et al. Emer-

gence of chaotic scattering in ultracold Er and Dy. *Physical Review X*, 5(4):041029, 2015.

[64] Axel Griesmaier, Jörg Werner, Sven Hensler, Jürgen Stuhler, and Tilman Pfau. Bose-Einstein condensation of chromium. *Physical Review Letters*, 94(16):160401, 2005.

[65] Mingwu Lu, Nathaniel Q Burdick, Seo Ho Youn, and Benjamin L Lev. Strongly dipolar Bose-Einstein condensate of dysprosium. *Physical Review Letters*, 107(19):190401, 2011.

[66] K Aikawa, A Frisch, M Mark, S Baier, A Rietzler, R Grimm, and F Ferlaino. Bose-Einstein condensation of erbium. *Physical Review Letters*, 108(21):210401, 2012.

[67] K Aikawa, A Frisch, M Mark, S Baier, R Grimm, and F Ferlaino. Reaching Fermi degeneracy via universal dipolar scattering. *Physical Review Letters*, 112(1):010404, 2014.

[68] Mark Saffman, Thad G Walker, and Klaus Mølmer. Quantum information with Rydberg atoms. *Reviews of Modern Physics*, 82(3):2313, 2010.

[69] K-K Ni, S Ospelkaus, MHG De Miranda, A Pe'Er, B Neyenhuis, JJ Zirbel, S Kotochigova, PS Julienne, DS Jin, and Jun Ye. A high phase-space-density gas of polar molecules. *Science*, 322(5899):231–235, 2008.

[70] Andrea Micheli, GK Brennen, and Peter Zoller. A toolbox for lattice-spin models with polar molecules. *Nature Physics*, 2(5):341–347, 2006.

[71] David DeMille. Quantum computation with trapped polar molecules. *Physical Review Letters*, 88(6):067901, 2002.

[72] SF Yelin, K Kirby, and Robin Côté. Schemes for robust quantum computation with polar molecules. *Physical Review A*, 74(5):050301, 2006.

[73] Jee Woo Park, Zoe Z Yan, Huanqian Loh, Sebastian A Will, and Martin W Zwierlein. Second-scale nuclear spin coherence time of ultracold $^{2}3Na^{4}0K$ molecules. *Science*, 357(6349):372–375, 2017.

[74] Roman V Krems. Cold controlled chemistry. *Physical Chemistry Chemical Physics*, 10(28):4079–4092, 2008.

[75] Goulven Quemener and Paul S Julienne. Ultracold molecules under control! *Chemical Reviews*, 112(9):4949–5011, 2012.

[76] ES Shuman, JF Barry, and D DeMille. Laser cooling of a diatomic molecule. *Nature*, 467(7317):820–823, 2010.

[77] Matthew T Hummon, Mark Yeo, Benjamin K Stuhl, Alejandra L Collopy, Yong Xia, and Jun Ye. 2D magneto-optical trapping of diatomic molecules. *Physical Review Letters*, 110(14):143001, 2013.

[78] JF Barry, DJ McCarron, EB Norrgard, MH Steinecker, and D DeMille. Magneto-optical trapping of a diatomic molecule. *Nature*, 512(7514):286, 2014.

[79] Jee Woo Park, Sebastian A Will, and Martin W Zwierlein. Ultracold dipolar gas of fermionic $^{23}Na^{40}K$ molecules in their absolute ground state. *Physical Review Letters*, 114(20):205302, 2015.

[80] Tetsu Takekoshi, Lukas Reichsöllner, Andreas Schindewolf, Jeremy M Hutson, C Ruth Le Sueur, Olivier Dulieu, Francesca Ferlaino, Rudolf Grimm, and Hanns-Christoph Nägerl. Ultracold dense samples of dipolar RbCs molecules in the rovibrational and hyperfine ground state. *Physical Review Letters*, 113(20):205301, 2014.

[81] Peter K Molony, Philip D Gregory, Zhonghua Ji, Bo Lu, Michael P Köppinger, C Ruth Le Sueur, Caroline L Blackley, Jeremy M Hutson, and

Simon L Cornish. Creation of Ultracold $^{87}Rb^{133}Cs$ Molecules in the Rovibrational Ground State. *Physical Review Letters*, 113(25):255301, 2014.

[82] Mingyang Guo, Bing Zhu, Bo Lu, Xin Ye, Fudong Wang, Romain Vexiau, Nadia Bouloufa-Maafa, Goulven Quéméner, Olivier Dulieu, and Dajun Wang. Creation of an Ultracold Gas of Ground-State Dipolar $^{23}Na^{87}Rb$ Molecules. *Physical Review Letters*, 116(20):205303, 2016.

[83] Timur M Rvachov, Hyungmok Son, Ariel T Sommer, Sepehr Ebadi, Juliana J Park, Martin W Zwierlein, Wolfgang Ketterle, and Alan O Jamison. Long-Lived Ultracold Molecules with Electric and Magnetic Dipole Moments. *Physical Review Letters*, 119(14):143001, 2017.

[84] S Ospelkaus, K-K Ni, D Wang, MHG De Miranda, B Neyenhuis, G Quéméner, PS Julienne, JL Bohn, DS Jin, and J Ye. Quantum-state controlled chemical reactions of ultracold potassium-rubidium molecules. *Science*, 327(5967):853–857, 2010.

[85] MHG De Miranda, A Chotia, B Neyenhuis, D Wang, G Quéméner, Silke Ospelkaus, JL Bohn, J Ye, and DS Jin. Controlling the quantum stereodynamics of ultracold bimolecular reactions. *Nature Physics*, 7(6):502–507, 2011.

[86] Piotr S Żuchowski and Jeremy M Hutson. Reactions of ultracold alkali-metal dimers. *Physical Review A*, 81(6):060703, 2010.

[87] S Ospelkaus, K-K Ni, G Quéméner, B Neyenhuis, D Wang, MHG de Miranda, JL Bohn, J Ye, and DS Jin. Controlling the hyperfine state of rovibronic ground-state polar molecules. *Physical Review Letters*, 104(3):030402, 2010.

[88] Philip D Gregory, Jesus Aldegunde, Jeremy M Hutson, and Simon L Cornish. Controlling the rotational and hyperfine state of ultracold ^{87}Rb^{133}Cs molecules. *Physical Review A*, 94(4):041403, 2016.

[89] Sebastian A Will, Jee Woo Park, Zoe Z Yan, Huanqian Loh, and Martin W Zwierlein. Coherent microwave control of ultracold ^{23}Na ^{40}K molecules. *Physical Review Letters*, 116(22):225306, 2016.

[90] Mingyang Guo, Xin Ye, Junyu He, Goulven Quéméner, and Dajun Wang. Internal state control of ultracold ^{23}Na^{87}Rb molecules. In preparation.

[91] Amodsen Chotia, Brian Neyenhuis, Steven A Moses, Bo Yan, Jacob P Covey, Michael Foss-Feig, Ana Maria Rey, Deborah S Jin, and Jun Ye. Long-lived dipolar molecules and Feshbach molecules in a 3D optical lattice. *Physical Review Letters*, 108(8):080405, 2012.

[92] Steven A Moses, Jacob P Covey, Matthew T Miecnikowski, Bo Yan, Bryce Gadway, Jun Ye, and Deborah S Jin. Creation of a low-entropy quantum gas of polar molecules in an optical lattice. *Science*, 350(6261):659–662, 2015.

[93] Lukas Reichsöllner, Andreas Schindewolf, Tetsu Takekoshi, Rudolf Grimm, and Hanns-Christoph Nägerl. Quantum engineering of a low-entropy gas of heteronuclear bosonic molecules in an optical lattice. *Physical Review Letters*, 118(7):073201, 2017.

[94] Michael Mayle, Goulven Quéméner, Brandon P Ruzic, and John L Bohn. Scattering of ultracold molecules in the highly resonant regime. *Physical Review A*, 87(1):012709, 2013.

[95] Mireille Aymar and Olivier Dulieu. Calculation of accurate permanent dipole moments of the lowest $^{1,3}\Sigma^+$ states of heteronuclear alkali dimers us-

ing extended basis sets. *The Journal of Chemical Physics*, 122(20):204302, 2005.

[96] A Pashov, O Docenko, M Tamanis, R Ferber, H Knöckel, and E Tiemann. Potentials for modeling cold collisions between Na (3S) and Rb (5S) atoms. *Physical Review A*, 72(6):062505, 2005.

[97] Jenning Y Seto, Robert J Le Roy, Jean Verges, and Claude Amiot. Direct potential fit analysis of the $X^1\Sigma_g^+$ state of Rb_2: Nothing else will do! *The Journal of Chemical Physics*, 113(8):3067–3076, 2000.

[98] KM Jones, S Maleki, S Bize, PD Lett, CJ Williams, H Richling, H Knöckel, E Tiemann, H Wang, PL Gould, et al. Direct measurement of the ground-state dissociation energy of Na_2. *Physical Review A*, 54(2):R1006, 1996.

[99] S Ospelkaus, A Pe'Er, K-K Ni, JJ Zirbel, B Neyenhuis, S Kotochigova, PS Julienne, J Ye, and DS Jin. Efficient state transfer in an ultracold dense gas of heteronuclear molecules. *Nature Physics*, 4:622, 2008.

[100] Fudong Wang, Xiaoke Li, Dezhi Xiong, and Dajun Wang. A double species ^{23}Na and ^{87}Rb Bose–Einstein condensate with tunable miscibility via an interspecies Feshbach resonance. *Journal of Physics B: Atomic, Molecular and Optical Physics*, 49(1):015302, 2015.

[101] Fudong Wang, Dezhi Xiong, Xiaoke Li, Dajun Wang, and Eberhard Tiemann. Observation of Feshbach resonances between ultracold Na and Rb atoms. *Physical Review A*, 87(5):050702, 2013.

[102] Fudong Wang, Xiaodong He, Xiaoke Li, Bing Zhu, Jun Chen, and Dajun Wang. Formation of ultracold NaRb Feshbach molecules. *New Journal of Physics*, 17(3):035003, 2015.

[103] Fudong Wang. *Studies of an ultracold Bose-Bose mixture with tunable interspecies interactions*. PhD thesis, The Chinese University of Hong Kong, Hong Kong, 2016.

[104] Bing Zhu. *Studies of Polar Molecules and Spinor Gases with an Ultracold Mixture of Na and Rb Atoms*. PhD thesis, The Chinese University of Hong Kong, Hong Kong, 2016.

[105] K Bergmann, H Theuer, and BW Shore. Coherent population transfer among quantum states of atoms and molecules. *Reviews of Modern Physics*, 70(3):1003, 1998.

[106] Nikolay V Vitanov, Andon A Rangelov, Bruce W Shore, and Klaas Bergmann. Stimulated Raman adiabatic passage in physics, chemistry, and beyond. *Reviews of Modern Physics*, 89(1):015006, 2017.

[107] Michael Fleischhauer and Aaron S Manka. Propagation of laser pulses and coherent population transfer in dissipative three-level systems: An adiabatic dressed-state picture. *Physical Review A*, 54(1):794, 1996.

[108] Nikolay V Vitanov, Thomas Halfmann, Bruce W Shore, and Klaas Bergmann. Laser-induced population transfer by adiabatic passage techniques. *Annual Review of Physical Chemistry*, 52(1):763–809, 2001.

[109] LP Yatsenko, VI Romanenko, BW Shore, and K Bergmann. Stimulated Raman adiabatic passage with partially coherent laser fields. *Physical Review A*, 65(4):043409, 2002.

[110] Marlan O Scully and M Suhail Zubairy. *Quantum optics*. AAPT, 1999.

[111] Jonathan D Pritchard. *Cooperative optical non-linearity in a blockaded Rydberg ensemble*. Springer Science & Business Media, 2012.

[112] Goran Lindblad. On the generators of quantum dynamical semigroups. *Communications in Mathematical Physics*, 48(2):119–130, 1976.

[113] Wolfgang Petrich, Michael H Anderson, Jason R Ensher, and Eric A Cornell. Stable, tightly confining magnetic trap for evaporative cooling of neutral atoms. *Physical Review Letters*, 74(17):3352, 1995.

[114] Y-J Lin, Abigail R Perry, Robert L Compton, Ian B Spielman, and James V Porto. Rapid production of ^{87}Rb Bose-Einstein condensates in a combined magnetic and optical potential. *Physical Review A*, 79(6):063631, 2009.

[115] Dezhi Xiong, Fudong Wang, Xiaoke Li, Ting-Fai Lam, and Dajun Wang. Production of a rubidium Bose-Einstein condensate in a hybrid trap with light induced atom desorption. *ArXiv:1303.0333*, 2013.

[116] Paul S Julienne, Eite Tiesinga, and Thorsten Köhler. Making cold molecules by time-dependent Feshbach resonances. *Journal of Modern Optics*, 51(12):1787–1806, 2004.

[117] J Stenger, S Inouye, MR Andrews, H-J Miesner, DM Stamper-Kurn, and W Ketterle. Strongly enhanced inelastic collisions in a Bose-Einstein condensate near Feshbach resonances. *Physical Review Letters*, 82(12):2422, 1999.

[118] Takashi Mukaiyama, JR Abo-Shaeer, Kaiwen Xu, Jit Kee Chin, and W Ketterle. Dissociation and decay of ultracold sodium molecules. *Physical Review Letters*, 92(18):180402, 2004.

[119] Stephan Dürr, Thomas Volz, and Gerhard Rempe. Dissociation of ultracold molecules with Feshbach resonances. *Physical Review A*, 70(3):031601, 2004.

[120] Fudong Wang, Xin Ye, Mingyang Guo, D Blume, and Dajun Wang. Exploring Few-Body Processes with an Ultracold Light-Heavy Bose-Bose Mixture. *ArXiv:1611.03198*, 2016.

[121] RWP Drever, John L Hall, FV Kowalski, J_ Hough, GM Ford, AJ Munley, and H Ward. Laser phase and frequency stabilization using an optical resonator. *Applied Physics B*, 31(2):97–105, 1983.

[122] Bo Lu and Dajun Wang. Note: A four-pass acousto-optic modulator system for laser cooling of sodium atoms. *Review of Scientific Instruments*, 88(7):076105, 2017.

[123] Donley, EA and Heavner, TP and Levi, F and Tataw, MO and Jefferts, SR. Double-pass acousto-optic modulator system. *Review of Scientific Instruments*, 76(6):063112, 2005.

[124] Eric D Black. An introduction to Pound–Drever–Hall laser frequency stabilization. *American Journal of Physics*, 69(1):79–87, 2001.

[125] Timothy Day, Eric K Gustafson, and Robert L Byer. Sub-hertz relative frequency stabilization of two-diode laser-pumped Nd: YAG lasers locked to a Fabry-Perot interferometer. *IEEE Journal of Quantum Electronics*, 28(4):1106–1117, 1992.

[126] Miao Zhu and John L Hall. Stabilization of optical phase/frequency of a laser system: application to a commercial dye laser with an external stabilizer. *JOSA B*, 10(5):802–816, 1993.

[127] M Nickerson. A review of pound-drever-hall laser frequency locking.

[128] Edward A Whittaker, Manfred Gehrtz, and Gary C Bjorklund. Residual amplitude modulation in laser electro-optic phase modulation. *JOSA B*, 2(8):1320–1326, 1985.

[129] Richard W Fox, Chris W Oates, and Leo W Hollberg. 1. Stabilizing diode lasers to high-finesse cavities. *Experimental Methods in the Physical Sciences*, 40:1–46, 2003.

[130] John L Hall, Matthew S Taubman, and Jun Ye. Laser stabilization. *OSA Handbook v14*, 1999.

[131] DS Elliott, Rajarshi Roy, and SJ Smith. Extracavity laser band-shape and bandwidth modification. *Physical Review A*, 26(1):12, 1982.

[132] Mingyang Guo, Romain Vexiau, Bing Zhu, Bo Lu, Nadia Bouloufa-Maafa, Olivier Dulieu, and Dajun Wang. High-resolution molecular spectroscopy for producing ultracold absolute-ground-state ^{23}Na^{87}Rb molecules. *Physical Review A*, 96(5):052505, 2017.

[133] George W Coulston and Klaas Bergmann. Population transfer by stimulated Raman scattering with delayed pulses: analytical results for multilevel systems. *The Journal of Chemical Physics*, 96(5):3467–3475, 1992.

[134] NV Vitanov and Stig Stenholm. Adiabatic population transfer via multiple intermediate states. *Physical Review A*, 60(5):3820, 1999.

[135] Kevin M Jones, Eite Tiesinga, Paul D Lett, and Paul S Julienne. Ultracold photoassociation spectroscopy: Long-range molecules and atomic scattering. *Reviews of Modern Physics*, 78(2):483, 2006.

[136] William C Stwalley, Michael Bellos, Ryan Carollo, Jayita Banerjee, and Matthew Bermudez. Shortcuts for understanding rovibronic spectroscopy of ultracold alkali metal diatomic molecules. *Molecular Physics*, 110(15-16):1739–1755, 2012.

[137] O Docenko, M Tamanis, R Ferber, EA Pazyuk, A Zaitsevskii, AV Stolyarov, A Pashov, H Knöckel, and E Tiemann. Deperturbation treatment of the

$A^1\Sigma^+$–$b^3\Pi$ complex of NaRb and prospects for ultracold molecule formation in $X^1\Sigma^+$ (v= 0; J= 0). *Physical Review A*, 75(4):042503, 2007.

[138] A Pashov, W Jastrzebski, P Kortyka, and P Kowalczyk. Experimental long range potential of the $B^1\Pi$ state in NaRb. *The Journal of Chemical Physics*, 124(20):204308, 2006.

[139] M Aymar and O Dulieu. Calculations of transition and permanent dipole moments of heteronuclear alkali dimers NaK, NaRb and NaCs. *Molecular Physics*, 105(11-12):1733–1742, 2007.

[140] Svetlana Kotochigova, Eite Tiesinga, and Paul S Julienne. Multi-channel modelling of the formation of vibrationally cold polar KRb molecules. *New Journal of Physics*, 11(5):055043, 2009.

[141] Warren T Zemke and William C Stwalley. Long-range potential energy curves for the $X^1\Sigma^+$ and $a^3\Sigma^+$ states of NaRb. *The Journal of Chemical Physics*, 114(24):10811–10815, 2001.

[142] O Docenko, O Nikolayeva, M Tamanis, R Ferber, EA Pazyuk, and AV Stolyarov. Experimental studies of the NaRb ground-state potential up to the v = 76 level. *Physical Review A*, 66(5):052508, 2002.

[143] O Docenko, M Tamanis, R Ferber, A Pashov, H Knöckel, and E Tiemann. Potential of the ground state of NaRb. *Physical Review A*, 69(4):042503, 2004.

[144] M Tamanis, R Ferber, A Zaitsevskii, EA Pazyuk, AV Stolyarov, Hongmin Chen, Jianbing Qi, Henry Wang, and William C Stwalley. High resolution spectroscopy and channel-coupling treatment of the $A^1\Sigma^+$–$b^3\Pi$ complex of NaRb. *The Journal of Chemical Physics*, 117(17):7980–7988, 2002.

[145] Markus Debatin, Tetsu Takekoshi, Raffael Rameshan, Lukas Reichsöllner, Francesca Ferlaino, Rudolf Grimm, Romain Vexiau, Nadia Bouloufa,

Olivier Dulieu, and Hanns-Christoph Nägerl. Molecular spectroscopy for ground-state transfer of ultracold RbCs molecules. *Physical Chemistry Chemical Physics*, 13(42):18926–18935, 2011.

[146] Jee Woo Park, Sebastian A Will, and Martin W Zwierlein. Two-photon pathway to ultracold ground state molecules of $^{23}Na^{40}K$. *New Journal of Physics*, 17(7):075016, 2015.

[147] D Borsalino, R Vexiau, M Aymar, E Luc-Koenig, O Dulieu, and N Bouloufa-Maafa. Prospects for the formation of ultracold polar ground state KCs molecules via an optical process. *Journal of Physics B: Atomic, Molecular and Optical Physics*, 49(5):055301, 2016.

[148] Markus Deiß, Björn Drews, Johannes Hecker Denschlag, and Eberhard Tiemann. Mixing of and observed in the hyperfine and Zeeman structure of ultracold molecules. *New Journal of Physics*, 17(8):083032, 2015.

[149] A Orbán, R Vexiau, O Krieglsteiner, H-C Nägerl, Olivier Dulieu, A Crubellier, and N Bouloufa-Maafa. Model for the hyperfine structure of electronically excited KCs molecules. *Physical Review A*, 92(3):032510, 2015.

[150] Ilona Schmidt-Mink and Wilfried Meyer. Predissociation lifetimes of the $b^3\Pi_u$ state of Li_2 and the accidental predissociation of its $A^1\Sigma_u^+$ state. *Chemical Physics Letters*, 121(1-2):49–56, 1985.

[151] Maxence Lepers, Romain Vexiau, Mireille Aymar, Nadia Bouloufa-Maafa, and Olivier Dulieu. Long-range interactions between polar alkali-metal diatoms in external electric fields. *Physical Review A*, 88(3):032709, 2013.

[152] Jesus Aldegunde and Jeremy M Hutson. Hyperfine structure of alkali-metal diatomic molecules. *Physical Review A*, 96(4):042506, 2017.

[153] Michael Fleischhauer, Atac Imamoglu, and Jonathan P Marangos. Electromagnetically induced transparency: Optics in coherent media. *Reviews of Modern Physics*, 77(2):633, 2005.

[154] Bing Zhu, Xiaoke Li, Xiaodong He, Mingyang Guo, Fudong Wang, Romain Vexiau, Nadia Bouloufa-Maafa, Olivier Dulieu, and Dajun Wang. Long-range states of the narb molecule near the $Na(3^2S_{1/2})+ Rb(5^2P_3/2)$ asymptote. *Physical Review A*, 93(1):012508, 2016.

[155] RJ Le Roy. Level 8.0: A computer program for solving the Radial Schrödinger equation for bound and quasibound levels. *University of Waterloo Chemical Physics Research Report CP-663*, 2007.

[156] Xiaoke Li. *Coherent Heteronuclear Spin Dynamics in an Ultracold Spinor Mixture*. PhD thesis, The Chinese University of Hong Kong, Hong Kong, 2015.

[157] Charles H Townes and Arthur L Schawlow. *Microwave spectroscopy*. Courier Corporation, 2013.

[158] John M Brown and Alan Carrington. *Rotational spectroscopy of diatomic molecules*. Cambridge University Press, 2003.

[159] A Micheli, G Pupillo, HP Büchler, and P Zoller. Cold polar molecules in two-dimensional traps: Tailoring interactions with external fields for novel quantum phases. *Physical Review A*, 76(4):043604, 2007.

[160] Kang-Kuen Ni. *A quantum gas of polar molecules*. PhD thesis, University of Colorado, USA, 2009.

[161] Paul J Dagdigian and Lennard Wharton. Molecular beam electric deflection and resonance spectroscopy of the heteronuclear alkali dimers: $^{39}K^{7}Li$, $Rb^{7}Li$, $^{39}K^{23}Na$, $Rb^{23}Na$, and $^{133}Cs^{23}Na$. *The Journal of Chemical Physics*, 57(4):1487–1496, 1972.

[162] G Igel-Mann, U Wedig, P Fuentealba, and H Stoll. Ground-state properties of alkali dimers XY (X, Y= Li to Cs). *The Journal of Chemical Physics*, 84(9):5007–5012, 1986.

[163] V Tarnovsky, M Bunimovicz, L Vušković, B Stumpf, and B Bederson. Measurements of the dc electric dipole polarizabilities of the alkali dimer molecules, homonuclear and heteronuclear. *The Journal of Chemical Physics*, 98(5):3894–3904, 1993.

[164] J Kleinert, C Haimberger, PJ Zabawa, and NP Bigelow. Trapping of ultracold polar molecules with a thin-wire electrostatic trap. *Physical Review Letters*, 99(14):143002, 2007.

[165] J Kleinert, C Haimberger, PJ Zabawa, and NP Bigelow. Manufacturing a thin wire electrostatic trap for ultracold polar molecules. *Review of Scientific Instruments*, 78(11):113108, 2007.

[166] MW Gempel, T Hartmann, TA Schulze, KK Voges, A Zenesini, and S Ospelkaus. Versatile electric fields for the manipulation of ultracold NaK molecules. *New Journal of Physics*, 18(4):045017, 2016.

[167] R Vexiau, D Borsalino, M Lepers, A Orbán, M Aymar, O Dulieu, and N Bouloufa-Maafa. Dynamic dipole polarizabilities of heteronuclear alkali dimers: optical response, trapping and control of ultracold molecules. *International Reviews in Physical Chemistry*, 36(4):709–750, 2017.

[168] S Kuhr, W Alt, D Schrader, I Dotsenko, Y Miroshnychenko, W Rosenfeld, M Khudaverdyan, V Gomer, A Rauschenbeutel, and D Meschede. Coherence properties and quantum state transportation in an optical conveyor belt. *Physical Review Letters*, 91(21):213002, 2003.

[169] S Kuhr, W Alt, D Schrader, I Dotsenko, Y Miroshnychenko, A Rauschenbeutel, and D Meschede. Analysis of dephasing mechanisms in a standing-wave dipole trap. *Physical Review A*, 72(2):023406, 2005.

[170] B Neyenhuis, B Yan, SA Moses, JP Covey, A Chotia, A Petrov, S Kotochigova, J Ye, and DS Jin. Anisotropic Polarizability of Ultracold Polar $^{40}K^{87}Rb$ Molecules. *Physical Review Letters*, 109(23):230403, 2012.

[171] Keith D Bonin and Vitaly V Kresin. *Electric-dipole polarizabilities of atoms, molecules, and clusters*. World Scientific, 1997.

[172] Svetlana Kotochigova and David DeMille. Electric-field-dependent dynamic polarizability and state-insensitive conditions for optical trapping of diatomic polar molecules. *Physical Review A*, 82(6):063421, 2010.

[173] Philip D Gregory, Jacob A Blackmore, Jesus Aldegunde, Jeremy M Hutson, and Simon L Cornish. AC Stark Effect in Ultracold Polar RbCs Molecules. *Physical Review A*, 96(2):021402, 2017.

[174] N Balakrishnan. Perspective: Ultracold molecules and the dawn of cold controlled chemistry. *The Journal of Chemical Physics*, 145(15):150901, 2016.

[175] Xin Ye, Mingyang Guo, Maykel L. González-Martínez, Goulven Quéméner, and Dajun Wang. Collisions of ultracold $^{23}Na^{87}Rb$ molecules with controlled chemical reactivities. Submitted to Science Advances.

[176] J Aldegunde, Ben A Rivington, Piotr S Żuchowski, and Jeremy M Hutson. Hyperfine energy levels of alkali-metal dimers: Ground-state polar molecules in electric and magnetic fields. *Physical Review A*, 78(3):033434, 2008.

[177] Ennio Arimondo, M Inguscio, and P Violino. Experimental determinations of the hyperfine structure in the alkali atoms. *Reviews of Modern Physics*, 49(1):31, 1977.

[178] HP Büchler, A Micheli, and P Zoller. Three-body interactions with cold polar molecules. *Nature Physics*, 3:726–731, 2007.

[179] Hans Peter Büchler, Eugene Demler, Mikhail Lukin, Andrea Micheli, N Prokofev, Guido Pupillo, and Peter Zoller. Strongly correlated 2D quantum phases with cold polar molecules: controlling the shape of the interaction potential. *Physical Review Letters*, 98(6):060404, 2007.

[180] AV Gorshkov, P Rabl, G Pupillo, A Micheli, P Zoller, MD Lukin, and HP Büchler. Suppression of inelastic collisions between polar molecules with a repulsive shield. *Physical Review Letters*, 101(7):073201, 2008.

[181] Tino Weber, Jens Herbig, Michael Mark, Hanns-Christoph Nägerl, and Rudolf Grimm. Three-body recombination at large scattering lengths in an ultracold atomic gas. *Physical Review Letters*, 91(12):123201, 2003.

[182] José P DIncao, Hiroya Suno, and Brett D Esry. Limits on universality in ultracold three-boson recombination. *Physical Review Letters*, 93(12):123201, 2004.

[183] C Amiot. Laser-induced fluorescence of Rb2: The (1) 1Σ+ g (X),(2) 1Σ+ g,(1) 1Π u (B),(1) 1Π g, and (2) 1Π u (C) electronic states. *The Journal of Chemical Physics*, 93(12):8591–8604, 1990.

[184] Truman J Odiorne, Philip R Brooks, and Jerome VV Kasper. Molecular beam reaction of K with HCl: Effect of vibrational excitation of HCl. *The Journal of Chemical Physics*, 55(4):1980–1982, 1971.

[185] John C Polanyi. Concepts in reaction dynamics. *Accounts of Chemical Research*, 5(5):161–168, 1972.

[186] J Gary Pruett and Richard N Zare. State-to-state reaction rates: Ba+ HF (v= 0,1) BaF (v= 0-12)+ H. *The Journal of Chemical Physics*, 64(4):1774–1783, 1976.

[187] Richard N Zare. Laser control of chemical reactions. *Science*, 279(5358):1875–1879, 1998.

[188] C Chin, T Kraemer, M Mark, J Herbig, P Waldburger, H-C Nägerl, and R Grimm. Observation of Feshbach-like resonances in collisions between ultracold molecules. *Physical Review Letters*, 94(12):123201, 2005.

[189] Tout T Wang, Myoung-Sun Heo, Timur M Rvachov, Dylan A Cotta, and Wolfgang Ketterle. Deviation from Universality in Collisions of Ultracold Li 2 6 Molecules. *Physical Review Letters*, 110(17):173203, 2013.

[190] Björn Drews, Markus Deiß, Krzysztof Jachymski, Zbigniew Idziaszek, and Johannes Hecker Denschlag. Inelastic collisions of ultracold triplet Rb_2 molecules in the rovibrational ground state. *Nature Communications*, 8:14854, 2017.

[191] Bo Gao. General form of the quantum-defect theory for- $1/r^{\alpha}$ type of potentials with $\alpha > 2$. *Physical Review A*, 78(1):012702, 2008.

[192] Hans Albrecht Bethe. Theory of disintegration of nuclei by neutrons. *Physical Review*, 47(10):747, 1935.

[193] Eugene P Wigner. On the behavior of cross sections near thresholds. *Physical Review*, 73(9):1002, 1948.

[194] Zbigniew Idziaszek and Paul S Julienne. Universal rate constants for reactive collisions of ultracold molecules. *Physical Review Letters*, 104(11):113202, 2010.

[195] Paul S Julienne, Thomas M Hanna, and Zbigniew Idziaszek. Universal ultracold collision rates for polar molecules of two alkali-metal atoms. *Physical Chemistry Chemical Physics*, 13(42):19114–19124, 2011.

[196] A Derevianko, JF Babb, and A Dalgarno. High-precision calculations of van der Waals coefficients for heteronuclear alkali-metal dimers. *Physical Review A*, 63(5):052704, 2001.

[197] PS Żuchowski, M Kosicki, M Kodrycka, and P Soldán. van der Waals coefficients for systems with ultracold polar alkali-metal molecules. *Physical Review A*, 87(2):022706, 2013.

[198] R Vexiau, M Lepers, M Aymar, N Bouloufa-Maafa, and O Dulieu. Long-range interactions between polar bialkali ground-state molecules in arbitrary vibrational levels. *The Journal of Chemical Physics*, 142(21):214303, 2015.

[199] Bo Gao. Universal model for exoergic bimolecular reactions and inelastic processes. *Physical Review Letters*, 105(26):263203, 2010.

[200] Krzysztof Jachymski, Michał Krych, Paul S Julienne, and Zbigniew Idziaszek. Quantum Theory of Reactive Collisions for 1/r n Potentials. *Physical Review Letters*, 110(21):213202, 2013.

[201] Krzysztof Jachymski, Michał Krych, Paul S Julienne, and Zbigniew Idziaszek. Quantum-defect model of a reactive collision at finite temperature. *Physical Review A*, 90(4):042705, 2014.

[202] Michael Mayle, Brandon P Ruzic, and John L Bohn. Statistical aspects of ultracold resonant scattering. *Physical Review A*, 85(6):062712, 2012.

[203] RA Marcus. Lifetimes of active molecules. I. *The Journal of Chemical Physics*, 20(3):352–354, 1952.

[204] RA Marcus. Lifetimes of active molecules. II. *The Journal of Chemical Physics*, 20(3):355–359, 1952.

[205] Raphael D Levine. *Molecular reaction dynamics*. Cambridge University Press, 2005.

[206] G Reinaudi, T Lahaye, Z Wang, and D Guéry-Odelin. Strong saturation absorption imaging of dense clouds of ultracold atoms. *Optics Letters*, 32(21):3143–3145, 2007.

[207] Woo Jin Kwon, Jae-yoon Choi, and Yong-il Shin. Calibration of saturation absorption imaging of ultracold atom clouds. *Journal of the Korean Physical Society*, 61(12):1970–1974, 2012.

[208] J Söding, D Guéry-Odelin, P Desbiolles, G Ferrari, and J Dalibard. Giant spin relaxation of an ultracold cesium gas. *Physical Review Letters*, 80(9):1869, 1998.

[209] Gaoren Wang and Goulven Quéméner. Tuning ultracold collisions of excited rotational dipolar molecules. *New Journal of Physics*, 17(3):035015, 2015.

[210] Goulven Quéméner. Ultracold collisions of molecules. *ArXiv:1703.09174*, 2017.

[211] Goulven Quéméner, private communication.

[212] Mingyang Guo, Xin Ye, Junyu He, Goulven Quéméner, and Dajun Wang. Dipolar collisions of ultracold ground-state bosonic molecules. In preparation.

[213] JL Bohn, M Cavagnero, and C Ticknor. Quasi-universal dipolar scattering in cold and ultracold gases. *New Journal of Physics*, 11(5):055039, 2009.

[214] Goulven Quéméner, John L Bohn, Alexander Petrov, and Svetlana Kotochigova. Universalities in ultracold reactions of alkali-metal polar molecules. *Physical Review A*, 84(6):062703, 2011.

[215] Vladimir Roudnev and Michael Cavagnero. Universal resonant ultracold molecular scattering. *Physical Review A*, 79(1):014701, 2009.

[216] Goulven Quéméner and John L Bohn. Strong dependence of ultracold chemical rates on electric dipole moments. *Physical Review A*, 81(2):022702, 2010.

[217] Zbigniew Idziaszek, Goulven Quéméner, John L Bohn, and Paul S Julienne. Simple quantum model of ultracold polar molecule collisions. *Physical Review A*, 82(2):020703, 2010.

[218] JFE Croft, C Makrides, M Li, A Petrov, BK Kendrick, N Balakrishnan, and S Kotochigova. Universality and chaoticity in ultracold K+ KRb chemical reactions. *Nature Communications*, 8, 2017.

[219] JFE Croft, N Balakrishnan, and BK Kendrick. Long-lived complexes and signatures of chaos in ultracold K_2+Rb collisions. *arXiv:1709.07419*, 2017.

[220] Alexander V Avdeenkov, Masatoshi Kajita, and John L Bohn. Suppression of inelastic collisions of polar $^1\Sigma$ state molecules in an electrostatic field. *Physical Review A*, 73(2):022707, 2006.

[221] Goulven Quéméner and John L Bohn. Shielding $^2\Sigma$ ultracold dipolar molecular collisions with electric fields. *Physical Review A*, 93(1):012704, 2016.

[222] Maykel L González-Martínez, John L Bohn, and Goulven Quéméner. Adimensional theory of shielding in ultracold collisions of dipolar rotors. *Physical Review A*, 96(3):032718, 2017.

[223] Goulven Quéméner and John L Bohn. Electric field suppression of ultracold confined chemical reactions. *Physical Review A*, 81(6):060701, 2010.

[224] Goulven Quéméner and John L Bohn. Dynamics of ultracold molecules in confined geometry and electric field. *Physical Review A*, 83(1):012705, 2011.

[225] Bihui Zhu, Goulven Quéméner, Ana M Rey, and Murray J Holland. Evaporative cooling of reactive polar molecules confined in a two-dimensional geometry. *Physical Review A*, 88(6):063405, 2013.

[226] NIST JILA. Quantum Magnetism with Ultracold Molecules. *From Atomic to Mesoscale: The Role of Quantum Coherence in Systems of Various Complexities*, page 1, 2015.

[227] SV Syzranov, ML Wall, V Gurarie, and AM Rey. Spin-orbital dynamics in a system of polar molecules. *Nature Communications*, 5:5391–5391, 2013.

[228] Norman Y Yao, Alexey V Gorshkov, Chris R Laumann, Andreas M Läuchli, Jun Ye, and Mikhail D Lukin. Realizing fractional Chern insulators in dipolar spin systems. *Physical Review Letters*, 110(18):185302, 2013.